Development of Immunosensors and Immunoassays Using Metallic Nanostructures

by

Ariadne Tuckmantel Bido

B.Sc., University of Campinas, 2013

A Dissertation Submitted in Partial Fulfillment

of the Requirements for the Degree of

DOCTOR OF PHILOSOPHY

in the Department of Chemistry

© Ariadne Tuckmantel Bido, 2023

University of Victoria

All rights reserved. This dissertation may not be reproduced in whole or in part, by photocopy or other means, without the permission of the author.

We acknowledge and respect the lək̓ʷəŋən peoples on whose traditional territory the university stands and the Songhees, Esquimalt and W̱SÁNEĆ peoples whose historical relationships with the land continue to this day.

Supervisory Committee

Development of Immunosensors and Immunoassays Using Metallic Nanostructures

by

Ariadne Tuckmantel Bido

B.Sc., University of Campinas, 2013

Supervisory Committee

Dr. Alexandre Guimarães Brolo (Department of Chemistry)

Supervisor

Dr. Fraser Hof (Department of Chemistry)

Departmental Member

Dr. Caroline Cameron (Department of Biochemistry and Microbiology)

Outside Member

Abstract

Supervisory Committee

Dr. Alexandre Guimarães Brolo (Department of Chemistry)

Supervisor

Dr. Fraser Hof (Department of Chemistry)

Departmental Member

Dr. Caroline Cameron (Department of Biochemistry and Microbiology)

Outside Member

Nanoplasmonic biosensors exploit the unique properties that arise from the interaction of light with free electrons of metallic nanostructures. They offer several advantages over the currently most employed methods of detection. These biosensors can be used for screening of infectious diseases, early diagnosis, management of chronic conditions, food quality and safety, among others. In this dissertation, the focus is on the development of surface-enhanced spectroscopy (SERS) and localized surface plasmon resonance (LSPR)- based immunosensors. A SERS-based immunoassay was developed for detection of IgG from human serum. A method for the sensor construction using poly(dimethylsiloxane) (PDMS) masks in 3D-printed platform, and extrinsic Raman labels (ERLs) were developed. SERS-based immunoassays are well-established in the research community. However, SERS-based sensors are questioned regarding their reproducibility and robustness. This is due to the large fluctuations in intensities in SERS measurements caused by inhomogeneous hotspots distributions in the sensing areas. The substantial local optical field variation within nanometers can affect reliability and reproducibility of these sensors. This effect particularly affects assays at low to ultralow concentrations (pM and lower) since there are less probed species per area in those conditions. Additionally, the common assumption that the analytical SERS intensities at all concentrations follow a Gaussian distribution can be detrimental to the reliable implementation of SERS-based assays. In this work, extensive SERS measurements were taken from the constructed sensors and the SERS intensities were shown to be log-normal distributed, particularly at low concentrations. Assessment of the number of measurements (sample size) per sensor at a particular concentration taken at different positions on the sensor surface were discussed. This study is a step forward towards the determination of best practices for a more reliable and robust employment of quantitative SERS-based immunoassays. A digital SERS protocol was also developed for the determination of SARS-CoV-2 (2019-nCoV) spike S1 + S2 ECD-His recombinant protein in saliva. In general, SERS-based immunoassays rely on a linear relationship between the average Raman intensity of a molecular reporter embedded in a SERS probe with the concentration of the analyte. As the concentration of the analyte decreases, the probability of a statistically significant number of SERS probes to be illuminated by the laser excitation also decreases. Additionally, there is large variation of intensities inherent to SERS and the inhomogeneous distribution of hotspots in the sensor being probed. These factors contribute to a loss in linearity of the assay at low concentrations of analyte and/or extrinsic Raman labels (ERLs). Here, an immunoassay was developed for determination of concentration of SARS-CoV-2 in saliva, and the conventional data treatment was compared to a digital protocol. The digital protocol generated a calibration curve with good linearity whereas the conventional approach did not. This approach is simple and can be employed in heterogeneous SERS immunoassays to improve both the limit-of-detection (LOD) and the dynamic working range. Finally, a low-cost localized surface plasmon resonance (LSPR)-based sensor was developed for SARS-CoV-2 screening in saliva. The sensor was built on plastic well plates for high throughput, but they can also be constructed in individual (discardable) plastic strips. The results were accessed using a plate reader, a ubiquitous equipment in laboratories and research centers. The sensor was challenged with 16 patient samples, being half COVID positive and half COVID negative. The sensor was developed in two modalities: 1) viral detection in saliva; and 2) antibody against COVID in saliva. Both sensors successfully classified all COVID positive patients (among hospitalized and non-hospitalized), and 7/8 COVID negative patients. This sensor is of low cost and of easy construction and is an alternative for SARS-CoV-2 screening in underserved communities. This sensor can be adapted to be used with other screening tests, by changing the element of recognition for other viral particles or antigens.

Table of Contents

List of Tables

List of Figures

Acknowledgements

"It takes a village." I've heard this phrase from our dear biomedical core manager regarding research and the production of scientific knowledge. Looking behind on those years that I had the pleasure to work and learn at Uvic, I can say this is the absolute truth. It would be impossible to track and thank all the people involved in every aspect of this journey, so I'll have to list the main contributors:

My supervisor, Dr. Alexandre Guimarães Brolo, for giving me the opportunity to be part of his group, encouraging independent thought and believing in me, sometimes more than I did.

Rebecca Hof, CAMTEC lab manager- biomedical core, for helping me think outside the box; I am thankful for our chats and your freely given help.

Everybody involved in the Centre for Advanced Materials and Related Technology -CAMTEC for the network of experts that support equipment training, use and problem-solving.

The past and current Brolo group members and extended family for the great work environment.

Thank you, Dr. Elaine Humphrey, Dr. Jonathan Rudge, Dr. Alex Wlasenko, Dr. Stanislav Koronov, Dr. Milton Wang, Sean Adams and Dr. Brent Gowen, for the support in equipment use and helpful discussions.

The science stores personnel: Rob Iuvale, Kara White, Christine MacInnis Rowan and Ian Sandercock. A special thanks to Stephanie Puckett; she is a ray of sunshine that always made the day better.

Thanks to MSc. Nahiane Pipaon Fernandez, a dear friend, for proofreading my texts and for the emotional support. My goal is to be as strong and competent as you are one day.

Thanks to UVic and NSERC for funding.

Dedication

This dissertation is dedicated to my beloved husband João Fabrício Wohnrath. He was and is the cornerstone that supports me through life challenges. He is the dandelion in the spring, the knowledge that we'll always be there for each other. Thank you for always being there for me.

Chapter 1: Overview

1.1 Context

Biosensors are ubiquitous in biomedical diagnosis, screening tests, chronic diseases management, environmental monitoring, food safety, forensics, biomedical research and drug development.[1] According to WHO (World Health Organization), cancer is the second leading cause for deaths, causing more than 10 million deaths per year.[2] Detection of cancers in advanced stages leads to a significant number of deaths. The vast heterogeneity of this disease requires ultrasensitive biosensors for early diagnosis and personalized treatment.[3] Diabetes is chronic disease that is present in 8.5% of the population above 18 years of age and that also requires biosensors for constant glucose monitoring.[4] Recently, policy makers relied on screening tests results to make informed decisions to control the highly contagious severe acute respiratory syndrome coronavirus 2 (SARS-CoV-2) global pandemic. The disproportion of tests distribution, specifically to low-income countries affected how the disease was dealt with and contributed to the higher death toll in those communities.

The first biosensor was developed in 1956 by Leland C. Clark. His invention of a functional oxygen detector for blood, water and other liquids earned him the moniker “father of biosensors”.[5] The modern-day glucose sensor, used by millions of diabetics for daily glucose monitoring, is based on his research. Glucose monitors have evolved to wearable, minimally invasive subcutaneous devices called continuous glucose monitoring (CGM) sensors, providing real time measurements every 1-5 minutes.[6] It relies on indirect detection of glucose oxidase, fluorescence intensity or skin dielectric properties.[6,7] Other point-of-care (POC) biosensors are screen printed and lateral flow assay (LFA) biosensors. There are several types of biosensors, such as enzyme, tissue or DNA-based, thermal and piezoelectric.[8] There is a trend of miniaturization of biosensing systems for point-of-care (POC) testing with integration to existing handheld devices or microfluidic systems. Sensor specificity is determined by the target recognition and sensitivity is significantly influenced by the transducer and amplifier, which translate molecular recognition into measurable signal. Specificity is the ability of the biosensor to differentiate the analyte from non-targets in the sample.[9] The sensitivity is the relationship between the change in analyte concentration with the signal generated by the transducer.[10] Ideally, small changes in analyte concentration should generate large responses in the transducer. Figure 1-1 shows the molecular recognition of the target and types of handheld instruments and microfluidic platforms used for miniaturization.[11]

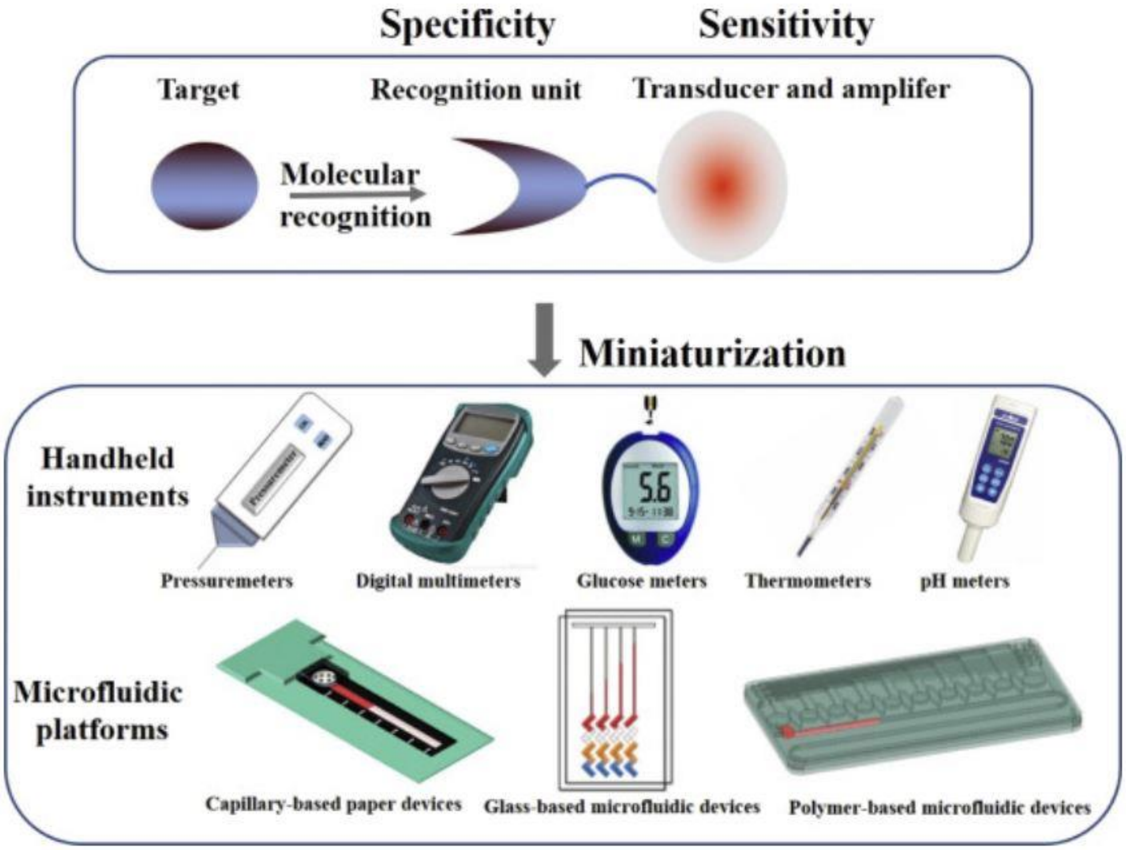

Figure 1-1. Biosensor principle in a POC setting. Target recognition determines the specificity and the transducer and amplifier determine the sensitivity of the biosensor. Some examples of the miniaturization in handheld instruments and microfluidic platforms.[11] [Used with permission from Reference 11]

Nanotechnology has been employed in the development of biosensors. Nanostructured materials have at least one dimension in the nanoscale range (< 100 nm), and can be made of one material (e.g metals, different types of carbon, polymers) or composites (e.g. polymer-metal, silica-metal, graphene-metal).[12] Engineered nanomaterials can have superior electrical conductivity, mechanical performance, capacity of surface functionalization, large surface area, tunable porosity and enhanced diffusivity.[13] Additionally, they can be compatible with biological molecules, making them ideal candidates for biosensor transducers.[14]

New medical diagnosis strategies in the last decade focus on plasmonic materials.[15,16] Plasmonic materials are metallic nanostructures with unique optical and electronic properties due to the collective oscillation of free electrons known as localized surface plasmons resonance (LSPR).[17] Plasmonic-based sensors are being studied with the promise of higher sensitivity and selectivity, easy of operation, minimal sample treatment, broad linear range relative to the current state-of-the-art.[18] There are different sensing platforms that rely on plasmonic behaviour, such as surface plasmon resonance (SPR), localized surface plasmon resonance (LSPR), surface-enhanced fluorescence (SEF), surface-enhanced Raman scattering (SERS), surface-enhanced infrared absorption spectroscopy (SEIRA).[18] Each platform has distinct features that make them suitable for different applications. For instance, in SEF-based biosensors, there is an increase in the fluorescence intensity of a fluorophore material by having it in a proximity of a metallic nanostructure. The associated local plasmonic electric field couples with the fluorophore electrons. This causes an enhanced fluorescence emission.[18] SERS-based biosensors have the Raman signal enhanced by attaching a reporter (e.g. dye) directly to a metal nanoparticle. The difference between these phenomena is the distance of the molecule and the nanostructure. For SERS, the fluorescence emission is quenched whereas for SEF a molecular spacer sits between the nanostructure and the fluorophore.[19] SEF has been used to detect DNA strands, oligonucleotides, RNA, toxins (Ochratoxin A, microcystin-LR, anthrax toxin), virus (e.g influenza A) and bacteria (e.g *E. coli*).[20] SERS-based biosensors have been used to detect bacteria, toxins, oligonucleotides, viral particles, DNA, cell surface antigens and others.[21]

1.2 Objectives

In this work, the focus will be on SERS-based and LSPR-based immunosensors. SERS-based immunoassays have advantages over traditional methods based on fluorescence and chemiluminescence (e.g ELISA). These advantages are higher sensitivity, multiplexing, and ability to perform detection in blood and other biological matrices.[22] However, SERS-based sensors are considered a "poorly reproducible and insufficiently robust analytical technique".[23] This is due to a high signal variation caused by the inhomogeneous distribution of hotspots on the sensor. Non-standardized sample preparation, different approaches to data analysis, different types of substrates, variations in instrument settings, among other factors also contribute to the large variations in the sensor response.[24] Chapters 3 and 4 are describe approaches to improve the characteristics of SERS-based immunosensors. Considerable effort was devoted to improve analytical procedures in SERS.[25] Those include studies on the variability of SERS substrates [26–28] and on the reproducibility between SERS methods applied in different laboratories[23]. Chapter 3 has the objective of developing a reliable SERS-based immunosensors with a robust statistic to verify the population distribution of the SERS measurements for different tested concentrations of the analytes. The observation of these distributions provided a better understanding for the best practices for data analysis in SERS, since they reveal the relationship between number of measurements and % error compared to a quality control sample.

Next, the focus is on exploring a better method to apply a new type of data analysis to assays in the low concentration range (pM). The conventional data analysis relies on creating calibration curve using relationship between the average of the SERS intensity of a Raman reporter to the antigen concentration.[29,30] This approach works well in systems with high concentration of analyte. However, as the concentration of analyte decreases, the probability of a statistically significant number of SERS probes (extrinsic Raman labels – ERLs) under the excitation laser decreases and it becomes challenging to correlate SERS intensities to concentration of analyte reliably.[31] In Chapter 4, a SERS-immunoassay was developed for determination of concentration of SARS-CoV-2 in saliva at very low concentrations (pM range). A new digital protocol method was applied to the dataset to tackle the lack of linearity between SERS intensities and analyte concentrations described above. The approach consisted of attributing 1 and 0 to SERS intensities above and below (respectively) a defined threshold. This method was compared to the conventional data treatment used in SERS-based immunoassays and it showed a better linearity for the tested concentrations (pM range).

The necessity for cheap and widely available screening tests were evident with the health crisis that started in 2019 as the SARS-CoV-2 virus spread around the world. The availability of screening tests for COVID-19 is still a challenge, especially for low-income countries and communities. Chapter 5 is dedicated to a development of a low-cost LSPR-based sensor for SARS-CoV-2 screening in saliva. The sensor was developed in two modalities, for viral screening and immunological response (antibody against the virus).

1.3 Dissertation Outline

This dissertation is organized in article-style format.

Chapter 2 presents a context and introduction to the topics of biosensors and immunoassays, the different types of immunoassays, an introduction to plasmonic biosensors and the use of SERS and LSPR to construct immunosensors.

Chapter 3 is based on the published work: Ariadne Tuckmantel Bido, Arash Azarakhshi, and Alexandre G. Brolo, "Exploring Intensity Distributions and Sampling in SERS-Based Immunoassays." Analytical Chemistry 2022 94 (49), 17031-17038.

Chapter 4 is based on the work: "A Digital SERS Protocol for the Determination of SARS-CoV-2 in Saliva Samples", which is under review at the time of the submission of this document, manuscript ID: se-2023-001727.

Chapter 5 is based on the work: "Detection of SARS-CoV-2 in Saliva by a Low-cost LSPR-based Sensor", that is ready for submission.

1.4 References

(1) Bhalla, N.; Jolly, P.; Formisano, N.; Estrela, P. Introduction to Biosensors. *Essays Biochem* **2016**, *60* (1), 1–8.

(2) *Cancer*. https://www.who.int/news-room/fact-sheets/detail/cancer (accessed 2023-01-21).

(3) Blanco-Formoso, M.; Alvarez-Puebla, R. A. Cancer Diagnosis through SERS and Other Related Techniques. *Int J Mol Sci* **2020**, *21* (6), 2253.

(4) *Diabetes*. https://www.who.int/news-room/fact-sheets/detail/diabetes (accessed 2023-01-21).

(5) *Biosensing for the 21st Century*; Renneberg, R., Lisdat, F., Eds.; Advances in Biochemical Engineering/Biotechnology; Springer Berlin Heidelberg: Berlin, Heidelberg, 2008; Vol. 109.

(6) Cappon, G.; Acciaroli, G.; Vettoretti, M.; Facchinetti, A.; Sparacino, G. Wearable Continuous Glucose Monitoring Sensors: A Revolution in Diabetes Treatment. *Electronics* **2017**, *6* (3), 65.

(7) Chen, C.; Zhao, X.-L.; Li, Z.-H.; Zhu, Z.-G.; Qian, S.-H.; Flewitt, A. J. Current and Emerging Technology for Continuous Glucose Monitoring. *Sensors (Basel)* **2017**, *17* (1), 182.

(8) Mehrotra, P. Biosensors and Their Applications – A Review. *Journal of Oral Biology and Craniofacial Research* **2016**, *6* (2), 153–159.

(9) Varshney, M.; Mallikarjunan, K. Challenges in Biosensor Development: Detection Limit, Detection Time, and Specificity. *Resource: Engineering and Technology for Sustainable World* **2009**, *16* (7), 18–21.

(10) Tetyana, P.; Shumbula, P. M.; Njengele-Tetyana, Z.; Tetyana, P.; Shumbula, P. M.; Njengele-Tetyana, Z. *Biosensors: Design, Development and Applications*; IntechOpen, 2021.

(11) Liu, D.; Wang, J.; Wu, L.; Huang, Y.; Zhang, Y.; Zhu, M.; Wang, Y.; Zhu, Z.; Yang, C. Trends in Miniaturized Biosensors for Point-of-Care Testing. *TrAC Trends in Analytical Chemistry* **2020**, *122*, 115701.

(12) *Applications of Nanostructured Materials*. https://encyclopedia.pub/entry/21548 (accessed 2023-02-14).

(13) Malhotra, B. D.; Ali, Md. A. Nanomaterials in Biosensors. *Nanomaterials for Biosensors* **2018**, 1–74.

(14) Kyriakides, T. R.; Raj, A.; Tseng, T. H.; Xiao, H.; Nguyen, R.; Mohammed, F. S.; Halder, S.; Xu, M.; Wu, M. J.; Bao, S.; Sheu, W. C. Biocompatibility of Nanomaterials and Their Immunological Properties. *Biomed Mater* **2021**, *16* (4), 10.1088/1748-605X/abe5fa.

(15) Wang, Z.; Chen, J.; Khan, S. A.; Li, F.; Shen, J.; Duan, Q.; Liu, X.; Zhu, J. Plasmonic Metasurfaces for Medical Diagnosis Applications: A Review. *Sensors* **2022**, *22* (1), 133.

(16) Brolo, A. G. Plasmonics for Future Biosensors. *Nature Photon* **2012**, *6* (11), 709–713.

(17) Mauriz, E.; Lechuga, L. M. Plasmonic Biosensors for Single-Molecule Biomedical Analysis. *Biosensors* **2021**, *11* (4), 123.

(18) Shrivastav, A. M.; Cvelbar, U.; Abdulhalim, I. A Comprehensive Review on Plasmonic-Based Biosensors Used in Viral Diagnostics. *Commun Biol* **2021**, *4* (1), 1–12.

(19) Ru, E. C. L.; Etchegoin, P. G. Surface-Enhanced Raman Scattering (SERS) and Surface-Enhanced Fluorescence (SEF) in the Context of Modified Spontaneous Emission. arXiv September 18, 2005. http://arxiv.org/abs/physics/0509154 (accessed 2023-02-14).

(20) Sultangaziyev, A.; Bukasov, R. Review: Applications of Surface-Enhanced Fluorescence (SEF) Spectroscopy in Bio-Detection and Biosensing. *Sensing and Bio-Sensing Research* **2020**, *30*, 100382.

(21) Ambartsumyan, O.; Gribanyov, D.; Kukushkin, V.; Kopylov, A.; Zavyalova, E. SERS-Based Biosensors for Virus Determination with Oligonucleotides as Recognition Elements. *Int J Mol Sci* **2020**, *21* (9), 3373.

(22) Krafft, C.; Popp, J. Raman-Based Technologies for Biomedical Diagnostics. In *Comprehensive Biomedical Physics*; Elsevier, 2014; pp 189–208.

(23) Fornasaro, S.; Alsamad, F.; Baia, M.; Batista de Carvalho, L. A. E.; Beleites, C.; Byrne, H. J.; Chiadò, A.; Chis, M.; Chisanga, M.; Daniel, A.; Dybas, J.; Eppe, G.; Falgayrac, G.; Faulds, K.; Gebavi, H.; Giorgis, F.; Goodacre, R.; Graham, D.; La Manna, P.; Laing, S.; Litti, L.; Lyng, F. M.; Malek, K.; Malherbe, C.; Marques, M. P. M.; Meneghetti, M.; Mitri, E.; Mohaček-Grošev, V.; Morasso, C.; Muhamadali, H.; Musto, P.; Novara, C.; Pannico, M.; Penel, G.; Piot, O.; Rindzevicius, T.; Rusu, E. A.; Schmidt, M. S.; Sergo, V.; Sockalingum, G. D.; Untereiner, V.; Vanna, R.; Wiercigroch, E.; Bonifacio, A. Surface Enhanced Raman Spectroscopy for Quantitative Analysis: Results of a Large-Scale European Multi-Instrument Interlaboratory Study. *Anal. Chem.* **2020**, *92* (5), 4053–4064.

(24) Bell, S. E. J.; Charron, G.; Cortés, E.; Kneipp, J.; Chapelle, M. L. de la; Langer, J.; Procházka, M.; Tran, V.; Schlücker, S. Towards Reliable and Quantitative Surface-Enhanced Raman Scattering (SERS): From Key Parameters to Good Analytical Practice. *Angewandte Chemie International Edition* **2020**, *59* (14), 5454–5462.

(25) Muehlethaler, C.; Leona, M.; Lombardi, J. R. Towards a Validation of Surface-Enhanced Raman Scattering (SERS) for Use in Forensic Science: Repeatability and Reproducibility Experiments. *Forensic Science International* **2016**, *268*, 1–13.

(26) Novara, C.; Marta, S. D.; Virga, A.; Lamberti, A.; Angelini, A.; Chiado, A.; Rivolo, P.; Geobaldo, F.; Sergo, V.; Bonifacio, A.; Giorgis, F. SERS-Active Ag Nanoparticles on Porous Silicon and PDMS Substrates: A Comparative Study of Uniformity and Raman Efficiency.

(27) Fisk, H.; Westley, C.; Turner, N. J.; Goodacre, R. Achieving Optimal SERS through Enhanced Experimental Design. *J Raman Spectrosc* **2016**, *47* (1), 59–66.

(28) Guicheteau, J. A.; Farrell, M. E.; Christesen, S. D.; Fountain, A. W.; Pellegrino, P. M.; Emmons, E. D.; Tripathi, A.; Wilcox, P.; Emge, D. Surface-Enhanced Raman Scattering (SERS) Evaluation Protocol for Nanometallic Surfaces. *Appl Spectrosc* **2013**, *67* (4), 396–403.

(29) Luo, S.-C.; Sivashanmugan, K.; Liao, J.-D.; Yao, C.-K.; Peng, H.-C. Nanofabricated SERS-Active Substrates for Single-Molecule to Virus Detection in Vitro: A Review. *Biosensors and Bioelectronics* **2014**, *61*, 232–240.

(30) Wang, Y.; Yan, B.; Chen, L. SERS Tags: Novel Optical Nanoprobes for Bioanalysis. *Chem. Rev.* **2013**, *113* (3), 1391–1428.

(31) de Albuquerque, C. D. L.; Sobral-Filho, R. G.; Poppi, R. J.; Brolo, A. G. Digital Protocol for Chemical Analysis at Ultralow Concentrations by Surface-Enhanced Raman Scattering. *Anal. Chem.* **2018**, *90* (2), 1248–1254.

Chapter 2: Introduction

2.1 Biosensors and Immunoassays

A chemical sensor contains two components: a molecular recognition system (receptor) and a physico-chemical transducer. In a biosensor, the receptor is a biological element such as enzymes, antibody/antigen, oligonucleotides (nucleic acids) or whole cells.[1,2] Additionally, organelles (chloroplasts, mitochondria), microorganisms, tissues (animal and vegetable) and mimetic molecules can be immobilized onto the transducer.[3,4] The transducer is the device that will convert the chemical information into a signal that can be detected (electrical or optical, for instance). Figure 2-1 shows the components necessary for signal generation in a biosensor. There are four main parts in a biosensor: a bioreceptor, a transducer, a signal processor, and an interface display. The analytes can be measured in a variety of samples such as body fluids (e.g. blood, serum, urine, tears, saliva), food samples and cell cultures.[5]

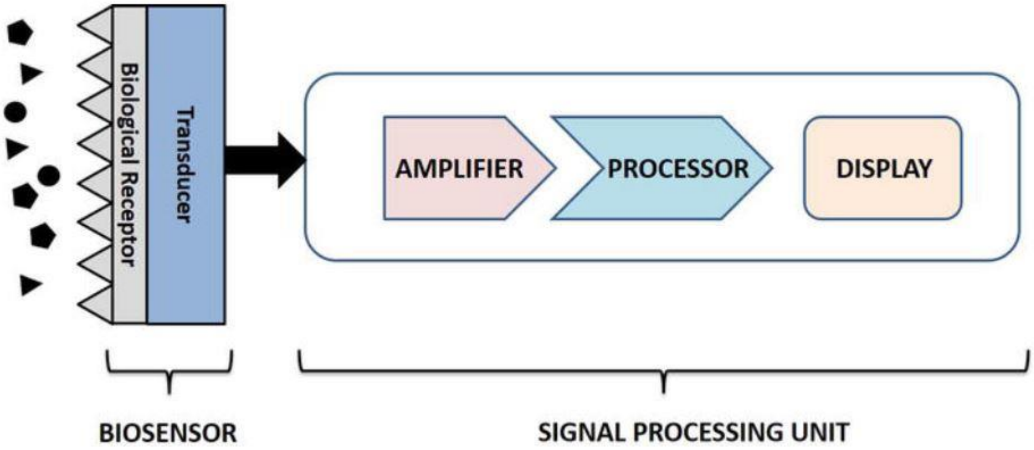

Figure 2-1. Biosensor principle, depicting the components necessary for signal generation: a biological receptor, a transducer, an amplifier, a processor and a display.[6]

There are many different types of transducers, including electrochemical (potentiometric, amperometric or conductimetric), optical, gravimetric and piezoelectric.[7] For example, a biocatalytic sensor based on a molecular recognition element can monitor a chemical conversion of an analyte into products. Whereas in an antibody/antigen interaction, the recognition is related to its affinity.[3] Some label-free transducers for antigen/antibody-based biosensors measure a change in resonance frequency (QMC), refractive index (RIU) or electrical impedance (EIS) upon the binding of these elements.[8]

Immunoassays are a specialized type of biosensors. Immunoassays are analytical methods for quantitative or qualitative analysis based on specific antigen-antibody interactions. Examples of immunoassays are electrophoretic immunoassay (EIA), enzyme-linked immunosorbent assay (ELISA), radioimmunoassay (RIA), fluorescence immunoassay (FIA), electrochemical immunoassay (ECIA), electrochemiluminescence immunoassay (ECLIA) and chemiluminescence immunoassay (CLIA).[9]

Immunoassays are used worldwide in many vital areas, such as diagnostics[10–12], drug monitoring[13,14], quality control[15] and clinical pharmacokinetics[16] and bioequivalence studies[17]. The widespread use of immunoassays methods is attributed to their specificity, high throughput and high selectivity for the analysis of a wide range of targets in biological samples.[18]

Immunoassays are classified as non-competitive (immunometric) and competitive, as shown in Figure 2-2. Non-competitive or immunometric immunoassays are commonly used for detection of proteins and viruses. They resolve two specific antibodies and are referred as a two-site or sandwich assay.[19] Figure 2-2A depicts this design, where immobilized antibodies are in excess and they capture the analyte that binds to one of its epitopes. Next, a second labeled antibody binds to the analyte. The second antibody is conjugated with a detection molecule (enzyme or fluorophore). The analyte molecules generate an optical signal that can be read out by colourimetry, chemiluminescence, or fluorescence. The magnitude of the optical signal is directly related to the antigen concentration. Competitive immunoassays are commonly used for small molecule detection. These assays are based on the competition between an labeled (tracer) and non-labeled analyte for a limited number of available antibody sites, as depicted in Figure 2-2 B.[20] The analyte is added with a known amount of the tracer containing an enzyme or a fluorophore that generates a detectable signal. The signal is inversely correlated to the analyte concentration in this case.

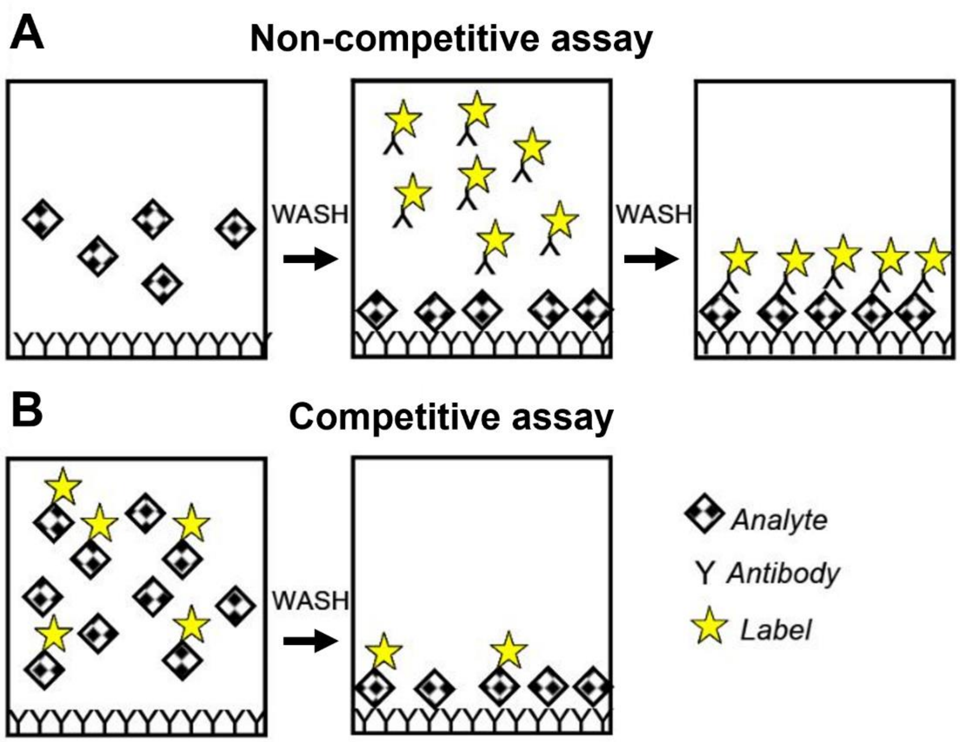

Figure 2-2. A) The non-competitive assay design where the amount of analyte is related to the signal generated by the detection molecule conjugated to the secondary antibody. The analyte is sandwiched between two antibodies. B) The competitive assay design where the signal is generated by a labeled analyte that competed for available sites with a non-labeled analyte.[21] [Used with permission from Reference 21]

Another common form of classification of immunoassays are homogenous or heterogeneous. Either homogeneous or heterogenous assays can be performed in competitive or non-competitive modalities.[18]

Homogeneous immunoassays distinguish between the free and the bound label used for detection without a physical separation step. The properties of a selected label is modified due to the binding to an antibody, causing a measurable increase or decrease in signal that is proportional to the analyte concentration in the matrix.[22] An example of a homogeneous immunoassay is based on Förster resonance energy transfer (FRET) as shown in Figure 2-3. This type of assay is based on a distance-dependent energy transfer from a donor to an acceptor; those are FRET compatible fluorescent dyes, fluorescent proteins or quantum dots (QDs).[23] The donor emission spectra overlaps with the acceptor absorption spectra and when they are positioned closely to each other (distance $R < 10$ nm) FRET happens (Figure 2-3 A).[8] A immunoassay can be constructed in such a way that FRET is only enabled when the donor molecules get close to the acceptor molecules due to the binding of the analyte to antibodies/antibody fragments, as depicted in Figure 2-3 B. In Figure 2-3 B, an analyte-specific Fab fragment, labelled with a donor fluorophore, forms an immunocomplex with a second analyte-specific Fab fragment, labeled with an acceptor fluorophore. FRET only happens when the analyte enables the formation of the immunocomplex. In the absence of the antibody-antigen interaction, the emission comes only from the fluorophore donor.[24] There are some drawbacks to this type of assay, such as autofluorescence of biological samples and photobleaching of fluorescent dyes for FRET.[24] This type of assay is most common for small molecule detection, such as morphine (opiate)[25], ochratoxin A[26] and deoxynivalenol[27] (food-contaminant mycotoxins).

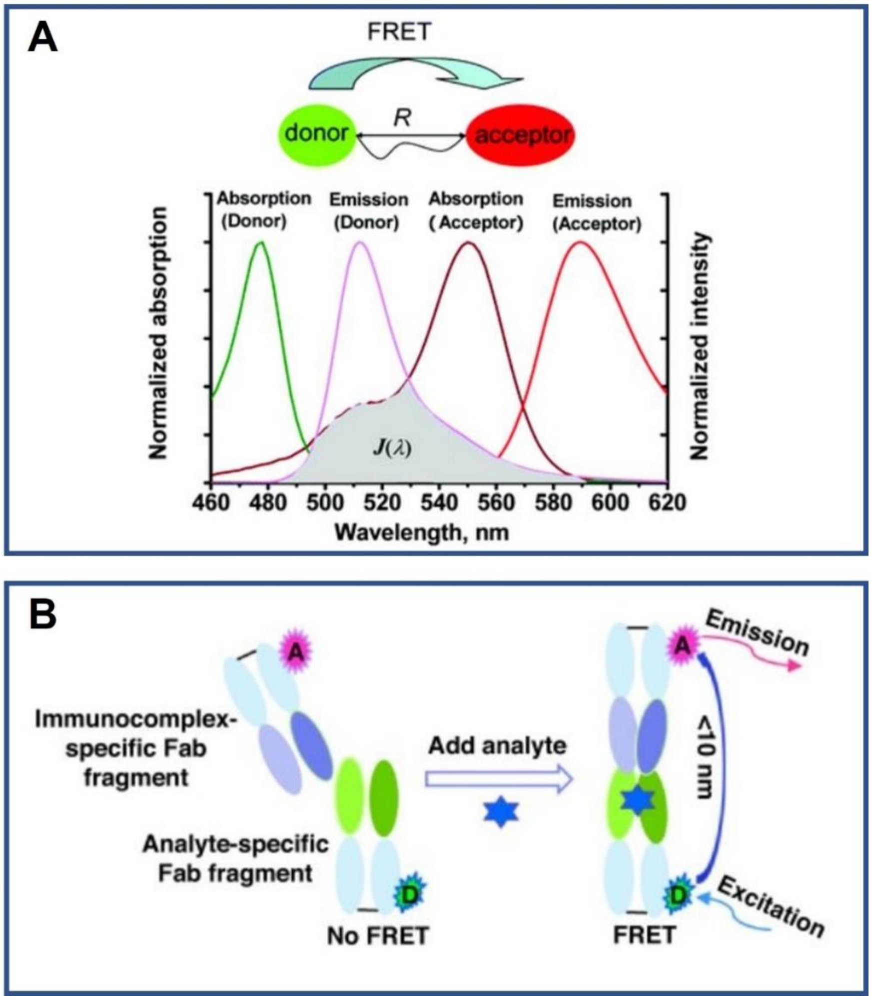

Figure 2-3. An example of homogeneous immunoassay, based on FRET. A) Schematics of the FRET process. A donor fluorophore is excited and transfers energy to an acceptor fluorophore at a distance R (<10 nm) through a nonradiative process. The acceptor releases the energy in either a fluorescent or nonradiative manner. J(λ) represents the degree of spectral overlap between the donor emission and the acceptor absorption. B) Schematics of a homogenous one-step FRET immunoassay for a small analyte. FRET occurs when the immunocomplex-specific Fab fragment binds to the primary Fab fragment-analyte complex bringing the donor and acceptor fluorophores to a distance R.[24,28] [Used with permission from Reference 24]

Heterogeneous immunoassays require physical separation of a labeled antigen/antibody complex from unbound components. Antibody/antigen binding is considered irreversible when k_1 (rate of the binding process) is much greater than k_{-1} (rate of dissociation).[22] This separation can occur through precipitation of antigen/antibody complexes with a precipitating chemical or crosslinking with other antibodies and analyzing the precipitate.[29] Antibodies can also be bound to a solid support and the removal of unbound components are done via various washes.[19] Enzyme-linked immunosorbent assay (ELISA) is an example of heterogenous assay (Figure 2-4).

ELISA is the predominant immunoassay method utilized today, and it is considered a gold standard for detection and quantification of protein biomarkers, antigens, antibodies, glycoproteins and hormones.[30,31] This method was developed by van Weeman and Schuurs in the late 1960s.[32] Figure 1-5 illustrates the different types of ELISA. There are three main types of ELISA: direct (Figure 2-4 A), indirect (Figure 2-4 B), and sandwich (Figure 2-4 C) assays, being the latter the most used method. The direct and indirect types are competitive and the sandwich is a non-competitive assay.[33]

ELISA has advantages such as high specificity and sensitivity, simultaneous analysis of samples, and ease of execution. However, ELISA has some drawbacks, such as being labour-intensive, time-consuming and results cannot be reassessed (endpoint assay).[34]

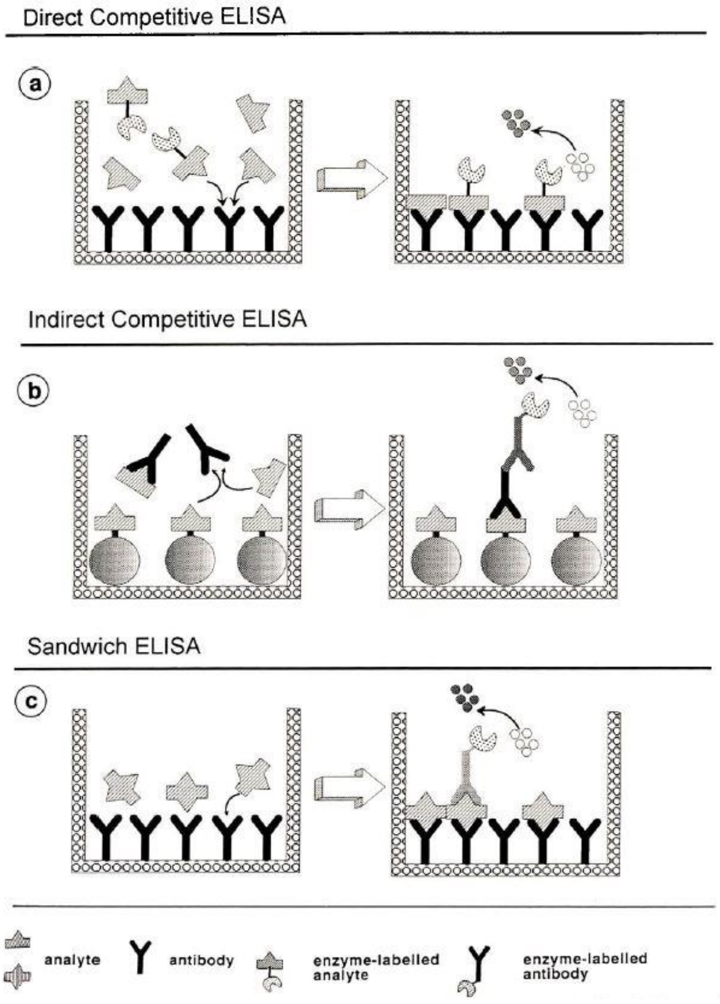

Figure 2-4. Illustration of the three main types of enzyme-linked immunosorbent assay (ELISA), a heterogeneous assay. A) Direct competitive, B) Indirect competitive and C) Sandwich.[35] [Used with permission from Reference 35]

Drawbacks with commonly used platforms in a clinical setting, such as ELISA and PCR have driven researchers to explore the development of plasmonic based sensors. This has led to a rise in the number of publications over the past 20 years. They can offer label-free and real-time molecular analysis with less reagent consumption.[36]

2.2 Plasmonic Biosensors

Biosensors can be classified based on the transducer principle, namely electrochemical (amperometric, conductimetric, impedance and potentiometric), piezoelectric, thermometric, magnetic and optical.[1] Optical biosensors exploit the interaction of the optical field with the biorecognition element. In an optical biosensor, the biorecognition element is conjugated with an optical transducer system.[37] The chemical or physical changes in the biorecognition elements induces a change in absorption, transmission, reflection, refraction, phase, amplitude, frequency or light polarization.[38] Among the optical biosensors, plasmonic-based sensors have advantages such as low limit-of-detection (LOD), broad linear range, high sensitivity and selectivity that make them ideal candidates for POC devices.[39]

The field of plasmonics is based on the interaction of light with free electrons of a noble metal and its in the crossroads of optics and nanotechnology.[40] Plasmonics are related to surface plasmons (SPs). SPs are the collective oscillations of free electrons confined evanescently on a metal surface.[41] SPs are of two kinds: i) localized SPs (LSPs) and ii) propagating SPs (PSPs; or plasmonic waveguide).[42] LSPs are confined to the surface of a metallic nanoparticle and PSPs propagate along the smooth continuous surface of a metal layer.[43] In LSPR, the length of the metallic nanostructure is smaller than the wavelength of the interacting light, resulting in non-propagating oscillations of free electrons. The associated electromagnetic field expands into the medium (around 30 nm) and decays exponentially (depicted in Figure 2-5 as δ_d).[45] Figure 2-5 A illustrates the classical example of LSPR, a single spherical gold nanoparticle excited by an external light field.[47] The LSPR phenomenon constrains the energy to the nanoparticle surface, magnifying the local electromagnetic field (light intensity). This effect underlies the principles for the mechanism for surface enhanced spectroscopy, such as surface-enhanced Raman scattering (SERS).[46] PSPs are traveling optical waves along a dielectric metal boundary and penetrate about 10 nm into the metal and more than 100 nm along the dielectric material [44] The optical waves propagate until the energy dissipates either by heat loss or radiation into free space.[42] Figure 2-5 B depicts the Kretschmann configuration, the most common scheme for prism coupling.[47]

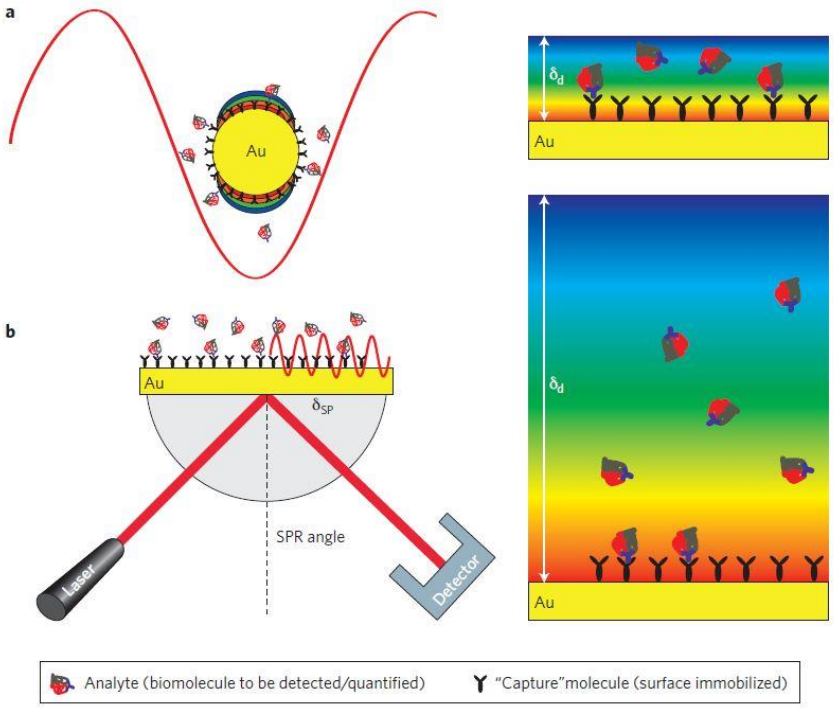

Figure 2-5. The fundamentals of LSPR vs. SPR. A) The particle diameter is much smaller than the wavelength of the incident light. The decay of the plasmon field (δ_d) is of the order of 30 nm. B) Depiction of a Kretschmann configuration, in which the PSPs propagate parallel to the surface of the metal film. The decay of the plasmon field (δ_d) is of the order of 100 nm. In the colour gradients, red represents more intense field enhancement and blue less intense.[47] [Used with permission from Reference 47]

The difference in the decay length of the plasmon field reflects on the strategies used to develop biosensors based on these SPs. Figure 2-6 summarizes the main differences in SPR and LSPR-based sensors, using as an example viral detection, but the same features are involved in other bio-analytes such as proteins, DNA and bacteria.[48] SPR biosensors are usually constituted by a prism bonded to a metal film in a Kretschmann configuration, first demonstrated in 1983 by Nylander and Liedberg.[49,50] The light passes though a dielectric prism, under total reflection and onto the thin metal film evaporated onto a glass containing the analyte.[51] The properties of the thin metal film are important for a highly sensitive detection of analytes.

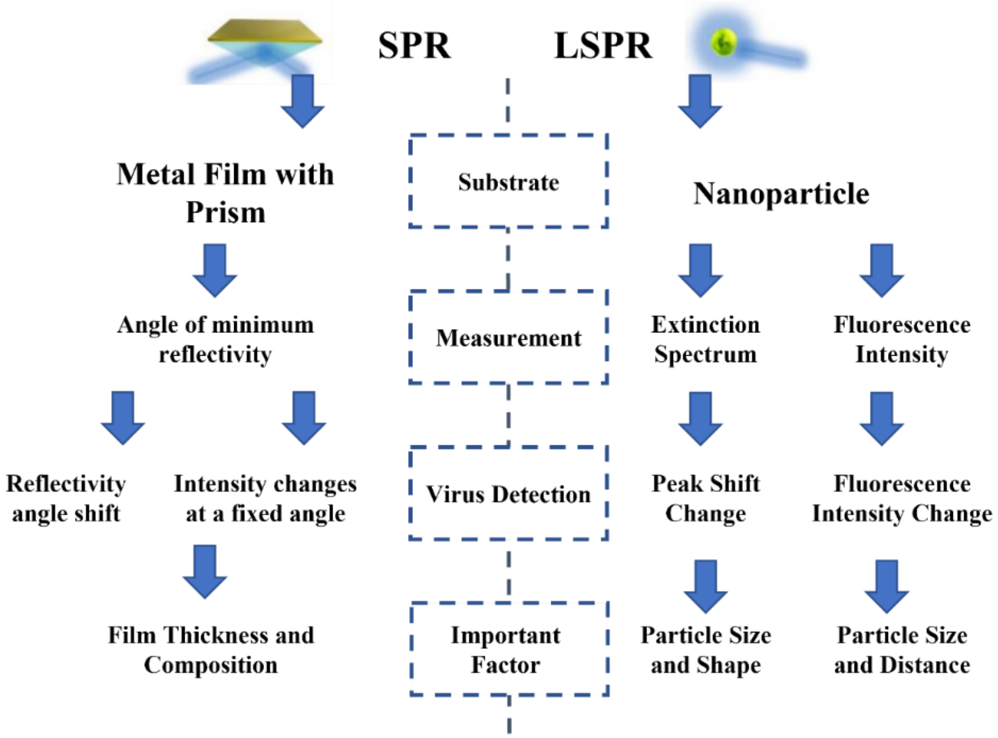

Figure 2-6. Summary of differences of substrate, measurement methods, and relevant factors in the construction of SPR and LSPR- based biosensors with viral detection as an example.[48]

A schematic of this SPR-based biosensor is shown in Figure 2-7 A. The interacting light is totally internally reflected and the SPR effect results in a sharp resonant dip in the reflected light at a distinct angle (θ).[44] Changes in the interface due to binding to the recognition elements cause a change in refractive index resulting in change of the optimal angle for excitation. The changes in the optical properties of the medium can be monitored as changes in wavelength, intensity, phase, or angle of incidence (Figure 2-7 B).[52] In the example of Figure 2-7, the quantification is related to the adsorption and dissociation of analyte to the recognition elements in real-time (Figure 2-7 C).[53]

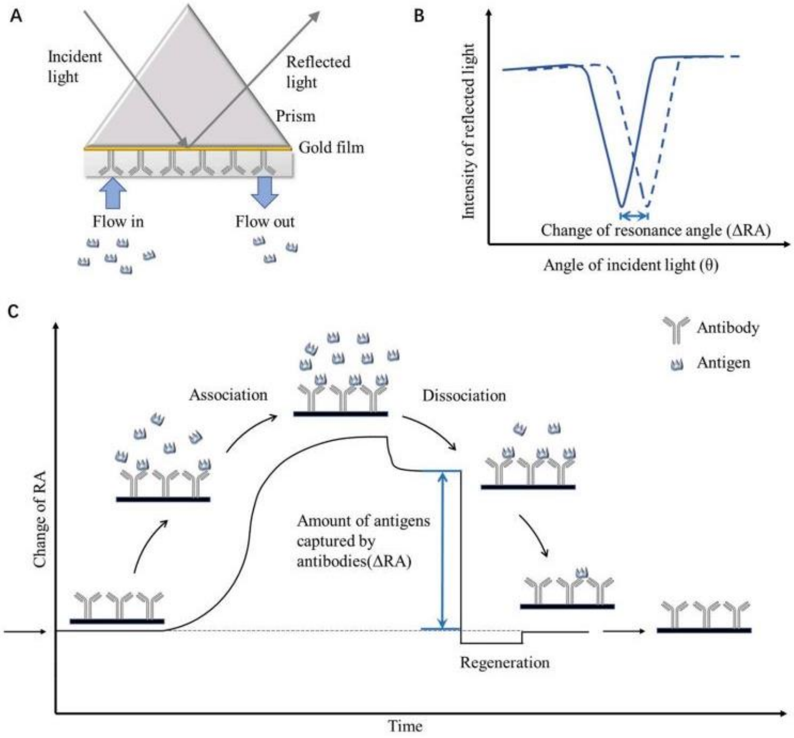

Figure 2-7. The SPR principle used in biosensor for a food allergen detection. A) A schematic of a Kretschmann-type prism coupling configuration. B) Monitoring of the change in signal upon binding of an analyte. C) Real-time sensorgram of the binding events of the analyte to the recognition elements.[53] [Used with permission from Reference 53]

In 1993, Jorgenson and Yee reported the first SPR arrangement using a optical-fiber rather than a prism.[44] Figure 2.8 shows a scheme of an optical fiber SPR sensor. In this sensor, the prism, arranged in a Kretschmann configuration, was replaced by the core of an optical fiber [54] In a standard SPR optic fiber sensor the cladding in the core of the sensing area is etched and coated with a thin metal layer, usually Au or Ag which can have an additional coat with a buffer layer. Lastly, there is a sensing layer. The light input is coupled to one of the ends of the fiber and the modulated light is perceived at the other end. The light has then information after interaction with the sensing layer. The sensing efficiency depends on the metal layer properties, optical fiber geometry and light wavelength.[44]

Optical fiber SPR sensors have advantages over the prism-based SPR sensors such as being of simple and robust design, flexible, capable of in-situ monitoring and continuous analysis.[55] Additionally, they have high degree of miniaturization, low cost and can be deployed in remote areas.[56]

For LSPR, the strong plasmons generated locally on the nanoparticles are used as a signal or as an enhancer for intensity of fluorescence materials or Raman probes.[48] The nanoparticle shape and size are important parameters that are related to the localization of the plasmons and are therefore related to the intensity of the signal. This dissertation focuses on SERS and LSPR-based immunoassays. Two sections will be dedicated to providing some background for those techniques in this document, under Application of Plasmonics in Biosensing, 2.3.1 and 2.3.2, respectively.

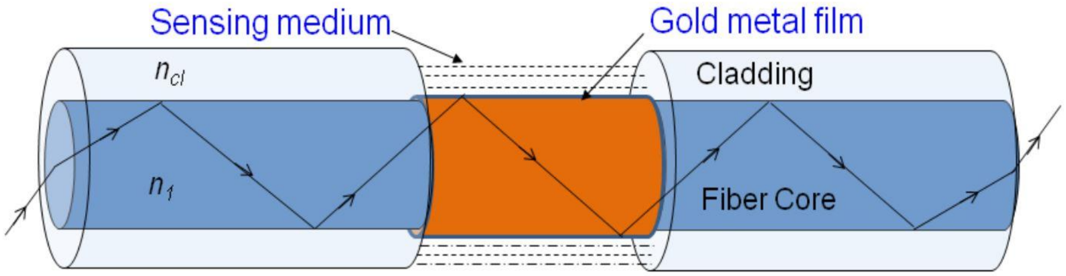

Figure 2-8. Optical fiber SPR sensor. The cladding of a portion of an optical fiber is removed followed by coating with a thin metal layer. The evanescent field of the light guided into the optical fiber excites surface plasmons at the metal coated region, that interacts with the medium to be sensed.[54]

SPR sensors are routinely used for food quality[57,58], fuel adulteration[59,60], pregnancy test[61], temperature monitoring[62,63], alcohol detection[64,65], smartphone diagnosis/telemedicine[66–69], bioimaging[70–72] and medical diagnosis[73–75]. For pathogen detection SPR has been used to detect leptospirosis[76], dengue virus E protein[77], SARS-CoV-2[78,79], hepatitis B[80], *vibrio fischeri*[81] , pseudomonas[82], rotavirus[83], Epstein-Barr virus[84], *Escherichia coli*[85], foot-and-mouth disease virus[86], among others[87]. Early disease detection, especially for cancer markers are being constantly developed and improved.[88–92]

2.3 Application of Plasmonics in Biosensing

The major plasmonics methods utilized for construction of immunosensors are SERS (Surface-Enhanced Raman Scattering), SPR (surface plasmon resonance), LSPR (localized surface plasmon resonance), SEF (surface-enhanced fluorescence) and SEIRA (surface-enhanced infrared absorption spectroscopy).[39] They have been used for detection of viral particles[18], proteins[93], food allergens[53], mycotoxins[94], among others[44]. In this dissertation, our focus is on immunoassays utilizing SERS and LSPR.

2.3.1 Surface-enhanced Raman Spectroscopy (SERS)

Surface-enhanced Raman spectroscopy (SERS) is the enhancement of the Raman signal, first reported in 1974 for pyridine adsorbed on roughened silver electrodes.[95] The SERS effect has electromagnetic (EM)[96] and charge-transfer (CT)[97] contributions to the overall intensification of the Raman response. The EM enhancement is generally the dominant mechanism in the SERS enhancement and involves the localization and amplification of the optical excitation by surface plasmon resonances (SPRs).[98] Molecules adsorbed within the plasmon field experience an increased electric field (light intensity) contribution to the induced polarization, thereby enhancing the Raman scattering.[99] The enhancement attributed to EM fields are commonly in the order of 10^4-10^8 [99–101], with the highest recorded up to 10^{14}.[102,103] The CT mechanism is the grouping of the resonant and non-resonant electronic processes between the adsorbed molecules and the nanoparticle surface, dependent on the laser excitation wavelength and site of attachment.[99]

Adrian[104] and Lippitsch[105] described two distinct CT models in the 1980's, namely the excited-state charge-transfer and the ground-state charge-transfer model, respectively. In the excited-state charge-transfer, a charge-transfer complex is formed by chemical bonding between the probe molecules and the metallic substrate, causing a substantial change in the intrinsic polarizability of the probed molecule.[106] The molecule/substrate complex creates new electronic states in resonance with the excitation laser, enhancing the Raman signal.[107] In the ground-state charge-transfer model, the probed molecules do not form a chemical bond with the metallic substrate. The charge transfer happens when both are in the ground state and it depends on the electronic structure of the probed molecule itself.[106,107] The CT enhancement contributions are in the order of 10-10^3.[108,109] An incremental enhancement of 10^2-10^4 is achieved when the maximum absorbance of the Raman scatterer is close to or in resonance with the wavelength of the exciting laser, termed surface-enhanced resonance Raman spectroscopy (SERRS).[99] This process is attributed to the large SERS cross sections of resonant molecules, e.g dyes such as Rhodamine 6G excited with green laser.[110]

SERS/SERRS have high sensitivity allowing even single-molecule detection. The method is non-destructive and possesses vibrational chemical specificity (fingerprint), allowing for direct detection of target analytes.[111] Fluorescence-based assays are by far the most employed in optical biosensors. The sensor response can be based on fluorescence intensity, lifetime, anisotropy, quenching efficiency, non-radiative and luminescent energy transfer.[112] Individual spectral lines in Raman are, on average, 10-100 times narrower than the emission profiles of fluorescent compounds. The highly resolved spectra promotes multiplex ability for SERS-based sensors.[99] Additionally, Raman-active reporters are less prone to photobleaching compared to fluorescent ones.[113] It has been reported that SERS is more intense and stable compared to fluorescence in the single-molecule regimen.[103] Additionally, Raman is performed in the visible, and near-infrared spectral range (400 - 1064 nm), making it ideal for aqueous environment and therefore, biomatrices.[114] These characteristics makes the use of SERS/SERRS an interesting tool for immunoassay development.

2.3.2 SERS-based Immunoassays

There are several reports on the development of immunoassays based on SERS.[115–117] The development of SERS-based immunoassays requires two critical components: 1) the substrate modified with targeting molecules (i.e. antibodies, aptamers); and 2) an external reporter label (ERL).[118]

The ERLs specifically recognize and bind to the analytes captured by the functionalized substrate and provide SERS/SERRS signals for the quantitative detection of the analytes. SERS-based immunoassays can be classified as heterogenous, homogeneous, competitive, and non-competitive, in a similar fashion as aforementioned (Figure 2-2), but with the employment of an ERL as element of detection rather than fluorescence/colorimetry probes. Moving forward, the focus will be on the sandwich scheme, which rivals with the most used type of ELISA, and it is the main topic in Chapters 3 and 4. amino or carboxylic acid type of SERS immunoassay. In Figure 2-9A the substrate, in this example a gold (Au) covered slide, is modified with a linker molecule that serve to anchor the antibodies to the substrate. The linker can contain, for example, thiol groups, since sulphur strongly interact with Au.[119] Next, capture antibodies are attached to the substrate via linker. The linker can contain, for example, carboxyl groups that form amide bonds with primary amides present in the antibodies, via N-ethyl-N′-(3-(dimethylamino)propyl)carbodiimide (EDC)/ N-hydroxysuccinimide (NHS) conjugation.[120]

The ERLs (Figure 2-9B) is a plasmonic core, typically spherical gold nanoparticles, modified with a Raman label or reporter and a detection antibody.[121] The assay is conducted (Figure 2-9C) by adding the analyte, present in aqueous matrix or biological fluid to the substrate. After washing step(s), the ERL is added to the immunosensor. The analyte is then sandwiched between the substrate and the ERL. The final step is to interrogate the substrate by Raman measurements. The presence of the Raman adsorbed to the ERL surface (metallic nanoparticle) generates enhanced Raman signals (SERS/ SERRS), that are related to the amount of ERLs and therefore, to the amount of analytes captured.[122]

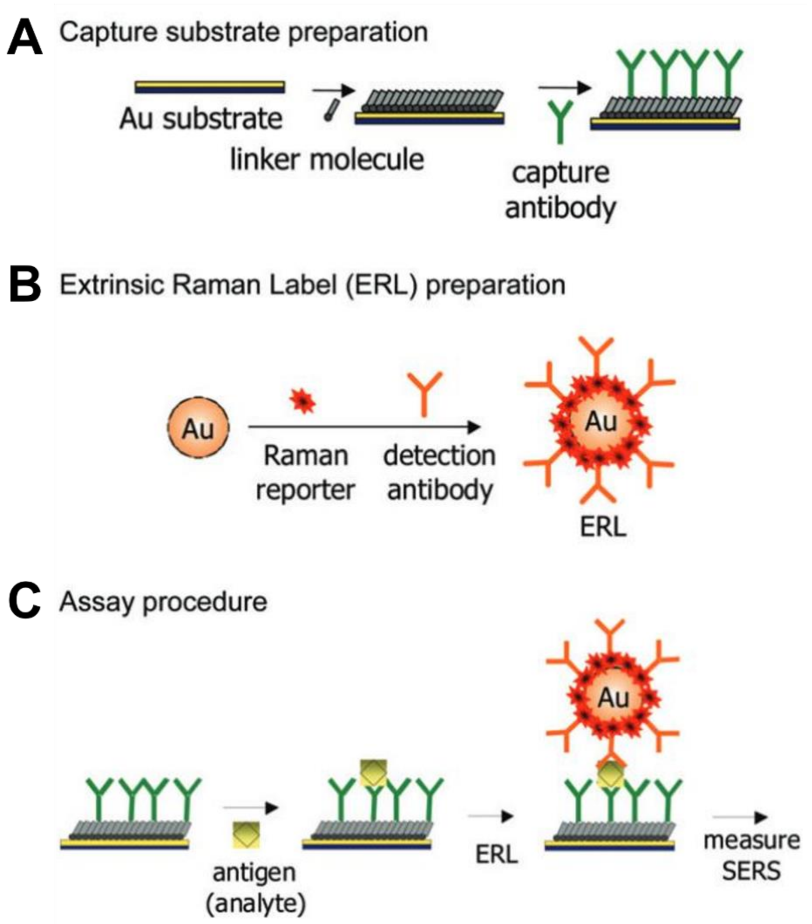

Figure 2-9. SERS-based immunoassay sandwich scheme. A) The substrate is functionalized with a capture antibody. B) The ERL is synthesized, and C) the assay is conducted, reaching a sandwiched analyte between the substrate and the ERL.[123] [Used with permission from Reference 123]

This SERS type of immunoassay has been used to detect hepatitis B virus with limits of detection (LOD) of 0.5 μg/mL[124], carcinoembryonic antigen with LOD of 10 pg/mL[125] and for Alzheimer's Tau[126] protein and prostate-specific antigen[127] in the femtomolar range. Our research group developed a SERS-based immunoassay, in a sandwich format, for zika virus (ZIKV) detection with LOD of 10 ng/mL, in 2015. At that time, ZIKV was a public health emergency and this sensor had LOD four orders of magnitude below the ELISA-based assays commercially available then.[128]

2.4 Localized Surface Plasmon Resonance (LSPR)

When metallic nanoparticles are irradiated by light, the oscillating electric field causes a collective oscillation of the metal's conduction electrons. This oscillation of the electron cloud is due to the Coulombic attraction between the negatively charged electrons and the positively charged nuclei and the repulsion among electrons that causes a restoring force to arise when the electron cloud is displaced relative to the nuclei. This displacement causes a dipole to arise. This phenomenon is called the dipole plasmon resonance or localized surface plasmon resonance (LSPR).[40]

Gustav Mie presented a solution to Maxwell's equations that described the extinction spectra (extinction spectra = scattering + absorption) of particles of arbitrary size. Mie's work, later coined Mie's theory, was the starting point for understanding the phenomena for other nanoparticles shapes. Some assumptions can be made for nanoparticles that are considerably smaller than the wavelength of the incoming light. Briefly, the propagating electric field is constant (or static) around the nanoparticle, and the LSPR response is governed by electrostatics rather than electrodynamics. These assumptions are referred to as quasistatic approximation and give rise to an equation that predicts the polarizability and extinction cross-section of spherical particles up to 100 nm in diameter.[40] In this approximation, the magnetic component is negligible, and only the electric component of the EM field is considered. The solution to Maxwell's equation for a quasistatic approximation have two components: the incident field term and an induced dipole term, which is proportional to the polarizability. The polarizability is a measure of the distortion of the electron cloud in response to an external field.[129] In other terms, it represents the ease in which charges distribute and form partial dipoles. The basis for surface plasmons in metallic nanoparticles can be understood by looking at the polarizability. Equation 2-1 defines the polarizability component, α, where ε_{in} and ε_{out} are the external and internal dielectric constants of the metal particle and a is the radius of the spherical particle.[130]

$$\alpha = \left(\frac{\varepsilon in - \varepsilon out}{\varepsilon in + 2\ \varepsilon out}\right) a^3 \qquad \text{Equation 2-1}$$

The internal dielectric constant, ε_{in}, is highly dependent on the wavelength of the incident light. When $\varepsilon_{in} = -2\ \varepsilon_{out}$, the electric field is enhanced compared to the incident field. When the dielectric constants are maximized, a peak (λmax) is observed in the extinction spectrum of the particles. For Au and Ag nanoparticles this resonance condition happens for wavelengths in the visible spectrum and is the basis for LSPR and EM field enhancement mechanism for SERS.[130]

2.5 LSPR-based Immunoassays

Surface plasmon resonance (SPR)[131] is found in materials with negative real and small positive imaginary dielectric constant (Equation 2-1), mainly gold, silver, and copper. The enhanced field surrounding the metallic nanoparticle is a result of the LSPR. The enhanced field decays exponentially away from the nanoparticle surface as seen in Figure 2-5. The LSPR is sensitive to the external dielectric environment in proximity to the surface. Therefore, adsorbate layers change this external environment and, consequently, the refractive index of the environment leading to a change in the LSPR resonance conditions that can be monitored.[130]

Equation 2-2 shows the dependency of the refractive index of the external medium with the shift of its resonant wavelength, where *na* is the refractive index of the adsorbate layer, *ne* is the refractive index of the bulk environment, *d* is the adsorbate layer thickness, and *ld* is the decay length of the electric field.

$$\Delta\lambda_{max} = m(n_a - n_e)[1 - exp(-\frac{2d}{l_d})] \qquad \text{Equation 2-2}$$

Immunoassays can then be constructed in a nanoparticle-coated platform monitored before and after interacting with the antigen of interest. Typically, discrete particles are attached to a solid support via covalent and/or noncovalent strategies. For immunoassays, an element of recognition (e.g antibodies) is then adhered to the anchored nanoparticles. Next, the assay is conducted, and the analytes interact with the elements of recognition. The measurements are usually conducted in transmission-mode configuration, as depicted in Figure 2-10.[132] The optical extinction (absorption plus scattering of the light) is measured before and after interaction with the analyte. The maximum of the optical extinction, λmax is accessed and the change in position is related to the concentration of analyte. The λmax does not change if there is no interaction with the analyte and it red shifts when it does.

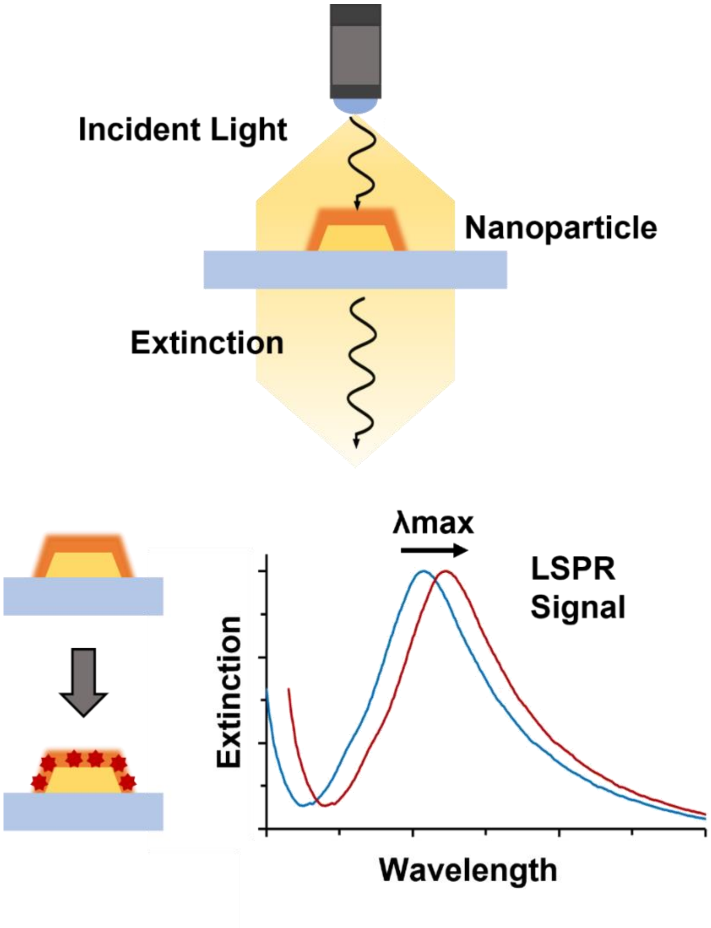

Figure 2-10. LSPR-based principle in biosensing. The anchored nanoparticles in a substrate are accessed before and after the analyte binding event. The change in the λmax of the LSPR signal is proportional to the analyte concentration.[132] [Used with permission from Reference 132]

The sensitivity of the LSPR sensor depends on the type of material, shape and size of the nanoparticle used in the platform. The sensitivity of a LSPR sensor is defined as the spectral shift of the peak wavelength ($\Delta\lambda$) resulted from a refractive index change (Δn) of the environment surrounding the nanostructure and is reported as refractive index units per nanometer (nm/RIU).[133]

For instance, Ag nanoparticles show a higher nm/RIU then Au nanoparticles and sharp Ag bipyramids have higher nm/RIU than rounded Ag bipyramids for the same size.[134] In contrast to spherical particles, nanoparticles with sharp tips and edges have high electromagnetic confinement and exhibit strong electromagnetic field enhancement.[135] Au nanostars show a higher nm/RIU compared to Au nanocubes and nanorods[136], whereas nanocubes have higher nm/RIU compared to nanospheres. Figure 2.11 shows an example of a LSPR wavelength shift for gold nanospheres (AuNS) and gold nanocubes (AuNC). Figure 2.11A and 2.11B shows the red shift of the LSPR scattering spectra for AuNS and AuNC, respectively with the change in the media from air to water and oil. The wavelength is plotted in relationship to the local refractive index (RI) in Figure 2.11C.[137]

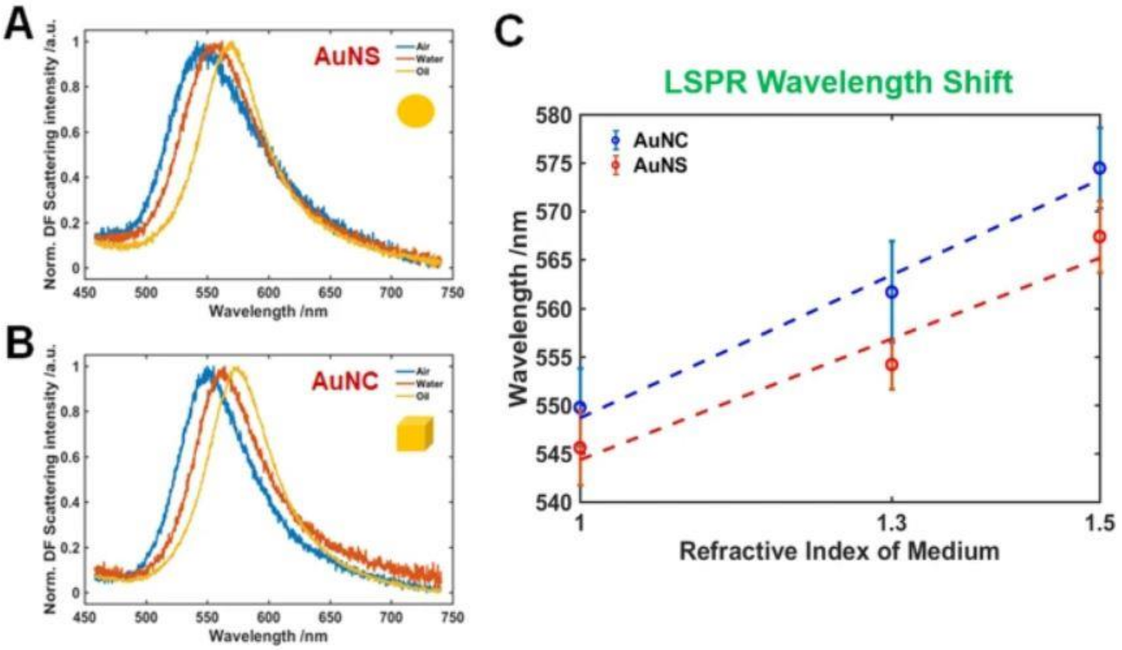

Figure 2-11. Change in LSPR scattering spectra for A) AuNS and B) AuNC in air, water, and oil. C) LSPR wavelength shifts for AuNS (red) and AuNC (blue) as a function of local RI of the medium.[137] [Open access from reference 137]

LSPR-based sensors can also be constructed with fiber optics, in a similar manner as the optical fiber SPR sensor (Figure 2.8). Figure 2-12 depicts this configuration. A portion of the optical fiber cladding is stripped and covered with a monolayer made of metal nanoparticles, surrounded by the sensing medium. Resonant plasmons are excited on the metallic nanoparticles by the evanescent field of the light that is guided inside the fiber. A portion of the guided spectral range is absorbed by the nanoparticle layer and a peak is observed in the absorption spectrum of transmitted optical power.[54]

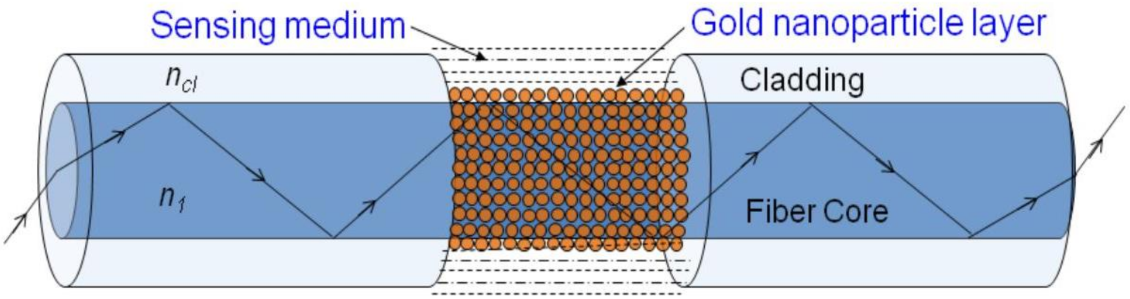

Figure 2-12. Schematic of a LSPR-based fiber optic sensor. A portion of the optical fiber cladding is stripped and covered with metallic nanoparticles.[54]

In our research group, a LSPR-based plastic strip platform was developed for biosensing.[138] Figure 2-13 shows a schematic of the strip preparation. A plastic strip made of a common plastic, polyethylene terephthalate (PET), is activated via plasma, inserting amino groups into the strip's surface. Next, the strips are incubated with AgNPs and further modified by either amino or carboxylic acid groups, using (3-aminopropyl) trimethoxysilane (APTMS) or 3-aminopropanoic acid (APA), respectively. These groups are further modified for protein/antibody conjugation via EDC/NHS conjugation. The strips were conjugated with IgG antibodies and detected anti-IgG with linear response in the range 9.5 – 189.4 nM. The LOD was estimated as 3.5 nM.

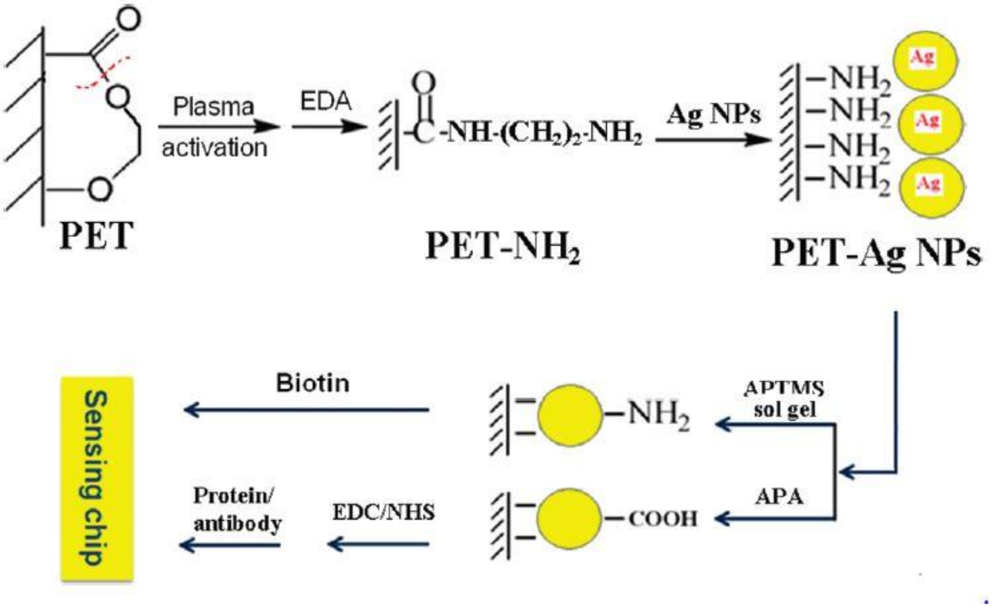

Figure 2-13. Steps on the fabrication of a LSPR-based biosensor. The plastic is modified via plasma activation to adhere silver nanoparticles on its surface, followed by conjugation of a recognition element.[138] [Used with permission from Reference 138]

2.6 References

(1) Justino, C. I. L.; Rocha-Santos, T. A.; Duarte, A. C.; Rocha-Santos, T. A. Review of Analytical Figures of Merit of Sensors and Biosensors in Clinical Applications. TrAC Trends in Analytical Chemistry 2010, 29 (10), 1172–1183.

(2) Murugaiyan, S. B.; Ramasamy, R.; Gopal, N.; Kuzhandaivelu, V. Biosensors in Clinical Chemistry: An Overview. Adv Biomed Res 2014, 3, 67.

(3) Stradiotto, N. R.; Yamanaka, H.; Zanoni, M. V. B. Electrochemical Sensors: A Powerful Tool in Analytical Chemistry. J. Braz. Chem. Soc. 2003, 14, 159–173..

(4) Giarola, J. de F.; Souto, D. E. P.; Kubota, L. T. Evaluation of PAMAM Dendrimers (G3, G4, and G5) in the Construction of a SPR-Based Immunosensor for Cardiac Troponin T. ANAL. SCI. 2021, 37 (7), 1007–1013.

(5) Malhotra, B. D.; Ali, Md. A. Nanomaterials in Biosensors. Nanomaterials for Biosensors 2018, 1–74.

(6) Tetyana, P.; Shumbula, P. M.; Njengele-Tetyana, Z.; Tetyana, P.; Shumbula, P. M.; Njengele-Tetyana, Z. Biosensors: Design, Development and Applications; IntechOpen, 2021.

(7) Yamanaka, K.; Vestergaard, M. C.; Tamiya, E. Printable Electrochemical Biosensors: A Focus on Screen-Printed Electrodes and Their Application. Sensors (Basel) 2016, 16 (10), 1761.

(8) Zeng, X.; Shen, Z.; Mernaugh, R. Recombinant Antibodies and Their Use in Biosensors. Anal Bioanal Chem 2012, 402 (10), 3027–3038.

(9) Guo, Z.; Sha, Y.; Hu, Y.; Wang, S. In-Electrode vs. on-Electrode: Ultrasensitive Faraday Cage-Type Electrochemiluminescence Immunoassay. Chemical Communications 2016, 52 (25), 4621–4624.

(10) Findlay, J. W. A.; Smith, W. C.; Lee, J. W.; Nordblom, G. D.; Das, I.; DeSilva, B. S.; Khan, M. N.; Bowsher, R. R. Validation of Immunoassays for Bioanalysis: A Pharmaceutical Industry Perspective. Journal of Pharmaceutical and Biomedical Analysis 2000, 21 (6), 1249–1273.

(11) Kobayashi, N.; Kubota, K.; Oiwa, H.; Goto, J.; Niwa, T.; Kobayashi, K. Idiotype-Anti-Idiotype-Based Noncompetitive Enzyme-Linked Immunosorbent Assay of

Ursodeoxycholic Acid 7-N-Acetylglucosaminides in Human Urine with Subfemtomole Range Sensitivity. J Immunol Methods 2003, 272 (1–2), 1–10.

(12) Karakulova, I. V.; Shutov, A. A. [Quantitative determination of serum serotonin in the diagnosis of tension headache]. Klin Lab Diagn 2006, No. 1, 9–10.

(13) Clarke, W. Immunoassays for Therapeutic Drug Monitoring and Clinical Toxicology. In Handbook of Analytical Separations; Elsevier, 2020; Vol. 7, pp 97–114.

(14) Broto, M.; McCabe, R.; Galve, R.; Marco, M.-P. A High-Specificity Immunoassay for the Therapeutic Drug Monitoring of Cyclophosphamide. Analyst 2019, 144 (17), 5172–5178.

(15) Grandke, J.; Oberleitner, L.; Resch-Genger, U.; Garbe, L.-A.; Schneider, R. J. Quality Assurance in Immunoassay Performance—Comparison of Different Enzyme Immunoassays for the Determination of Caffeine in Consumer Products. Anal Bioanal Chem 2013, 405 (5), 1601–1611.

(16) Woodbury, N.; Bald, E.; Geist, B.; Yang, T.-Y. Application of Multiplexed Pharmacokinetic Immunoassay to Quantify in Vivo Drug Forms and Coadministered Biologics. Bioanalysis 2019, 11 (24), 2251–2268.

(17) Cassidy, J. P.; Luzio, S. D.; Marino, M. T.; Baughman, R. A. Quantification of Human Serum Insulin Concentrations in Clinical Pharmacokinetic or Bioequivalence Studies: What Defines the "Best Method"? Clinical Chemistry and Laboratory Medicine 2012, 50 (4), 663–666.

(18) Darwish, I. A. Immunoassay Methods and Their Applications in Pharmaceutical Analysis: Basic Methodology and Recent Advances. Int J Biomed Sci 2006, 2 (3), 217–235.

(19) O’Kennedy, R.; Murphy, C. Immunoassays: Development, Applications and Future Trends; Pan Stanford publishing: Singapore, 2017.

(20) Wang, X.; Cohen, L.; Wang, J.; Walt, D. R. Competitive Immunoassays for the Detection of Small Molecules Using Single Molecule Arrays. J. Am. Chem. Soc. 2018, 140 (51), 18132–18139.

(21) Ylikotila, J. HIGHLY FUNCTIONAL BINDING SURFACE FOR MINIATURISED SOLID-PHASE IMMUNOASSAYS – A SPOT STORY – .2009.Tampereen yliopisto Tampere University, PhD dissertation .

(22) Clarke, W.; Sokoll, L. J.; Rai, A. J. Immunoassays. In Contemporary Practice in Clinical Chemistry; Elsevier, 2020; pp 201–214.

(23) Bajar, B. T.; Wang, E. S.; Zhang, S.; Lin, M. Z.; Chu, J. A Guide to Fluorescent Protein FRET Pairs. Sensors (Basel) 2016, 16 (9), 1488.

(24) Takkinen, K.; Žvirblienė, A. Recent Advances in Homogenous Immunoassays Based on Resonance Energy Transfer. Current Opinion in Biotechnology 2019, 55, 16–22.

(25) Pulli, T.; Höyhtyä, M.; Söderlund, H.; Takkinen, K. One-Step Homogeneous Immunoassay for Small Analytes. Anal. Chem. 2005, 77 (8), 2637–2642.

(26) Li, T.; Jeon, K.-S.; Suh, Y. D.; Kim, M.-G. A Label-Free, Direct and Noncompetitive FRET Immunoassay for Ochratoxin A Based on Intrinsic Fluorescence of an Antigen and Antibody Complex. Chem. Commun. 2011, 47 (32), 9098–9100.

(27) Goryacheva, O. A.; Beloglazova, N. V.; Goryacheva, I. Y.; De Saeger, S. Homogenous FRET-Based Fluorescent Immunoassay for Deoxynivalenol Detection by Controlling the Distance of Donor-Acceptor Couple. Talanta 2021, 225, 121973.

(28) Wu, L.; Huang, C.; P. Emery, B.; C. Sedgwick, A.; D. Bull, S.; He, X.-P.; Tian, H.; Yoon, J.; L. Sessler, J.; D. James, T. Förster Resonance Energy Transfer (FRET)-Based Small-Molecule Sensors and Imaging Agents. Chemical Society Reviews 2020, 49 (15), 5110–5139.

(29) Price, C. P.; Spencer, K.; Whicher, J. Light-Scattering Immunoassay of Specific Proteins: A Review. Ann Clin Biochem 1983, 20 (1), 1–14.

(30) Thiha, A.; Ibrahim, F. A Colorimetric Enzyme-Linked Immunosorbent Assay (ELISA) Detection Platform for a Point-of-Care Dengue Detection System on a Lab-on-Compact-Disc. Sensors (Basel) 2015, 15 (5), 11431–11441.

(31) Alhajj, M.; Farhana, A. Enzyme Linked Immunosorbent Assay. In StatPearls; StatPearls Publishing: Treasure Island (FL), 2021.

(32) Van Weemen, B. k.; Schuurs, A. h. w. m. Immunoassay Using Antigen—Enzyme Conjugates. FEBS Letters 1971, 15 (3), 232–236.

(33) Vashist, S. K.; Luong, J. H. T. Enzyme-Linked Immunoassays. In Handbook of Immunoassay Technologies; Elsevier, 2018; pp 97–127.

(34) Sakamoto, S.; Putalun, W.; Vimolmangkang, S.; Phoolcharoen, W.; Shoyama, Y.; Tanaka, H.; Morimoto, S. Enzyme-Linked Immunosorbent Assay for the Quantitative/Qualitative Analysis of Plant Secondary Metabolites. J Nat Med 2018, 72 (1), 32–42.

(35) Aspland, J. R.; Hennion, M.-C. Immunochemical Methods and Biosensors. In Techniques and Instrumentation in Analytical Chemistry; Elsevier, 1997; Vol. 19, pp 429–517.

(36) Soler, M.; Huertas, C. S.; Lechuga, L. M. Label-Free Plasmonic Biosensors for Point-of-Care Diagnostics: A Review. Expert Review of Molecular Diagnostics 2019, 19 (1), 71–81.

(37) Damborský, P.; Švitel, J.; Katrlík, J. Optical Biosensors. Essays Biochem 2016, 60 (1), 91–100.

(38) Naresh, V.; Lee, N. A Review on Biosensors and Recent Development of Nanostructured Materials-Enabled Biosensors. Sensors 2021, 21 (4), 1109.

(39) Shrivastav, A. M.; Cvelbar, U.; Abdulhalim, I. A Comprehensive Review on Plasmonic-Based Biosensors Used in Viral Diagnostics. Commun Biol 2021, 4 (1), 1–12.

(40) Plasmonics: From Basics to Advanced Topics; Enoch, S., Bonod, N., Eds.; Springer Series in Optical Sciences; Springer Berlin Heidelberg: Berlin, Heidelberg, 2012; Vol. 167.

(41) Zhang, Z.; Fang, Y.; Wang, W.; Chen, L.; Sun, M. Propagating Surface Plasmon Polaritons: Towards Applications for Remote-Excitation Surface Catalytic Reactions. Advanced Science 2016, 3 (1), 1500215.

(42) Cao, E.; Lin, W.; Sun, M.; Liang, W.; Song, Y. Exciton-Plasmon Coupling Interactions: From Principle to Applications. Nanophotonics 2018, 7 (1), 145–167.

(43) Yun, H.; Lee, I.-M.; Lee, S.-Y.; Kim, K.-Y.; Lee, B. Intermediate Plasmonic Characteristics in a Quasi-Continuous Metallic Monolayer. Sci Rep 2014, 4 (1), 3696.

(44) Butt, M. A.; Khonina, S. N.; Kazanskiy, N. L. Plasmonics: A Necessity in the Field of Sensing-A Review (Invited). Fiber and Integrated Optics 2021, 40 (1), 14–47.

(45) Kaminska, I.; Maurer, T.; Nicolas, R.; Renault, M.; Lerond, T.; Salas-Montiel, R.; Herro, Z.; Kazan, M.; Niedziolka-Jönsson, J.; Plain, J.; Adam, P.-M.; Boukherroub, R.; Szunerits, S. Near-Field and Far-Field Sensitivities of LSPR Sensors. J. Phys. Chem. C 2015, 119 (17), 9470–9476.

(46) Hong, W.; Lan, J.; Li, H.; Yan, Z.; Li, Y.; Jiang, H.; Chen, M. Towards an Understanding of the Localized Surface Plasmon Resonance Decay Pathways in Bimetallic Core–Shell Nanoparticles. Optics & Laser Technology 2022, 146, 107565.

(47) Read, T.; Olkhov, R. V.; Shaw, A. M. Measurement of the Localised Plasmon Penetration Depth for Gold Nanoparticles Using a Non-Invasive Bio-Stacking Method. Phys. Chem. Chem. Phys. 2013, 15 (16), 6122–6127.

(48) Takemura, K. Surface Plasmon Resonance (SPR)- and Localized SPR (LSPR)-Based Virus Sensing Systems: Optical Vibration of Nano- and Micro-Metallic Materials for the Development of Next-Generation Virus Detection Technology. Biosensors 2021, 11 (8), 250.

(49) (16) Brolo, A. G. Plasmonics for Future Biosensors. *Nature Photon* **2012**, *6* (11), 709–713. (50) Liedberg, B.; Nylander, C.; Lunström, I. Surface Plasmon Resonance for Gas Detection and Biosensing. Sensors and Actuators 1983, 4, 299–304.

(51) Vinogradov, A. P.; Dorofeenko, A. V.; Pukhov, A. A.; Lisyansky, A. A. Exciting Surface Plasmon Polaritons in the Kretschmann Configuration by Light Beam.

(52) Griffin, G. D.; Stratis-Cullum, D. N.; McKnight, T. E. Biosensors☆. In Encyclopedia of Microbiology (Fourth Edition); Schmidt, T. M., Ed.; Academic Press: Oxford, 2019; pp 542–574.

(53) Zhou, J.; Qi, Q.; Wang, C.; Qian, Y.; Liu, G.; Wang, Y.; Fu, L. Surface Plasmon Resonance (SPR) Biosensors for Food Allergen Detection in Food Matrices. Biosensors and Bioelectronics 2019, 142, 111449.

(54) Srivastava, S. K. Fiber Optic Plasmonic Sensors: Past, Present and Future. TOOPTSJ 2013, 7 (1), 58–83.

(55) Odacı, C.; Aydemir, U. The Surface Plasmon Resonance-Based Fiber Optic Sensors: A Theoretical Comparative Study with 2D TMDC Materials. Results in Optics 2021, 3, 100063.

(56) Wieduwilt, T.; Kirsch, K.; Dellith, J.; Willsch, R.; Bartelt, H. Optical Fiber Micro-Taper with Circular Symmetric Gold Coating for Sensor Applications Based on Surface Plasmon Resonance. Plasmonics 2013, 8 (2), 545–554.

(57) Tseng, S.-Y.; Li, S.-Y.; Yi, S.-Y.; Sun, A. Y.; Gao, D.-Y.; Wan, D. Food Quality Monitor: Paper-Based Plasmonic Sensors Prepared Through Reversal Nanoimprinting for Rapid Detection of Biogenic Amine Odorants. ACS Appl. Mater. Interfaces 2017, 9 (20), 17306–17316.

(58) Thenmozhi, H.; Mani Rajan, M. S.; Ahmed, K. D-Shaped PCF Sensor Based on SPR for the Detection of Carcinogenic Agents in Food and Cosmetics. Optik 2019, 180, 264–270.

(59) Ahmed, K.; Jabin, Md. A.; Paul, B. K. Surface Plasmon Resonance-Based Gold-Coated Biosensor for the Detection of Fuel Adulteration. J Comput Electron 2020, 19 (1), 321–332.

(60) Yang, L.; Shi, Y.; Yi, Z.; Song, X.; Lv, J.; Chu, P. K.; Liu, C. Detection of Kerosene Adulteration in Automobile Fuel by a Low-Loss Surface Plasmon Resonance (SPR) Chemical Sensor. Anal. Methods 2022, 14 (22), 2153–2160.

(61) Mitu, S. A.; Ahmed, K.; Zahrani, F. A. A.; Grover, A.; Mani Rajan, M. S.; Moni, M. A. Development and Analysis of Surface Plasmon Resonance Based Refractive Index Sensor for Pregnancy Testing. Optics and Lasers in Engineering 2021, 140, 106551.

(62) Yang, X.; Zhu, L.; Dong, M.; Yao, J. Multiplex Localized Surface Plasmon Resonance Temperature Sensor Based on Grapefruit Fiber Filled with a Silver Nanoshell and Liquid. OE 2019, 58 (11), 117104.

(63) Akter, S.; Ahmed, K.; El-Naggar, S. A.; Taya, S. A.; Nguyen, T. K.; Dhasarathan, V. Highly Sensitive Refractive Index Sensor for Temperature and Salinity Measurement of Seawater. Optik 2020, 216, 164901.

(64) Ahmed, K.; Haque, Md. J.; Jabin, Md. A.; Paul, B. K.; Amiri, I. S.; Yupapin, P. Tetra-Core Surface Plasmon Resonance Based Biosensor for Alcohol Sensing. Physica B: Condensed Matter 2019, 570, 48–52.

(65) Xu, H.; Song, Y.; Zhu, P.; Zhao, W.; Liu, T.; Wang, Q.; Zhao, T. Alcohol Sensor Based on Surface Plasmon Resonance of ZnO Nanoflowers/Au Structure. Materials (Basel) 2021, 15 (1), 189.

(66) Preechaburana, P.; Gonzalez, M. C.; Suska, A.; Filippini, D. Surface Plasmon Resonance Chemical Sensing on Cell Phones. Angewandte Chemie International Edition 2012, 51 (46), 11585–11588.

(67) Guner, H.; Ozgur, E.; Kokturk, G.; Celik, M.; Esen, E.; Topal, A. E.; Ayas, S.; Uludag, Y.; Elbuken, C.; Dana, A. A Smartphone Based Surface Plasmon Resonance

Imaging (SPRi) Platform for on-Site Biodetection. Sensors and Actuators B: Chemical 2017, 239, 571–577.

(68) Singh, G. P.; Sardana, N. Smartphone-Based Surface Plasmon Resonance Sensors: A Review. Plasmonics 2022, 17 (5), 1869–1888.

(69) Liu, Y.; Liu, Q.; Chen, S.; Cheng, F.; Wang, H.; Peng, W. Surface Plasmon Resonance Biosensor Based on Smart Phone Platforms. Sci Rep 2015, 5 (1), 12864.

(70) Vo-Dinh, T.; Wang, H.-N.; Scaffidi, J. Plasmonic Nanoprobes for SERS Biosensing and Bioimaging. Journal of Biophotonics 2010, 3 (1–2), 89–102.

(71) Wong, C. L.; Chen, G. C. K.; Li, X.; Ng, B. K.; Shum, P.; Chen, P.; Lin, Z.; Lin, C.; Olivo, M. Colorimetric Surface Plasmon Resonance Imaging (SPRI) Biosensor Array Based on Polarization Orientation. Biosens Bioelectron 2013, 47, 545–552.

(72) Peng, H.; Li, S.; Xing, J.; Yang, F.; Wu, A. Surface Plasmon Resonance of Au/Ag Metals for the Photoluminescence Enhancement of Lanthanide Ion Ln3+ Doped Upconversion Nanoparticles in Bioimaging. J. Mater. Chem. B 2022.

(73) Masson, J.-F. Surface Plasmon Resonance Clinical Biosensors for Medical Diagnostics. ACS Sens. 2017, 2 (1), 16–30.

(74) Parvin, T.; Ahmed, K.; Alatwi, A. M.; Rashed, A. N. Z. Differential Optical Absorption Spectroscopy-Based Refractive Index Sensor for Cancer Cell Detection. Opt Rev 2021, 28 (1), 134–143.

(75) Ahmed, K.; Paul, B. K.; Vasudevan, B.; Rashed, A. N. Z.; Maheswar, R.; Amiri, I. S.; Yupapin, P. Design of D-Shaped Elliptical Core Photonic Crystal Fiber for Blood Plasma Cell Sensing Application. Results in Physics 2019, 12, 2021–2025.

(76) Raikwar, S.; Prajapati, Y. K.; Srivastava, D. K.; Maurya, J. B.; Saini, J. P. Detection of Leptospirosis Bacteria in Rodent Urine by Surface Plasmon Resonance Sensor Using Graphene. Photonic Sens 2021, 11 (3), 305–313.

(77) Omar, N. A. S.; Fen, Y. W.; Abdullah, J.; Zaid, M. H. M.; Daniyal, W. M. E. M. M.; Mahdi, M. A. Sensitive Surface Plasmon Resonance Performance of Cadmium Sulfide Quantum Dots-Amine Functionalized Graphene Oxide Based Thin Film towards Dengue Virus E-Protein. Optics & Laser Technology 2019, 114, 204–208.

(78) Bong, J.-H.; Kim, T.-H.; Jung, J.; Lee, S. J.; Sung, J. S.; Lee, C. K.; Kang, M.-J.; Kim, H. O.; Pyun, J.-C. Pig Sera-Derived Anti-SARS-CoV-2 Antibodies in Surface Plasmon Resonance Biosensors. BioChip J 2020, 14 (4), 358–368.

(79) Funari, R.; Chu, K.-Y.; Shen, A. Q. Detection of Antibodies against SARS-CoV-2 Spike Protein by Gold Nanospikes in an Opto-Microfluidic Chip. Biosensors and Bioelectronics 2020, 169, 112578.

(80) Liu, M.; Zheng, C.; Cui, M.; Zhang, X.; Yang, D.-P.; Wang, X.; Cui, D. Graphene Oxide Wrapped with Gold Nanorods as a Tag in a SERS Based Immunoassay for the Hepatitis B Surface Antigen. Microchim Acta 2018, 185 (10), 458.

(81) Shin, W.-R.; Sekhon, S. S.; Rhee, S.-K.; Ko, J. H.; Ahn, J.-Y.; Min, J.; Kim, Y.-H. Aptamer-Based Paper Strip Sensor for Detecting Vibrio Fischeri. ACS Comb. Sci. 2018, 20 (5), 261–268.

(82) Mudgal, N.; Yupapin, P.; Ali, J.; Singh, G. BaTiO3-Graphene-Affinity Layer–Based Surface Plasmon Resonance (SPR) Biosensor for Pseudomonas Bacterial Detection. Plasmonics 2020, 15 (5), 1221–1229.

(83) Rippa, M.; Castagna, R.; Brandi, S.; Fusco, G.; Monini, M.; Chen, D.; Zhou, J.; Zyss, J.; Petti, L. Octupolar Plasmonic Nanosensor Based on Ordered Arrays of Triangular Au Nanopillars for Selective Rotavirus Detection. ACS Appl. Nano Mater. 2020, 3 (5), 4837–4844.

(84) Chuang, C.-S.; Wu, C.-Y.; Juan, P.-H.; Hou, N.-C.; Fan, Y.-J.; Wei, P.-K.; Sheen, H.-J. LMP1 Gene Detection Using a Capped Gold Nanowire Array Surface Plasmon Resonance Sensor in a Microfluidic Chip. Analyst 2020, 145 (1), 52–60.

(85) Kaushik, S.; Tiwari, U. K.; Pal, S. S.; Sinha, R. K. Rapid Detection of Escherichia Coli Using Fiber Optic Surface Plasmon Resonance Immunosensor Based on Biofunctionalized Molybdenum Disulfide (MoS2) Nanosheets. Biosensors and Bioelectronics 2019, 126, 501–509.

(86) Kim, J.-W.; Kim, M.; Lee, K. K.; Chung, K. H.; Lee, C.-S. Effects of Graphene Oxide-Gold Nanoparticles Nanocomposite on Highly Sensitive Foot-and-Mouth Disease Virus Detection. Nanomaterials 2020, 10 (10), 1921.

(87) Park, J.-H.; Cho, Y.-W.; Kim, T.-H. Recent Advances in Surface Plasmon Resonance Sensors for Sensitive Optical Detection of Pathogens. Biosensors (Basel) 2022, 12 (3), 180.

(88) Bellassai, N.; D’Agata, R.; Jungbluth, V.; Spoto, G. Surface Plasmon Resonance for Biomarker Detection: Advances in Non-Invasive Cancer Diagnosis. Frontiers in Chemistry 2019, 7.

(89) Avci, E.; Yilmaz, H.; Sahiner, N.; Tuna, B. G.; Cicekdal, M. B.; Eser, M.; Basak, K.; Altıntoprak, F.; Zengin, I.; Dogan, S.; Çulha, M. Label-Free Surface Enhanced Raman Spectroscopy for Cancer Detection. Cancers 2022, 14 (20), 5021.

(90) Aćimović, S. S.; Ortega, M. A.; Sanz, V.; Berthelot, J.; Garcia-Cordero, J. L.; Renger, J.; Maerkl, S. J.; Kreuzer, M. P.; Quidant, R. LSPR Chip for Parallel, Rapid, and Sensitive Detection of Cancer Markers in Serum. Nano Lett 2014, 14 (5), 2636–2641.

(91) Mahani, M.; Alimohamadi, F.; Torkzadeh-Mahani, M.; Hassani, Z.; Khakbaz, F.; Divsar, F.; Yoosefian, M. LSPR Biosensing for the Early-Stage Prostate Cancer Detection Using Hydrogen Bonds between PSA and Antibody: Molecular Dynamic and Experimental Study. Journal of Molecular Liquids 2021, 324, 114736.

(92) Asl, M. B.; Karamdel, J.; Khoshbaten, M.; Rostami, A. Plasmonic Biosensor for Early Gastric Cancer Detection. Opt. Continuum, OPTCON 2022, 1 (9), 2043–2061.

(93) Lyu, S.; Wu, Z.; Shi, X.; Wu, Q. Optical Fiber Biosensors for Protein Detection: A Review. Photonics 2022, 9 (12), 987.

(94) Li, Y.; Liu, X.; Lin, Z. Recent Developments and Applications of Surface Plasmon Resonance Biosensors for the Detection of Mycotoxins in Foodstuffs. Food Chemistry 2012, 132, 1549–1554.

(95) Fleischmann, M.; Hendra, P. J.; McQuillan, A. J. Raman Spectra of Pyridine Adsorbed at a Silver Electrode. Chemical Physics Letters 1974, 26 (2), 163–166.

(96) Jeanmaire, D. L.; Van Duyne, R. P. Surface Raman Spectroelectrochemistry: Part I. Heterocyclic, Aromatic, and Aliphatic Amines Adsorbed on the Anodized Silver Electrode. Journal of Electroanalytical Chemistry and Interfacial Electrochemistry 1977, 84 (1), 1–20.

(97) Albrecht, M. G.; Creighton, J. A. Anomalously Intense Raman Spectra of Pyridine at a Silver Electrode. J. Am. Chem. Soc. 1977, 99 (15), 5215–5217.

(98) Kurouski, D.; Large, N.; Chiang, N.; Henry, A.-I.; Seideman, T.; Schatz, G. C.; Van Duyne, R. P. Unraveling the Near- and Far-Field Relationship of 2D Surface-Enhanced Raman Spectroscopy Substrates Using Wavelength-Scan Surface-Enhanced Raman Excitation Spectroscopy. J. Phys. Chem. C 2017, 121 (27), 14737–14744.

(99) Driscoll, A. J.; Harpster, M. H.; Johnson, P. A. The Development of Surface-Enhanced Raman Scattering as a Detection Modality for Portable in Vitro Diagnostics: Progress and Challenges. Phys. Chem. Chem. Phys. 2013, 15 (47), 20415.

(100) Jensen, L.; Aikens, C. M.; Schatz, G. C. Electronic Structure Methods for Studying Surface-Enhanced Raman Scattering. Chem. Soc. Rev. 2008, 37 (5), 1061.

(101) Heeg, S.; Mueller, N. S.; Wasserroth, S.; Kusch, P.; Reich, S. Experimental Tests of Surface-Enhanced Raman Scattering: Moving beyond the Electromagnetic Enhancement Theory. Journal of Raman Spectroscopy 2021, 52 (2), 310–322.

(102) Kneipp, K.; Wang, Y.; Kneipp, H.; Perelman, L. T.; Itzkan, I.; Dasari, R. R.; Feld, M. S. Single Molecule Detection Using Surface-Enhanced Raman Scattering (SERS). Phys. Rev. Lett. 1997, 78 (9), 1667–1670.

(103) Nie, S.; Emory, S. R. Probing Single Molecules and Single Nanoparticles by Surface-Enhanced Raman Scattering. Science 1997, 275 (5303), 1102–1106.

(104) Adrian, F. J. Charge Transfer Effects in Surface-enhanced Raman Scattering a). The Journal of Chemical Physics 1982, 77 (11), 5302–5314.

(105) Lippitsch, M. E. Ground-State Charge Transfer as a Mechanism for Surface-Enhanced Raman Scattering. Phys. Rev. B 1984, 29 (6), 3101–3110.

(106) Ling, X.; Moura, L. G.; Pimenta, M. A.; Zhang, J. Charge-Transfer Mechanism in Graphene-Enhanced Raman Scattering. J. Phys. Chem. C 2012, 116 (47), 25112–25118.

(107) Xia, M. 2D Materials-Coated Plasmonic Structures for SERS Applications. Coatings 2018, 8 (4), 137.

(108) Guo, L.; Mao, Z.; Jin, S.; Zhu, L.; Zhao, J.; Zhao, B.; Jung, Y. M. A SERS Study of Charge Transfer Process in Au Nanorod–MBA@Cu2O Assemblies: Effect of Length to Diameter Ratio of Au Nanorods. Nanomaterials 2021, 11 (4), 867.

(109) Sharma, B.; Frontiera, R. R.; Henry, A.-I.; Ringe, E.; Van Duyne, R. P. SERS: Materials, Applications, and the Future. Materials Today 2012, 15 (1), 16–25.

(110) Meyer, S. A.; Ru, E. C. L.; Etchegoin, P. G. Quantifying Resonant Raman Cross Sections with SERS. J. Phys. Chem. A 2010, 114 (17), 5515–5519.

(111) Isabel Pérez-Jiménez, A.; Lyu, D.; Lu, Z.; Liu, G.; Ren, B. Surface-Enhanced Raman Spectroscopy: Benefits, Trade-Offs and Future Developments. Chemical Science 2020, 11 (18), 4563–4577.

(112) Duque, T.; Chaves Ribeiro, A. C.; de Camargo, H. S.; Costa Filho, P. A. da; Mesquita Cavalcante, H. P.; Lopes, D. New Insights on Optical Biosensors: Techniques, Construction and Application. In State of the Art in Biosensors - General Aspects; Rinken, T., Ed.; InTech, 2013.

(113) Kim, K.; Choi, N.; Jeon, J. H.; Rhie, G.; Choo, J. SERS-Based Immunoassays for the Detection of Botulinum Toxins A and B Using Magnetic Beads. Sensors 2019, 19 (19), 4081.

(114) Krafft, C.; Popp, J. Raman-Based Technologies for Biomedical Diagnostics. In Comprehensive Biomedical Physics; Elsevier, 2014; pp 189–208.

(115) Lopez, A.; Lovato, F.; Hwan Oh, S.; Lai, Y. H.; Filbrun, S.; Driskell, E. A.; Driskell, J. D. SERS Immunoassay Based on the Capture and Concentration of Antigen-Assembled Gold Nanoparticles. Talanta 2016, 146, 388–393.

(116) Granger, J. H.; Granger, M. C.; Firpo, M. A.; Mulvihill, S. J.; Porter, M. D. Toward Development of a Surface-Enhanced Raman Scattering (SERS)-Based Cancer Diagnostic Immunoassay Panel. Analyst 2013, 138 (2), 410–416.

(117) Wang, G.; Lipert, R. J.; Jain, M.; Kaur, S.; Chakraboty, S.; Torres, M. P.; Batra, S. K.; Brand, R. E.; Porter, M. D. Detection of the Potential Pancreatic Cancer Marker MUC4 in Serum Using Surface-Enhanced Raman Scattering. Anal. Chem. 2011, 83 (7), 2554–2561.

(118) Wang, Z.; Zong, S.; Wu, L.; Zhu, D.; Cui, Y. SERS-Activated Platforms for Immunoassay: Probes, Encoding Methods, and Applications. Chem. Rev. 2017, 117 (12), 7910–7963.

(119) Xue, Y.; Li, X.; Li, H.; Zhang, W. Quantifying Thiol–Gold Interactions towards the Efficient Strength Control. Nat Commun 2014, 5 (1), 4348.

(120) Wang, C.; Yan, Q.; Liu, H.-B.; Zhou, X.-H.; Xiao, S.-J. Different EDC/NHS Activation Mechanisms between PAA and PMAA Brushes and the Following Amidation Reactions. Langmuir 2011, 27 (19), 12058–12068.

(121) Pilot, R.; Signorini, R.; Durante, C.; Orian, L.; Bhamidipati, M.; Fabris, L. A Review on Surface-Enhanced Raman Scattering. Biosensors (Basel) 2019, 9 (2).

(122) Pollap, A.; Świt, P. Recent Advances in Sandwich SERS Immunosensors for Cancer Detection. Int J Mol Sci 2022, 23 (9), 4740.

(123) D. Porter, M.; J. Lipert, R.; M. Siperko, L.; Wang, G.; Narayanan, R. SERS as a Bioassay Platform: Fundamentals, Design, and Applications. Chemical Society Reviews 2008, 37 (5), 1001–1011.

(124) Xu, S.; Ji, X.; Xu, W.; Li, X.; Wang, L.; Bai, Y.; Zhao, B.; Ozaki, Y. Immunoassay Using Probe-Labelling Immunogold Nanoparticles with Silver Staining Enhancement via Surface-Enhanced Raman Scattering. Analyst 2004, 129 (1), 63.

(125) Guo, M.; Dong, J.; Xie, W.; Tao, L.; Lu, W.; Wang, Y.; Qian, W. SERS Tags-Based Novel Monodispersed Hollow Gold Nanospheres for Highly Sensitive Immunoassay of CEA. J Mater Sci 2015, 50 (9), 3329–3336.

(126) Zengin, A.; Tamer, U.; Caykara, T. A SERS-Based Sandwich Assay for Ultrasensitive and Selective Detection of Alzheimer’s Tau Protein. Biomacromolecules 2013, 14 (9), 3001–3009.

(127) Femtomolar Detection of Prostate-Specific Antigen: An Immunoassay Based on Surface-Enhanced Raman Scattering and Immunogold Labels | Analytical Chemistry. (accessed 2021-10-10).

(128) Camacho, S. A.; Sobral-Filho, R. G.; Aoki, P. H. B.; Constantino, C. J. L.; Brolo, A. G. Zika Immunoassay Based on Surface-Enhanced Raman Scattering Nanoprobes. ACS Sens. 2018, 3 (3), 587–594.

(129) Petryayeva, E.; Krull, U. J. Localized Surface Plasmon Resonance: Nanostructures, Bioassays and Biosensing—A Review. Analytica Chimica Acta 2011, 706 (1), 8–24.

(130) Kosuda, K. M.; Bingham, J. M.; Wustholz, K. L.; Van Duyne, R. P.; Groarke, R. J. Nanostructures and Surface-Enhanced Raman Spectroscopy. In Comprehensive Nanoscience and Nanotechnology; Elsevier, 2016; pp 117–152.

(131) Singh, P. LSPR Biosensing: Recent Advances and Approaches. In Reviews in Plasmonics 2016; Geddes, C. D., Ed.; Reviews in Plasmonics; Springer International Publishing: Cham, 2017; pp 211–238.

(132) Jackman, J. A.; Ferhan, A. R.; Cho, N.-J. Surface-Based Nanoplasmonic Sensors for Biointerfacial Science Applications. BCSJ 2019, 92 (8), 1404–1412.

(133) Shen, M.; Wang, M.; Zhou, J.; Du, L.; Deng, C. Nanostructured Plasmonic Interferometers for Compact Sensing. Plasmonics 2017, 12 (3), 691–697.

(134) Ringe, E.; Zhang, J.; Langille, M. R.; Sohn, K.; Cobley, C.; Au, L.; Xia, Y.; Mirkin, C. A.; Huang, J.; Marks, L. D.; Van Duyne, R. P. Effect of Size, Shape, Composition, and Support Film on Localized Surface Plasmon Resonance Frequency: A Single Particle Approach Applied to Silver Bipyramids and Gold and Silver Nanocubes. MRS Proc. 2009, 1208, 1208-O10-02.

(135) Gao, M.; Zheng, X.; Khan, I.; Cai, H.; Lan, J.; Liu, J.; Wang, J.; Wu, J.; Huang, S.; Li, S.; Kang, J. Resonant Light Absorption and Plasmon Tunability of Lateral Triangular Au Nanoprisms Array. Physics Letters A 2019, 383 (31), 125881.

(136) Hegde, H. R.; Chidangil, S.; Sinha, R. K. Refractive Index Sensitivity of Au Nanostructures in Solution and on the Substrate. J Mater Sci: Mater Electron 2022, 33 (7), 4011–4024.

(137) Jeon, H. B.; Tsalu, P. V.; Ha, J. W. Shape Effect on the Refractive Index Sensitivity at Localized Surface Plasmon Resonance Inflection Points of Single Gold Nanocubes with Vertices. Sci Rep 2019, 9 (1), 13635.

(138) Fan, M.; Thompson, M.; Andrade, M. L.; Brolo, A. G. Silver Nanoparticles on a Plastic Platform for Localized Surface Plasmon Resonance Biosensing. Anal. Chem. 2010, 82 (15), 6350–6352.

Chapter 3: Exploring Intensity Distributions and Sampling in SERS-Based Immunoassays

This chapter is based on the published work: Ariadne Tuckmantel Bido, Arash Azarakhshi, and Alexandre G. Brolo, Exploring Intensity Distributions and Sampling in SERS-Based Immunoassays. Analytical Chemistry 2022 94 (49), 17031-17038. Copyright: Reproduced with permission.

ATB performed all the experiments, developed the codes for the data analysis, analyzed the data and wrote the first draft of the manuscript. Arash Azarakhshi programmed the %RMSE and chi-square calculations.

Surface-enhanced Raman scattering (SERS) is a sensitive, widely used spectroscopic technique. However, SERS is perceived as poorly reproducible and insufficiently robust for standard applications in analytical chemistry. Here we demonstrated that reliable SERS immunoassay quantification at low concentrations (pM range) can be achieved by careful experimental design and appropriate data analysis statistics. A SERS-based immunoassay for IgG in human serum (3.1 to 50.0 ng.mL^{-1} or 20.6 to 333 pM) was developed as a proof-of-concept. Calibration curves were created using the population median of the band area, centred at 592 cm^{-1}, of a SERS reporter (Nile Blue A). Histograms of seventy-two thousand SERS spectra show lognormal distributions. Scanning electron microscope (SEM) images of the sensor platform confirm a correlation between the number of SERS probes (ERLs) at the surface and the SERS intensity response. The IgG immunosensor reported here presented a LOD of 1.11 ng.mL^{-1} or 7.39 pM and LOQ of 9.04 ng.mL^{-1} or 60.30 pM, within a 95% confidence level. The % error of the predicted versus the actual response of a quality control (QC) sample was 0.13%. The percent error of the QC sample decreases exponentially with the number of measurements. Randomly selected spatially separated measurements provided lower QC % error than a larger number of measurements that were closely spaced. We propose that it is necessary to describe the measured populations using an appropriate sample size for good statistics and consider the interrogation of sufficiently large and well-separated areas of the sensor surface to achieve a reliable sampling.

3.1 Introduction

Surface-enhanced Raman scattering (SERS) is broadly explored for biomedical research in a variety of areas, such as diagnosis, bio-imaging, bio-molecule analysis, single-cell and pathogenic bacteria detection.[1,2] A wide variety of SERS substrates have been developed and used for specific analytes and biomedical methods.[3–5] SERS-based sensors have a small footprint, enable multiplexing and their high sensitivity permits single-particle, single organism and single-molecule detection[6,7]. These characteristics make them ideal for incorporation into microfluidics devices.[8–10]

SERS-based immunoassay is among the most explored biomedical application of SERS. SERS immunoassays of different formats have been developed in many labs and their sensitivity rival the state-of-the-art ELISA method.[11–16] Although SERS immunoassays are now well-established, there are still aspects that must be considered to make it competitive to the widely used fluorescence-based methods in ELISA. Large fluctuations in intensities caused by heterogeneously distributed electromagnetic hotspots in the sensing area are inherent to the SERS technique. There are substantial local optical field variations within nanometers that are predicted by theory and observed in experiments.[12] These fluctuations can affect the reliability and reproducibility of the SERS readout, particularly at low concentrations (pM and lower). A considerable effort has been devoted to obtain reliable assay quantification, but those were mostly focused on the optimization of the SERS substrate or the quality of the SERS probe reporters.[6,12,17,18]

SERS immunoassays at low concentrations require the evaluation of signal from a surface containing a small number of nanoparticle probes that support the enhancement effect. Those probes are known in the literature as extrinsic Raman labels (ERLs).[19] As the number of probes present in the sensing surface decreases, the minor dissimilarities and clustering result in a considerable effect on the magnitude of the SERS intensity response that may directly interfere with the reproducibility and reliability of the assay.[20] Typically, a few spectra from different regions of the sensing surface are obtained and their intensities are averaged and symmetric error bars are reported. This assume that the SERS intensity from different regions of the sensing surface follows a Gaussian (normal) distribution,[21] which could not be the case at low concentrations. In fact, the sparse distribution of ERLs along the sensing surface in comparison to the area probed by the laser in a single spot constitute a classical analytical chemistry sampling issue.[6] Some groups have attempted to tackle this problem by increasing the probing area by either using the Raman mapping or the Raman global imaging technique.[22,23] There is a trade-off between the number of spectra taken and the variation in the assessed relative standard deviation (RSD) of the areas (intensities) of SERS signals. A decrease in RSD from 20% to 5% when increasing the number of spectra from 180 to 2040 was reported for SERS measurements of rhodamine 6G in thin films.[24]

Here we examined the spatial distribution of SERS intensities for immunoassays at low analyte concentrations using a relatively large dataset. The goal is to verify the effect of the SERS intensity variations, their distribution and the sampling conditions in the accuracy of the assay. As a proof of concept, a SERS immunoassay for IgG in human serum detection was developed and the accuracy in the determination of a quality control sample was evaluated. The sensing surface consisted of a gold-covered glass slide coated with protein A which was used as a mediator to anchor the anti-human IgG Fc specific antibody. Various concentrations of IgG from human serum were added to the sensing surface, while IgM from human serum was used as control. Next, the ERLs containing the Raman reporter Nile Blue A and anti-human IgG Fc specific were added to the substrates. The ERLs present in the sensing surface correlated with the amount of adsorbed IgG. A large SERS dataset was obtained for each IgG concentration through Raman mapping of randomly chosen regions of the sensing surface. The distribution of SERS intensities for the tested concentrations of IgG in this assay were all lognormal rather than Gaussian.

3.2 Materials and Methods

3.2.1 Materials

Glass slides (1″ x 1″ x 0.040″) coated with Cr 50 Å and Au 100 nm were acquired from Evaporated Metal Films (EMF Dynasil). PBS pH 7.2 (1X) was purchased from Gibco. Sodium azide, Protein A from Staphylococcus aureus and Dimethyl sulfoxide (DMSO) HPLS grade were purchased from Sigma-Aldrich. IgG and IgM from human serum were purchased from Sigma. Anti-Human IgG (Fab specific) antibody produced in goat and Anti-Human IgG (Fc specific) antibody produced in rabbit was purchased from Millipore Sigma. Nile Blue A perchlorate (NB) and chloroauric acid ($HAuCl_4 \cdot 3H_2O$) were purchased from Aldrich. Sodium citrate salt dihydrate, and polyoxyethylene-20 (tween 20) were purchased from Biotech. Dithiobis-succinimide propionate (DSP) was purchased from Thermo Scientific. Ethyl alcohol anhydrous was purchased from Commercial Alcohols. The Sylgard 184 silicone elastomer kit was purchased from Dow Corning Corporation. All aqueous solutions were prepared with ultrapure water obtained from a Nanopure Diamond™, 18.2 MΩ.cm at 25 °C. Centrifugation was conducted using an accuSpin Micro 17 from Fisher Scientific.

3.2.2 Synthesis of Gold Nanoparticles (AuNPs)

Colloidal gold nanoparticles (AuNPs) were fabricated by reducing chloroauric acid ($HAuCl_4 \cdot 3H_2O$) with citrate as described elsewhere, with minor changes.[25] In a 150 mL beaker, 99 mL of ultrapure water was brought to boil, covered with a watch glass. Next, 1 mL of a 1% m/v $HAuCl_4 \cdot 3H_2O$ solution was added at 800 rpm stirring. After one minute, 1 mL of a 1% m/v trisodium citrate solution was added at once and left boiling covered with the watch glass for 5 minutes. Finally, 1 mL of a 5% m/v sodium azide solution was added dropwise, and the heat was turned off. The colloid was left stirring until it reached room temperature (around 45 minutes) and was stored in a glass vial at 4 °C. This synthesis yields a 31 ± 4 nm particle with approximately 2×10^{10} AuNPs/mL.

3.2.3 Preparation of the extrinsic Raman labels (ERLs)

Briefly, 300 µL of a 5 µM freshly prepared NB solution in water is added dropwise to 2 mL of the AuNPs at 1000 rpm stirring. After 20 minutes, 230 µL aliquots were separated into small glass vials. To each aliquot, it was added dropwise 100 µL of a 10 µg.mL^{-1} antibody solution (i5260-anti-human IgG Fc specific), made from a 20 µg.mL^{-1} stock in PBS 10 times diluted in ultrapure water (PBS-10). This dilution of the PBS was done to prevent nanoparticle aggregation that happened with the high salt content. The solution in the vials was left stirring for 30 min. Then, 8 µL of a 5% BSA solution in PBS-10 was added to each vial and left stirring for 20 minutes. The aliquots were centrifuged for 20 min at 7000 g, then resuspended in 200 µL of PBS-10.

As noted from the description above, the ERLs were prepared by adsorption of the Raman reporter (NB) to the AuNPs, followed by the adsorption of the antibody anti-human IgG Fc specific, via electrostatic interactions with the capping agent on the AuNPs. Azide-functionalized gold nanoparticles are used for click-chemistry with alkynes.[26,27] The azide promotes NB adsorption with higher efficiency than the same citrate-reduced colloid without the azide addition. Nile Blue A perchlorate is a cationic oxazine dye that has properties of both the donor and electron acceptor.[28] Azide can act as a hydrogen bond acceptor,[29] and we suggest that it interacts with the amine portions of the dye, forming a hydrogen bond that increases the NB coverage onto the gold nanoparticle. Next, the antibody associates with the AuNPs through noncovalent forces such as hydrogen bonding, van der Waals and hydrophobic interactions related to protein structure and surface charge.[30] The ERLs contain approximately 100 antibodies per gold nanoparticle. The number of antibodies per gold nanoparticle was calculated based on the amount of antibodies added to the gold nanoparticles.

To investigate if the binding capacity of the ERLs is adequate, a lateral flow assay (LFA)[31] was conducted (see Appendix A - Figure A-S1). The results from the LFA confirmed that the ERLs had a high affinity to the antigen with no significant cross reactivity with the IgM referenced as negative control. The LFA results suggest that the distribution of orientations of the antibodies adsorbed on the ERLs allow sufficient exposure of the Fab specific regions to interact with the antigen IgG from human serum. Other control experiments confirmed that the adsorption of the antibody does not decrease the Raman signal from NB. Therefore, there is no evidence of displacement of the NB after the antibody is attached to the probe.

3.2.4 PDMS Fabrication

A silicon wafer was used as a base to prepare poly(dimethylsiloxane) (PDMS) masks to define the sensing surface on the gold-coated glass slide. A 10:1 mixture of a silicone elastomer base and an elastomer curing agent were poured into a silicon wafer. After degassing in a desiccator under vacuum, the PDMS was baked at 150 °C for 1 h to polymerize. The PDMS was then peeled and cut into the same size as the gold-covered slides, and holes with 5 mm-diameter holes were made to superpose the marked regions in the slides. A schematic of the assembly is presented in Appendix A (Figure A-S2). The PDMS masks were washed with water and soap, then rinsed with ethanol and N_2 dried.

3.2.5 Sensor Surface Modification and SERS-based Immunoassay

A schematic of the assembled platform used in this work is presented in Figure A-S2 of Appendix A. The gold-covered slides were first marked with an electric pen to determine regions to be modified and to define the regions for Raman and scanning electron microscopy (SEM) measurements. The slides were cleaned with piranha solution for 10 min, washed abundantly with ultrapure water and N_2 dried. The PDMS mask was added on top of the slides. The holes were superposed with the marked regions. The slide and the mask were then sandwiched in a 3D-printed platform (Figure A-S2) and clamped together with a binder clip. To each region of exposed Au, a 50 μL of a 0.002M dithiobis-succinimide propionate (DSP) solution in dimethylsulfoxide (DMSO) was added for 2 hours. Each well was washed 4x with 50 μL of ultrapure water, followed by the addition of 20 μL of a 1 mg.mL^{-1} protein A in PBS-10. All the platforms were then put inside of a humidity chamber and left at 4 °C overnight. Each well was washed with PBS-10 3X, 50 μL/ well followed by the addition of 30 μL of a 1 mg.mL^{-1} anti-human IgG Fc specific produced in rabbit, whole antiserum and left 4 °C overnight. The wells were washed with PBS-10 3X, 50 μL/ well.

3.2.6 Instrumentation

AuNPs and ERLs (AuNPs/NB/antibody) were characterized by dynamic light scattering (DLS), ζ-potential, ultraviolet-visible (UV-Vis) and transmission electron microscopy (TEM). Anton Paar LiteSizer 500 was used to measure the hydrodynamic radius (DLS) and surface charge (ζ-potential). The size and shape of the particles were estimated from UV-Vis spectroscopy measured using a Biotek Cytation 5 (Agilent) plate reader. TEM images were taken using a JEOL 1011 Transmission Electron Microscope. SEM images of the sensor surfaces after the assays described in Figure 3-1E were taken by Hitachi S-4800 scanning electron microscope at 1kV. Raman measurements were recorded on a Renishaw inVia Raman Microscope. The excitation laser was at 633 nm (He–Ne), and a 50 X Leica Germany 5660 objective (NA=0.75) was used. SERS maps were recorded in 30 by 30 μm^2 regions, with 1 μM step size, using a Renishaw MS 20 Encoded stage 100 nm. Each SERS map consisted of 900 spectra taken using the StreamLine™ image acquisition, 10 seconds integration time, 10 mW laser power, grating 1200 l/mm, and the Renishaw CCD camera. StreamLine™ uses a laser line rather than a laser spot to illuminate the surface to be mapped. Each imaged point of the sample transverses the laser line once with a synchronized stage motion with the movement of signal on the detector. The detector accumulates the signal and then reads it, generating an image. The area of the spread beam is around 0.22 mm^2 and the power density is around 45.5 mW/mm^2. The same assay was done conventionally, using a laser spot to raster the surface, with 3 seconds integration time without StreamLine™ maintaining all the other parameters and the results are comparable. The time required to record a SERS map was reduced from 55 minutes with a laser spot rastering to 6.5 minutes with StreamLine™. The rapid measurement of the samples permits an extensive data collection, improving the accuracy of the sensor. Each pixel size was about 1.1 μm^2 for both mapping modalities.

3.3 Result and Discussion

3.3.1 Overview of the Immunoassay

Figure 3-1 shows a general scheme for the chemical modification procedures of the sensing surface and the main concept of the immunoassay. The sensor surface modification was based on a procedure reported in the literature with a few modifications (Figure 3-1A - D).[32,33] Oriented antibody immobilization is achieved using protein A as a facilitator. Protein A has a region that specifically recognizes and binds to the Fc domain of some mammalian IgG subclasses, such as human, rabbit, pig, and monkey. This antibody immobilization leaves the Fab region of the antibody well accessible for interaction with the antigen.[34,35]

Protein A also has a cysteine-rich region opposite to the Fc binding domain region containing thiol groups. The cysteine-rich region contains thiol groups that have high affinity to gold and can be linked directly to it through chemisorption. DSP (Figure 3-1A) is a homo-bifunctional cross-linker containing a disulphide bridge that covalently attaches to the gold substrate via a thiol bond, forming a self-assembled monolayer (SAM). The ester moiety of the DSP reacts with the amine functionality on proteins forming stable amide bonds.[32] The amine groups of the cysteine residues in protein A reacts with DSP and this interaction anchors the protein onto the sensing surface (Figure 3-1B). Figure 3-1D shows that the immobilized protein A can then interact with the antibody (Figure 3-1C) forming an IgG-capturing layer on the sensing platform.

Figure 3-1E shows a scheme for the SERS immunoassay. In the modified areas of the sensor surface, 30 μL of the desired antigen concentration, IgG from human serum, was added. Duplicates of seven IgG concentrations were used, ranging from 3.1 to 50.0 ng.mL^{-1}. Duplicate of two controls, IgM from human serum at 25 ng.mL^{-1} and only PBS-10 were also run. The platforms were put inside of a humidity chamber for 3 hours and then washed with PBST-10 (0.1% tween 20 in PBS-10) 3X, 50 μL/ well, followed by PBS-10 2X, 50 μL/ well. Lastly, 30 μL of the freshly prepared ERLs were added to each well for incubation inside of a humidity chamber for 30 minutes, resulting in the sandwiched architecture presented in Figure 3-1E. The PDMS mask was then removed, and the whole sensor surface was washed abundantly with ultrapure water using a wash bottle and N_2 dried. The sensor slides were left in a slide box, protected from light, and the marked regions were then eventually interrogated using a Raman Microscope. The sensors were evaluated several times, showing no evidence of degradation during an 8-months period. SEM images of the sensor areas were also obtained.

A second assay was conducted in the same manner, but with higher concentrations of IgG, ranging from 12.5 to 200.0 ng.mL^{-1}, and a control, IgM at 25.0 ng.mL^{-1}. The calibration curve is on Appendix A, Figure A-S3. After 100.0 ng.mL^{-1} the sensor is not quantitative anymore and the signal plateaus. Although reliable quantification was not possible, the SERS-based sensor is still useful as a screening tool in the high concentration range.

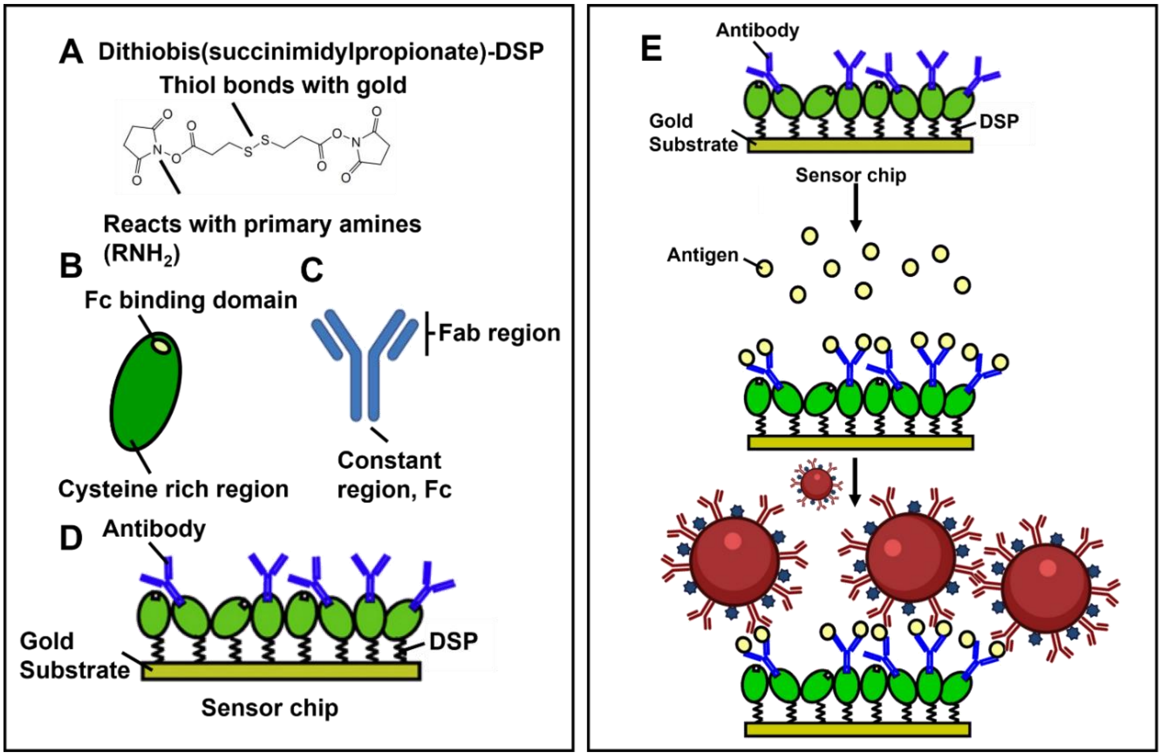

Figure 3-1. A) DSP structure. B) Scheme of the two protein A regions being a cysteine-rich that reacts with DSP and a Fc binding domain, that anchors the antibody to the sensor. C) Representation of the Fab and Fc regions in an antibody. D) Representation of the sensor chip after modification with DSP, protein A and the antibody. E) Scheme of the sensor steps for antigen binding and Raman reporter interaction, resulting in the finalized assay.

3.3.2 ERLs Characterization

Figure 3-2 shows the data for the AuNPs characterization before and after NB and antibody adsorption to the surface. The UV-Vis maximum absorbance in Figure 3-2A is due to the excitation of localized surface plasmon resonances (LSPR band). A redshift of the LSPR peak from 517.4 ± 0.1 to 523.2 ± 0.1 is evident in Figure 3-2A, suggesting that the antibodies have replaced the citrate. The LSPR redshift is caused by a change in the dielectric constant of the environment around the AuNPs due to the antibody adsorption.[30] Similarly, in Figure 3-2B, the dynamic light scattering (DLS) results show an increase in hydrodynamic diameter due to the adsorption of the protein on the AuNPs.[36] Figure 3-2C shows the ζ- potential of the AuNPs and ERLs. TEM images of AuNPs before and after IgG adsorption to the particles (ERL) are shown in Figure 3-2A. Only the AuNPs core are evident in the TEM due to the high density of the gold and the presence of the adsorbed protein cannot be inferred by TEM. The TEM images were analyzed using Image J software to determine the AuNPs size. The diameters of 2065 AuNPs were measured, and an average value of 31 ± 4 nm was determined. Table 3-1 summarizes the averages of triplicate DLS, ζ- potential and UV-Vis measurements for both AuNP and ERLs.

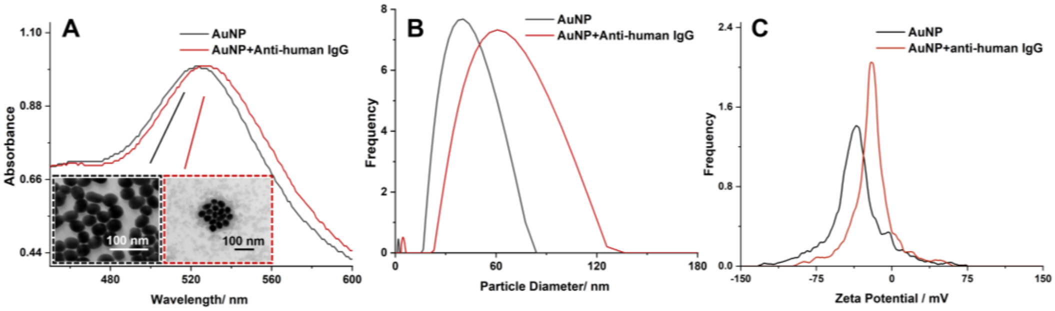

Figure 3-2. A) Normalized UV-Vis and TEM images, B) Dynamic light scattering (DLS) and C) ζ- potential for the gold nanoparticles and the gold nanoparticles with anti-human IgG adsorbed on the surface (ERLs).

Table 3-1. DLS triplicates and ζ- potential duplicates for AuNP and ERLs (AuNP/NB/Ab).

Nanoparticle	Hydrodynamic diameter / nm	Zeta Potential / mV	UV-Vis peak wavelength
AuNP	36.8 ± 0.4	-37.6 ± 1.4	517.4 ± 0.1
AuNP/NB/anti-human IgG	53.9 ± 0.5	-18.1 ± 0.9	523.2 ± 0.1

3.3.3 SERS Mapping and Intensity Distribution

Typical Raman mappings obtained for different concentrations of antigens are presented in Figure 3-3A. The advantage of using NB as a Raman reporter for the ERLs is that it is a chromophore with a large Raman cross-section. Additionally, the excitation laser line at 632.8 nm overlaps with the absorption spectrum of NB, centred at 630 nm, resulting in a resonance Raman (RR) condition. Therefore, the Raman spectra contains a double enhancement contribution (SERS and RR, also known as surface-enhanced resonance Raman scattering - SERRS) providing the very strong Raman signature required for the detection of single particles in this assay.[7,37] Each spectrum in a Raman mapping was individually baseline corrected using the Savitsky-Golay signal removal method, described elsewhere (Figure A-S4 of Appendix A).[38] The area under the NB phenoxazine ring mode, centered at 592 cm^{-1}, was identified using the Peakfit function in the MATLAB® software followed by integration. Peakfit was applied to cover a range of 15 wavenumbers in each side of the centered peak, with Lorentzian peak shape and 20 iterations to fit until the fitting error was minimized. Hence, the color scale in Figure 3-3A indicates the area under the NB SERS peak (dubbed in this work as "SERS intensity") at different positions on the sensor surface. Eight 900 μm^2 random regions of the 7.1 mm^2 sensor surface were mapped, and duplicate measurements were performed in at least four of them. In total, 7200 spectra were recorded for each sensor surface totaling sixty-four thousand measurements (7200 for sample, and 9 sensor surfaces at different concentrations of the analyte plus the controls). Figure 3-3B shows representative distributions of SERS intensities with a lognormal fitting (NB SERS Intensities) produced from the SERS maps (Figure 3-3A) obtained at different concentrations. SEM images were also obtained for all sensing surfaces containing the ERLs for the different concentrations investigated. Representative SEM images are shown in Figure 3-3C, for three concentrations of IgG.

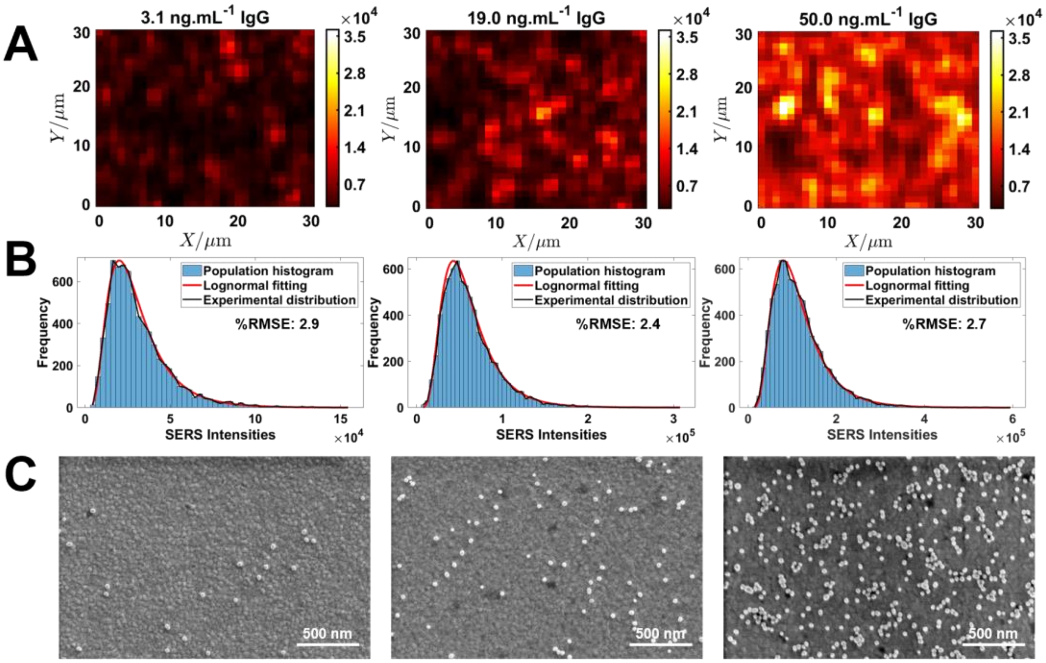

Figure 3-3. A) Color Maps of Intensity of Raman measurements for selected concentrations (3.1, 19.0 and 50.0 ng.mL^{-1}). B) Population distribution, bin size for each histogram was around 60, with experimental and log normal fitting, and %RMSE (% root mean square error) displayed for selected populations. C) SEM of an area of the selected populations at 50 K and 1kV.

The number of ERLs on the sensor surface scales with the concentration of the analyte (see Figure 3-4). It is also important to notice that, as the concentration of the analyte decreases, there are less ERL particles probed within the 1.1 μm^2 laser spot. The small number of particles probed by the laser leads to intensity variations and a skewed (lognormal) intensity distribution. The number of ERLs were further quantified for eight 2.5 x 1.9 μm^2 SEM images of random areas of the sensor surface for each concentration of the IgG analyte.

3.3.4 Population Distribution

The SERS intensity distribution histograms (Figure 3-3B and Figure A-S4 in Appendix A) indicate that a small number of ERLs have highly efficient hotspots, generating SERS signals that are several orders of magnitude higher than the normal Raman scattering measured for the rest of the population, resulting in a SERS intensity population distribution skewed towards a long tail. This type of lognormal intensity distribution has been reported for single-particle SERS measurements.[25,37,39] A lognormal distribution was also described for SERS experiments at low concentrations, but non-single molecule regime, in which small clusters or multiple separated probes are interrogated under the laser beam.[18,37] Coupled particles, clusters, and protrusions strongly affect the local field enhancement and introduce strong variations. These variations become more apparent for surfaces that are not densely packed with the ERLs probe. The use of a gold film as a support substrate for the assay also potentially influence the statistic of the distributions through the creation of additional hotspots between the ERL probes and the metal film. These additional hotspots arise from a coupling between the LSPR of the AuNPs and the thin gold film.[40] In densely ERL-packed substrates, the rare events are less significant relative to the total amount of ERLs under a single laser spot in each measurement; therefore, a Gaussian distribution is more likely.[39] Percent root mean square error (% RMSE) was calculated for all the measured populations and some representative examples are listed in Figure 3-3B. The %RMSE shows the percent deviation of the fitted data points over the mean for each population. The numbers range from 1.6 to 3.6% for the different IgG concentrations. These low %RSME values confirm that the lognormal populations fits are accurate.

The population distributions displayed in Figures 3-10 and 3-3B reflect the statistics of rare events due to a small number of highly enhanced ERL probes. Typically, SERS immunoassays reports from the literature involves the collection of a certain number of single point SERS data from different areas of the sensor surface, and the average intensity is reported with symmetric error bars. This procedure is correct when the ERL concentration of the probe is high enough for a normal distribution, but a lognormal behavior is dominant at low concentrations.

3.3.5 Sensor Performance

Figure 3-4A is the calibration curve generated from the SERS intensity distributions for each concentration of the analyte. A linear calibration curve was constructed with the median SERS intensity of the populations with superposed box plots for each detected concentration.[41] Box plots represent the distribution within the dataset and enables to visualize the data in a more integrated way.[42] The middle line corresponds to the median value of a dataset, the box comprises of the 25th to 75th percentiles, and the whiskers represent 5th and 95th percentiles. The mean is also shown in Figure 3-4 as the small squares above the median (see also Figure A-S3). Since the SERS intensity distributions for the assay are non-Gaussian (Figure 3-3B), it is a more accurate way to represent the range of variations of the measurements within a population. When a calibration curve is constructed with mean values and symmetric error bars based on standard deviation of the populations, the large distribution of intensities is not shown, and the error bars are often smaller than the variations of the data points. The datasets have a considerable spread of values due to the SERS effect.

SEM images were taken for all the IgG concentrations. Eight images, making up 38.1 μm^2 of substrate per concentration were used to construct the plot in Figure 3-4B. The number of ERLs were counted (example of images on Figure 3-3C) within that fixed area and correlated to the median SERS intensity of the populations. The number of ERLs are displayed as a box plot for each concentration, so the spread of values is readily seen. The results of Figure 3-4B show a linear relationship. This direct relationship indicates that even when high variations in SERS intensities is observed, it is still possible to correlate their median value with the number of ERLs probed within the laser spot.

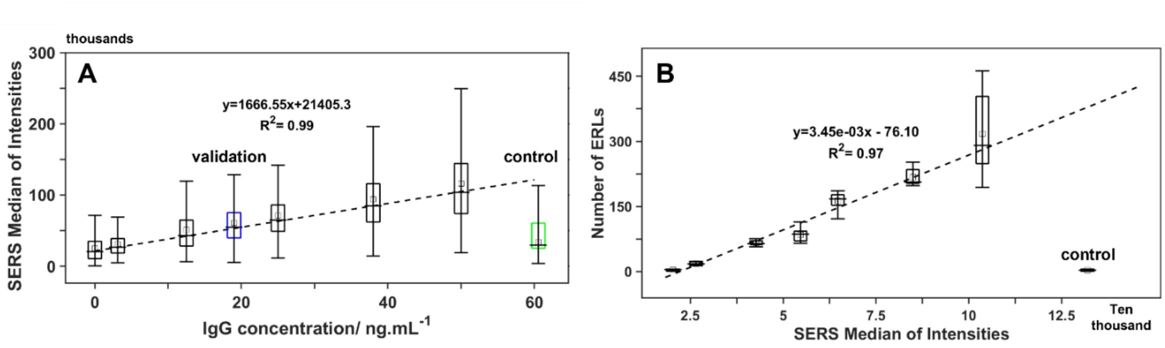

Figure 3-4. A) Box Plot superposed with a calibration curve generated by the median of the intensities under the NB peak for the 7200 measurements for each related IgG concentration. A control, IgM 25 ng.mL^{-1}, and a validation point (19 ng.mL^{-1} IgG) were also measured. B) Box plots superposed with calibration curve for number of ERLs (within 38.1 μm^2) on the substrate surface correlated with the signal median of the assay.

A quality control sample (QC) with a known concentration of IgG equals to 19.0 ng.mL^{-1} was also measured to further validate the assay (indicated in Figure 3-4A). The % error of the predicted versus the actual concentration value determined by our assay for the QC sample was 0.13%. The limit of detection (LOD) and limit of quantification (LOQ) were calculated at a 95% confidence level. LOD was defined as the analyte concentration that produces a signal three times larger than the standard deviation and LOQ as 10 times the standard deviation of the blank. LOD was determined to be 1.11 ng.mL^{-1} or 7.39 pM and LOQ as 9.04 ng.mL^{-1} or 60.30 pM for IgG, within a 95% confidence level.

3.3.6 Impact of Number of Measurements in the Assay's Accuracy

Figure 3-3B demonstrated that the intensity distributions in SERS immunoassays at low concentrations do not follow a normal behavior. The use of medians and boxplots provides a better representation of the calibration curves that explicitly shows the intensity variations for the ERLs distributed on the sensing surface. The robust statistics in Figure 3-3 were obtained by several maps and a large number of SERS spectra (at least 7200 spectra per sample). This massive number of data/spectra led to better accuracy in the SERS-based immunoassay presented here. Since minor variations in the arrangements of the atoms in the ERLs may generate substantial fluctuations of SERS intensity, more measurements are required to account for the large uncertainties that translate to the analytical calibration curves when under-sampled. However, it is important to explore the sampling limitations a bit further to find a compromise between accuracy and the time required for the assay. This information is essential for a wide application of SERS immunoassays.

Figure 3-5 shows the % error in the QC sample when 10, 25, 50, 200 single measurements are selected for each population and for the validation sample and used to construct calibration curves. This is compared with the assay with the total number of measurements (7200) and its QC % error. Each of the random measurements represent a single point spectrum obtained in different areas of the sensor surface. Typically, in the SERS field, researchers use 10 to 20 random spectra to account for SERS intensity variations.

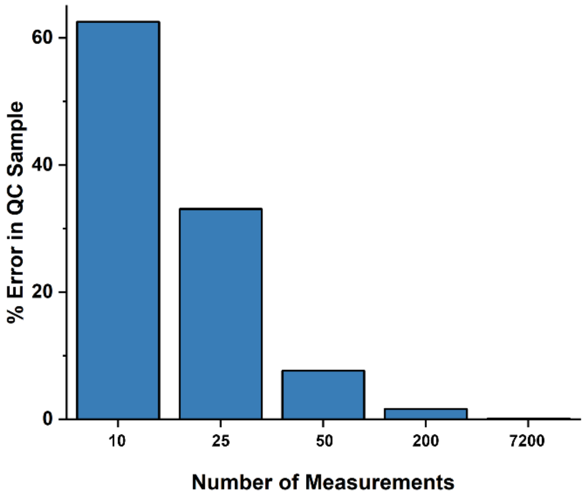

Figure 3-5. Percent error in the QC sample with assays constructed with 10, 25, 50, 200 randomly selected measurements out of the measurement pool compared with the 7200 measurements of the full assay.

Figure 3-5 shows that, for immunoassays at low concentrations, this level of sampling is not enough to provide an accurate determination. Figure 3-5A shows that % error improves asymptotically with the number of measurements, going from 62.6% to 0.13% error with more measurements. A good compromise between time used to measure and low % error is 200 spectra measured, with an % error of 1.61%. This result agrees with previous studies that indicate that 100s of measurements are necessary to obtain statistically relevant parameters for SERS reproducibility.[24] Another interesting aspect is that the quality of the determination improves when the sampling is distributed over a wide area. For instance, a single SERS map with 900 spectra (covering an area of 30 x 30 μm^2) region can lead to a relatively large error in the determination because all 900 spectra were obtained close to each other. Even 4 maps from different areas (42.4 % error) were not enough to recover the same level of accuracy than compared to only 25 random measurements of very distinct regions on the sensor surface. It seems that randomly interrogated spots may better account for the non-homogeneity of the ERLs response and distribution in different regions of the sensor surface. Although the level of variability depends on the substrate and ERLs, this study indicates that fewer measurements of spatially distant regions provide better accuracy than many measurements that are close together, increasing the quality of the immunoassay with less time spent on the data acquisition. The presented experimental data is comprised of duplicate experiments, done separately, and following the same procedure. When QC is calculated for the two datasets, the % difference between the obtained QC values was 3.8%.

3.4 Conclusion

We propose that an approach to improve the application of SERS as an analytical tool lies in embracing the inherent variations of the method and a better understanding of the SERS sampling limitations. This contrasts to a large body of previous investigation that focused on improving the homogeneity of the SERS substrates. In the case of immunoassays, a sufficiently large number of measurements accounts for the SERS effect inherent over-expression of minor dissimilarities and clustering in the sensor surface. Not only the size but also the distance between interrogated areas should be considered for a more reliable sampling. In addition, a more thorough population description and appropriate statistical analysis of each concentration regimen (low to ultra-low regimens - pM and smaller), and high concentrations (nM to μM and up) of SERS reporters should be considered.

3.5 References

(1) Liang, X.; Li, N.; Zhang, R.; Yin, P.; Zhang, C.; Yang, N.; Liang, K.; Kong, B. Carbon-Based SERS Biosensor: From Substrate Design to Sensing and Bioapplication. *NPG Asia Mater* 2021, *13* (1), 8.

(2) Pang, Y.; Wan, N.; Shi, L.; Wang, C.; Sun, Z.; Xiao, R.; Wang, S. Dual-Recognition Surface-Enhanced Raman Scattering (SERS) Biosensor for Pathogenic Bacteria Detection by Using Vancomycin-SERS Tags and Aptamer-Fe3O4@Au. *Analytica Chimica Acta* 2019, *1077*, 288–296.

(3) Hu, B.; Pu, H.; Sun, D.-W. Multifunctional Cellulose Based Substrates for SERS Smart Sensing: Principles, Applications and Emerging Trends for Food Safety Detection. *Trends in Food Science & Technology* 2021, *110*, 304–320.

(4) Wu, X.; Wu, P.; Gu, M.; Xue, J. Ratiometric Fluorescent Probe Based on AuNCs Induced AIE for Quantification and Visual Sensing of Glucose. *Analytica Chimica Acta* 2020, *1104*, 140–146.

(5) Li, J.; Yan, H.; Tan, X.; Lu, Z.; Han, H. Cauliflower-Inspired 3D SERS Substrate for Multiple Mycotoxins Detection. *Anal. Chem.* 2019, *91* (6), 3885–3892.

(6) Fan, M.; Andrade, G. F. S.; Brolo, A. G. A Review on Recent Advances in the Applications of Surface-Enhanced Raman Scattering in Analytical Chemistry. *Analytica Chimica Acta* 2020, *1097*, 1–29.

(7) Langer, J.; Jimenez de Aberasturi, D.; Aizpurua, J.; Alvarez-Puebla, R. A.; Auguié, B.; Baumberg, J. J.; Bazan, G. C.; Bell, S. E. J.; Boisen, A.; Brolo, A. G.; Choo, J.; Cialla-May, D.; Deckert, V.; Fabris, L.; Faulds, K.; García de Abajo, F. J.; Goodacre, R.; Graham, D.; Haes, A. J.; Haynes, C. L.; Huck, C.; Itoh, T.; Käll, M.; Kneipp, J.; Kotov, N. A.;

Kuang, H.; Le Ru, E. C.; Lee, H. K.; Li, J.-F.; Ling, X. Y.; Maier, S. A.; Mayerhöfer, T.; Moskovits, M.; Murakoshi, K.; Nam, J.-M.; Nie, S.; Ozaki, Y.; Pastoriza-Santos, I.; Perez-Juste, J.; Popp, J.; Pucci, A.; Reich, S.; Ren, B.; Schatz, G. C.; Shegai, T.; Schlücker, S.; Tay, L.-L.; Thomas, K. G.; Tian, Z.-Q.; Van Duyne, R. P.; Vo-Dinh, T.; Wang, Y.; Willets, K. A.; Xu, C.; Xu, H.; Xu, Y.; Yamamoto, Y. S.; Zhao, B.; Liz-Marzán, L. M. Present and Future of Surface-Enhanced Raman Scattering. *ACS Nano* 2020, *14* (1), 28–117.

(8) Zhang, X.; Zhang, H.; Yan, S.; Zeng, Z.; Huang, A.; Liu, A.; Yuan, Y.; Huang, Y. Organic Molecule Detection Based on SERS in Microfluidics. *Sci Rep* 2019, *9* (1), 17634.

(9) Litti, L.; Trivini, S.; Ferraro, D.; Reguera, J. 3D Printed Microfluidic Device for Magnetic Trapping and SERS Quantitative Evaluation of Environmental and Biomedical Analytes. *ACS Appl. Mater. Interfaces* 2021, *13* (29), 34752–34761.

(10) Panneerselvam, R.; Sadat, H.; Höhn, E.-M.; Das, A.; Noothalapati, H.; Belder, D. Microfluidics and Surface-Enhanced Raman Spectroscopy, a Win–Win Combination? *Lab Chip* 2022, *22* (4), 665–682.

(11) Lopez, A.; Lovato, F.; Hwan Oh, S.; Lai, Y. H.; Filbrun, S.; Driskell, E. A.; Driskell, J. D. SERS Immunoassay Based on the Capture and Concentration of Antigen-Assembled Gold Nanoparticles. *Talanta* 2016, *146*, 388–393.

(12) Granger, J. H.; Granger, M. C.; Firpo, M. A.; Mulvihill, S. J.; Porter, M. D. Toward Development of a Surface-Enhanced Raman Scattering (SERS)-Based Cancer Diagnostic Immunoassay Panel. *Analyst* 2013, *138* (2), 410–416.

(13) Wang, G.; Lipert, R. J.; Jain, M.; Kaur, S.; Chakraboty, S.; Torres, M. P.; Batra, S. K.; Brand, R. E.; Porter, M. D. Detection of the Potential Pancreatic Cancer Marker MUC4

in Serum Using Surface-Enhanced Raman Scattering. *Anal. Chem.* 2011, *83* (7), 2554–2561.

(14) Wang, G.; Park, H.-Y.; Lipert, R. J.; Porter, M. D. Mixed Monolayers on Gold Nanoparticle Labels for Multiplexed Surface-Enhanced Raman Scattering Based Immunoassays. *Anal. Chem.* 2009, *81* (23), 9643–9650.

(15) Camacho, S. A.; Sobral-Filho, R. G.; Aoki, P. H. B.; Constantino, C. J. L.; Brolo, A. G. Immunoassay Quantification Using Surface-Enhanced Fluorescence (SEF) Tags. *Analyst* 2017, *142* (15), 2717–2724.

(16) Camacho, S. A.; Sobral-Filho, R. G.; Aoki, P. H. B.; Constantino, C. J. L.; Brolo, A. G. Zika Immunoassay Based on Surface-Enhanced Raman Scattering Nanoprobes. *ACS Sens.* 2018, *3* (3), 587–594.

(17) Nolan, J. P.; Duggan, E.; Condello, D. Optimization of SERS Tag Intensity, Binding Footprint, and Emittance. *Bioconjugate Chem.* 2014, *25* (7), 1233–1242.

(18) Freeman, L. M.; Pang, L.; Fainman, Y. Self-Reference and Random Sampling Approach for Label-Free Identification of DNA Composition Using Plasmonic Nanomaterials. *Sci Rep* 2018, *8* (1), 7398.

(19) Narayanan, R.; Lipert, R. J.; Porter, M. D. Cetyltrimethylammonium Bromide-Modified Spherical and Cube-Like Gold Nanoparticles as Extrinsic Raman Labels in Surface-Enhanced Raman Spectroscopy Based Heterogeneous Immunoassays. *Anal. Chem.* 2008, *80* (6), 2265–2271.

(20) Crawford, A. C.; Skuratovsky, A.; Porter, M. D. Sampling Error: Impact on the Quantitative Analysis of Nanoparticle-Based Surface-Enhanced Raman Scattering Immunoassays. *Anal. Chem.* 2016, *88* (12), 6515–6522.

(21) Limpert, E.; Stahel, W. A. Problems with Using the Normal Distribution – and Ways to Improve Quality and Efficiency of Data Analysis. *PLOS ONE* 2011, *6* (7), e21403.

(22) Schlücker, S.; Schaeberle, M. D.; Huffman, S. W.; Levin, I. W. Raman Microspectroscopy: A Comparison of Point, Line, and Wide-Field Imaging Methodologies. *Anal. Chem.* 2003, *75* (16), 4312–4318.

(23) Tian, Y.; Wu, P.; Liu, Q.; Wu, X.; Hou, X. Mapping for Total Surface-Enhanced Raman Scattering to Improve Its Quantification Analysis. *Talanta* 2016, *161*, 151–156.

(24) Mabbott, S.; Xu, Y.; Goodacre, R. Objective Assessment of SERS Thin Films: Comparison of Silver on Copper via Galvanic Displacement with Commercially Available Fabricated Substrates. *Analytical Methods* 2017, *9* (33), 4783–4789.

(25) Shaw, C. P.; Fan, M.; Lane, C.; Barry, G.; Jirasek, A. I.; Brolo, A. G. Statistical Correlation Between SERS Intensity and Nanoparticle Cluster Size. *J. Phys. Chem. C* 2013, *117* (32), 16596–16605.

(26) Brennan, J. L.; Hatzakis, N. S.; Tshikhudo, T. R.; Razumas, V.; Patkar, S.; Vind, J.; Svendsen, A.; Nolte, R. J. M.; Rowan, A. E.; Brust, M. Bionanoconjugation via Click Chemistry: The Creation of Functional Hybrids of Lipases and Gold Nanoparticles. *Bioconjugate Chem.* 2006, *17* (6), 1373–1375.

(27) Elliott, E. W.; Ginzburg, A. L.; Kennedy, Z. C.; Feng, Z.; Hutchison, J. E. Single-Step Synthesis of Small, Azide-Functionalized Gold Nanoparticles: Versatile, Water-Dispersible Reagents for Click Chemistry. *Langmuir* 2017, *33* (23), 5796–5802.

(28) Douhal, A. Photophysics of Nile Blue A in Proton-Accepting and Electron-Donating Solvents. *J. Phys. Chem.* 1994, *98* (50), 13131–13137.

(29) Lockhart, C. L.; Conger, M. A.; Pittman, D. S.; Liptak, M. D. Hydrogen Bond Donation to the Heme Distal Ligand of Staphylococcus Aureus IsdG Tunes the Electronic Structure. *J Biol Inorg Chem* 2015, *20* (5), 757–770.

(30) Kozlowski, R.; Ragupathi, A.; Dyer, R. B. Characterizing the Surface Coverage of Protein-Gold Nanoparticle Bioconjugates. 2019, 24.

(31) Koczula, K. M.; Gallotta, A. Lateral Flow Assays. *Essays Biochem* 2016, *60* (1), 111–120.

(32) Hirlekar Schmid, A.; Stanca, S. E.; Thakur, M. S.; Thampi, K. R.; Raman Suri, C. Site-Directed Antibody Immobilization on Gold Substrate for Surface Plasmon Resonance Sensors. *Sensors and Actuators B: Chemical* 2006, *113* (1), 297–303.

(33) Iijima, M.; Kadoya, H.; Hatahira, S.; Hiramatsu, S.; Jung, G.; Martin, A.; Quinn, J.; Jung, J.; Jeong, S.-Y.; Choi, E. K. Nanocapsules Incorporating IgG Fc-Binding Domain Derived from Staphylococcus Aureus Protein A for Displaying IgGs on Immunosensor Chips. *Biomaterials* 2011, *32* (6), 1455–1464.

(34) Turková, J. Oriented Immobilization of Biologically Active Proteins as a Tool for Revealing Protein Interactions and Function. *Journal of Chromatography B: Biomedical Sciences and Applications* 1999, *722* (1–2), 11–31.

(35) Lua, B.; Smytha, M. R.; O'Kennedyb, R. Oriented Immobilization of Antibodies and Its Applications in Lmmunoassays and I m m u Nosensors. 1996, *121*, 4.

(36) Zimbone, M.; Baeri, P.; Calcagno, L.; Musumeci, P.; Contino, A.; Barcellona, M. L.; Bonaventura, G. Dynamic Light Scattering on Bioconjugated Laser Generated Gold Nanoparticles. *PLOS ONE* 2014, *9* (3), e89048.

(37) Izumi, C. M. S.; Moffitt, M. G.; Brolo, A. G. Statistics on Surface-Enhanced Resonance Raman Scattering from Single Nanoshells. *J. Phys. Chem. C* 2011, *115* (39), 19104–19109.

(38) Schulze, G.; Jirasek, A.; Yu, M. M. L.; Lim, A.; Turner, R. F. B.; Blades, M. W. Investigation of Selected Baseline Removal Techniques as Candidates for Automated Implementation. Appl Spectrosc 2005, 59 (5), 545–574.

(39) dos Santos, D. P.; Temperini, M. L. A.; Brolo, A. G. Intensity Fluctuations in Single-Molecule Surface-Enhanced Raman Scattering. *Acc. Chem. Res.* 2019, *52* (2), 456–464.

(40) Sisco, P. N.; Murphy, C. J. Surface-Coverage Dependence of Surface-Enhanced Raman Scattering from Gold Nanocubes on Self-Assembled Monolayers of Analyte. *J. Phys. Chem. A* 2009, *113* (16), 3973–3978.

(41) Limpert, E.; Stahel, W. A.; Abbt, M. Log-Normal Distributions across the Sciences: Keys and Clues: On the Charms of Statistics, and How Mechanical Models Resembling Gambling Machines Offer a Link to a Handy Way to Characterize Log-Normal Distributions, Which Can Provide Deeper Insight into Variability and Probability—Normal or Log-Normal: That Is the Question. *BioScience* 2001, *51* (5), 341–352.

(42) Moeini, B.; Haack, H.; Fairley, N.; Fernandez, V.; Gengenbach, T. R.; Easton, C. D.; Linford, M. R. Box Plots: A Simple Graphical Tool for Visualizing Overfitting in Peak Fitting as Demonstrated with X-Ray Photoelectron Spectroscopy Data. *Journal of Electron Spectroscopy and Related Phenomena* 2021, *250*, 147094.

Chapter 4: A Digital SERS Protocol for the Determination of SARS-CoV-2 in Saliva Samples

This chapter is based on the work: "A Digital SERS Protocol for the Determination of SARS-CoV-2 in Saliva Samples" by Ariadne Tuckmantel Bido and Alexandre G. Brolo currently under review - manuscript ID: se-2023-001727.

ATB performed all experiments, data treatment and helped with writing of the manuscript.

Surface-enhanced Raman (SERS)-based immunoassays are emerging as a solution for early diagnosis and screening of diseases. SERS as a readout strategy brings high sensitivity, the possibility of simultaneous detection of distinct markers, sensor stability and limits of detection that extend to ultra-low concentrations (pM range). Here, we focused on SERS-based heterogeneous immunoassays, in which the number of extrinsic Raman labels (ERLs) at the sensor surface is related to the concentration of the intended target. The ERLs are selective to the target and boost the signal of a Raman reporter. However, as the concentration of the target biomarker decreases, the number of ERLs per unit of area (mm^2) also decreases, leading to a small number of ERLs being probed within an exciting laser spot. This poor sampling adds to the large intensity variations inherent to the SERS effect, resulting in a loss in the linearity between the SERS signal and the marker/target analyte concentration. This characteristic has rendered SERS-based immunoassays unreliable for quantification at low bioanalyte concentrations (pM or less).

We propose the use of a digital quantification protocol to overcome this problem. A SERS-based sandwich immunoassay was developed for the detection of the SARS-CoV-2 S1-S2 spike protein in saliva. A conventional data analysis was compared to the digital protocol for the same dataset. The digital protocol recuperated good linearity for the calibration curve of S1-S2 Spike protein determination. The digital quantification protocol is simple and can be applied to any labeled SERS-based heterogeneous immunoassays in low-concentration regimens (pM or less).

4.1 Introduction

SERS-based immunoassays have unique advantages over other methods.[1] Firstly, SERS-based systems can reach sensitivities up to the single molecule (SM) regimen due to the large enhancement of the Raman signal caused by the localization and amplification of the optical excitation (and scattering) by surface plasmon resonances.[2] This phenomenon enables the construction of assays with very low limits of detection.[3] Secondly, Raman bands are narrow (a few nm), permitting efficient spectroscopic encoding and high throughput multiplexing assays.[4–6] This feature contrasts with the widely used fluorescent-based assays, such as ELISA, in which the broad emission bands lead to large spectral overlap.[5,7] Thirdly, SERS is less prone to sample bleaching and quenching as long as the laser power is properly controlled.[8,9] The high stability of these sensors permits a vast number of measurements without a time limitation. Fast and sensitive SERS immunoassays have been employed for SARS-CoV-2 detection in saliva, with results better than the commercially available lateral flow tests, by aggregation of immunocomplexes with gold-coated magnetic nanoparticles.[10]

There are different formats of SERS-based immunoassays, namely heterogeneous, homogeneous, competitive and noncompetitive assays and they can be either labeled or non-labeled.[11] Here we focus in a labeled, heterogeneous and noncompetitive assay.[8] The SERS probes are called extrinsic Raman labels, or ERLs.[12] It consists of gold nanoparticles that contains Nile Blue (NB), a strong Raman scatterer, and an antibody against the S1 subunit of the SARS-CoV-2 spike protein as a recognition element. Generally, in these types of two-site or sandwich immunoassays, the SERS intensities of the Raman reporter present on the ERLs are directly correlated to the antigen concentration.

SERS-based sandwich immunoassays have been used quantitatively.[4,13,14] They usually rely on a linear relationship between the average Raman intensity of a particular spectral feature of a SERS reporter and the concentration of the target analyte.[4,15,16] However, this approach becomes challenging as the concentration of the analyte decreases and the probability of a statistically significant number of SERS probes to be illuminated by the laser excitation also decreases.[15,17] Additionally, there is large variation of signal intensities attributed to the non-homogenous distribution of hotspots around the Raman reporters present at the surface of the ERLs.[18–20]

In this study, we constructed a SERS-based sandwich assay for detection of SARS-CoV-2 (2019-nCoV) spike F + S2 ECD-His recombinant protein, dubbed S1-S2 spike protein, in saliva in the pM range. A conventional data analysis using SERS intensities was compared to a digital quantification protocol for this system. The digital protocol counts or "digitizes" the SERS signal by attributing 1 or 0 for intensity values above or below a threshold.[21] The rationale for this procedure assumes a high probability of having either none or one (or a small number) of ERL under the illuminated laser at ultralow concentrations. This approach was introduced by our group in the context of ultralow quantification (pM) in single-molecule SERS (SM-SERS) conditions.[22] Later, similar approaches were implemented by other groups even in SERS-based immunoassays. For instance, the digital protocol was used to filter the background noise on signal quantification for a sensing platform for SARS-Cov-2.[23] The calibration curve was constructed by plotting the digital counts multiplied by the Raman intensities, filtering the signal below a defined threshold. A second group used the digital protocol to filter false signals by applying a classical least squares (CLS) approach in a dual-reporter SERS bioassay for detection of human α-thrombin.[24] A signal was considered true only if the measurement contained the peak of the Raman reporter present on the sensor and the second Raman reporter present in the ERL.

In this paper, we developed a purely digital SERS protocol that relates the count number to antigen concentration. The procedure does not require expert statistical knowledge and was applied to a single Raman reporter present in the ERLs. The sensor was used to detect S1-S2 spike protein in human saliva samples. The assay presented a LOD of 6.3 ng/mL or 34.9 pM and a LOQ of 19.0 ng/ mL or 105.7 pM, within a 95% confidence level.

4.2 Materials and Methods

4.2.1 Materials

Glass slides (1″ x 1″ x 0.040″) coated with Cr 50 Å and Au 100 nm were purchased from Evaporated Metal Films (EMF Dynasil). SARS-CoV-2 (2019-nCoV) Spike S2 Antibody and SARS-CoV-2 (2019-nCoV) Spike S1 + S2 ECD-His Recombinant Protein, dubbed in this manuscript as S1-S2 Spike Protein for simplicity, were purchased from Sino Biological. Anti-Spike S1 Monoclonal Antibody (SARS-CoV-2) was purchased from BPS Bioscience. SARS wt Spike (TEV foldon his) used as a control was provided by ImmunoPrecise Antibodies (IPA). PBS pH 7.2 (1X) was purchased from Gibco. Sodium azide, Bovine Serum Albumin (BSA), 3-mercaptopropionic acid (3 MPA), 11-mercaptoundecanoic acid (11 MUA) and ethanolamine-hydrochloride were purchased from Sigma-Aldrich. Nile Blue A perchlorate, or Nile Blue (NB) and chloroauric acid ($HAuCl_4 \cdot 3H_2O$) were purchased from Aldrich. Sodium citrate salt dihydrate, and polyoxyethylene-20 (tween 20) were purchased from Biotech. N-ethyl-N'-(3-diethylaminopropyl) carbodiimide (EDC) and sulfo-(N-hydroxysulfosuccinimide sodium salt (sulfo NHS) were purchased from ProteoChem™; HS-PEG-COOH, MW 3000 and methoxy -PEG-thiol, MW 5000 were purchased from Rapp Polymere. Ethyl alcohol anhydrous was purchased from Commercial Alcohols. The Sylgard 184 silicone elastomer kit was purchased from Dow Corning Corporation. Disposable sterile biopsy punches 5 mm were purchased from Ted Pella, Inc. Tissue culture dishes,35 mm, surface treated and sterile was purchased from VWR (Avantor).

All aqueous solutions were prepared with ultrapure water obtained from a Nanopure Diamond™, 18.2 MΩ.cm at 25 °C. Centrifugation was conducted using an accuSpin Micro 17 from Fisher Scientific.

4.2.2 Synthesis of Gold Nanoparticles (AuNPs)

Colloidal gold nanoparticles (AuNPs) were fabricated by reducing chloroauric acid ($HAuCl_4 \cdot 3H_2O$) with citrate as described elsewhere.[25] Briefly, 99 mL of ultrapure water was brought to boil in a 150 mL beaker covered with a watch glass. Next, 1 mL of a 1% m/v $HAuCl_4 \cdot 3H_2O$ solution was added at 800 rpm stirring for 1 minute, followed by 1 mL of a 1% m/v trisodium citrate solution. After 5 minutes under stirring, 1 mL of a 5% m/v sodium azide solution was added dropwise, and the heat was turned off. The colloid was left stirring until it reached room temperature and was stored in a glass vial at 4 °C. This synthesis yields a 31 ± 4 nm particle. This size was determined by averaging the diameter of 2065 AuNPs in TEM images using Image J software. The concentration was estimated considering the average size of the nanoparticles and the amount of gold added to the reaction as 2×10^{10} AuNPs/mL.

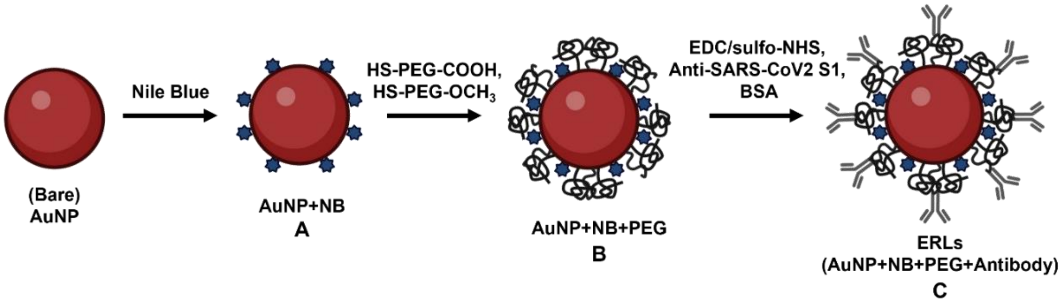

Figure 4-1. Preparation of ERLs. Nile Blue (NB) is adsorbed onto bare gold nanoparticles (A), followed by PEGylation (B) and covalent biding of anti-SARS-CoV-2 antibody against S1 subunit (C).

4.2.3 Preparation of the extrinsic Raman labels (ERLs)

The preparation of the ERLs is depicted in Figure 4-1. To 2 mL of the AuNPs, 300 µL of a 5 µM freshly prepared NB solution in water was added dropwise at 1000 rpm, under stirring. NB acts as a Raman reporter and is adsorbed to the AuNPs. The bare AuNP containing adsorbed NB is called AuNP+NB (Figure 4-1A). Directional conjugation of the antibody was achieved by pegylating the AuNPs using two thiolated PEGs as described by Qian et al.[26] After 20 minutes of the NB solution addition to the gold colloid, 160 µL of a 200 µM HS-PEG-COOH (3 KDa) PEG solution was added and left stirring for 30 minutes. Then, 160 µL of a 200 µM methoxy -PEG-thiol (5 Kda) PEG solution was added and let stirring for 2 hours. Then the nanoparticles were centrifuged at 8000 g for 15 minutes. The supernatant was discarded, and the nanoparticles were resuspended in 2 mL of ultrapure water. The particles now have NB adsorbed and a PEG layer and they are referenced as AuNP+NB+PEG (Figure 4-1B).

The PEG ligands are heterobifunctional, containing a dithiol group that anchors onto the gold surface and a terminal carboxyl group that is available for a crosslinking reaction with EDC/sulfo NHS.[27] Following the pegylation of the particle (AuNP+NB+PEG), 1 mL aliquots were separated in glass vials. To each 1 mL aliquot, it was added 8 µL of a freshly prepared 1 mg.mL^{-1} EDC solution, followed by 16 µL of freshly prepared 1 mg.mL^{-1} sulfo NHS solution, under stirring, for 35 minutes. Then the nanoparticles were centrifuged at 8000 g for 15 minutes and resuspended in 2 mL of PBS-10 (PBS 10 times diluted in ultrapure water). The colloid was then separated into 500 µL portions, in small glass vials, and put into vigorous stirring (1600 rpm). 25 µL of anti-SARS-CoV-2 antibody against S1 subunit 0.2 mg.mL^{-1} was added to each vial and then the vials were stirred for 2.5 hours, under a specimen cup covered with aluminum foil. The carboxylic moiety of the PEG reacts with the primary amines in the lysine residues of the antibodies, forming an amide, anchoring the antibodies in an oriented manner, in which the Fab fragments can be assessed for antigen binding. [28] This step is very important and if the stirring is not adequate, it can lead to aggregation of the particles. To each vial, it was then added 50 µL of a 1% BSA solution in PBS-10 and let stirring for 30 minutes. Then the nanoparticles were centrifuged at 8000 g for 15 minutes and resuspended in 1 mL of PBS-10. The nanoparticles now are referenced as ERLs and consist of AuNP+NB+PEG+Antibody (Figure 4-1C).

The binding capacity of the ERLs to the antigen was investigated by a lateral flow assay (LFA)[19,29] developed in parallel. The results for the LFA are presented in Appendix B, Figure B-S1. The LFA indicates that there is a high affinity between the ERLs and the antigen, S1-S2 Spike protein and no significant cross reactivity with the control, SARS wt Spike (TEV foldon his).

4.2.4 Sensor Surface Preparation

The sensor surface preparation was based on Holzer et al.[30] A self-assembled monolayer (SAM) is formed on a gold-covered glass slide through the chemisorption of 3-mercaptopropionic acid (3 MPA) and 11-mercaptoundecanoic acid (11 MUA) via their thiol functional groups. A SARS-CoV-2 (2019-nCoV) Spike S2 antibody was then covalently linked to the SAMs via carboxyl to amine crosslinking using EDC/sulfo NHS. First, the gold-covered glass slides were marked with an electric pen, to demark regions where the assay would be conducted. Next, the slides were cleaned with piranha solution for 10 minutes and washed abundantly with ultra-pure water and dried under a N_2 stream.

Each clean slide was fit to the lid of a 35 mm tissue culture dish and then put inside a 60 x 15 mm plastic petri dish with 4 mL of the self-assembly forming solution added to the lid. The SAM forming solution consists of a mixture of 3 MPA and 11 MUA at 10×10^{-3} M in 10:1 volume ratio, respectively, in ethanol.

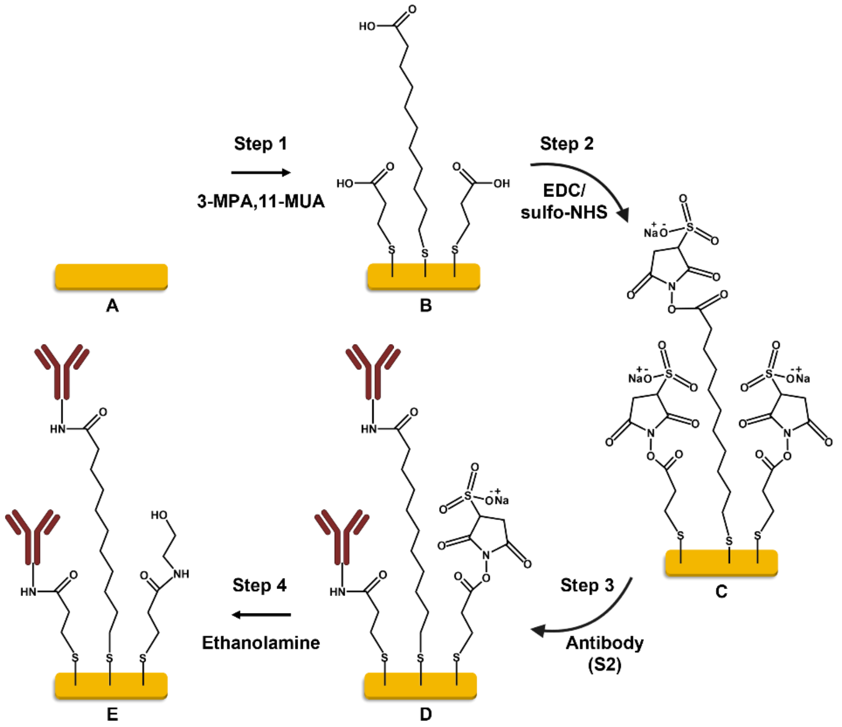

Figure 4-2. Functionalization of the gold-covered glass slide showing the stepwise formation of the self-assembled monolayers (SAMs).

The petri dish was covered with its lid, then covered with aluminum foil and left undisturbed at room temperature for at least 24 hours for the SAMs formation. The slides were then washed with ethanol abundantly with a squirt bottle and dried under a N_2 stream. The stepwise functionalization of the SAMs is shown in Figure 4-2. A clean gold-covered glass slide (A) is added to a mixture of 3-mercaptopropionic acid (3-MPA) and 11-

mercaptoundecanoic acid (11-MUA) in a 10:1 (v:v) ratio (Step 1). This ratio results in a close-packed, ordered monolayer by chemisorption of the thiol moieties in the gold on the sensor that offers less steric hindrance and provides better immobilization efficiency of the antibodies (B).[31] The carboxylic terminal ends of the SAMs were activated with EDC/sulfo NHS (Step 2) for conjugation with the primary amines of the SARS-CoV-2 (2019-nCoV) spike S2 antibody (C), forming an amide bond (Step 3), and anchoring the antibodies to the sensor (D).[32,33] Nonreacted activated functionalities were blocked with ethanolamide (Step 4), resulting in an antibody-covered sensor (E).[31]

Next, the slides were mounted into a 3D printed assay platform with a PDMS mask demarking the areas for reactions, described elsewhere.[19] Details on this platform are in the Appendix B (Figure B-S2). Using the PDMS mask A (Figure B-S2A), 600 μL of an EDC/sulfo-NHS solution (0.2 M EDC and 0.05 M sulfo-NHS) was added to the platform. The system was placed inside a humidity chamber and left to react for 2 hours. The slides were then taken out of the platform, washed abundantly with ultra-pure water, and dried under a N_2 stream. The system was re-assembled with PDMS mask B (Figure B-S2B), containing 5 mm holes, cut with biopsy punches, and aligned with the marked regions in the slides. 25 μL of a 100 μg.mL^{-1} SARS-CoV-2 (2019-nCoV) Spike S2 in PBS-10 was added to each demarked region. The platforms were placed in a humidity chamber, closed with parafilm overnight at 8 °C. The aqueous contents of the wells were then sucked gently with a micropipette, and each well was washed with 30 μL of PBS-10, three times. Then, 30 μL of 1M ethanolamide solution was added to each well, and the platforms were left into the humidity chamber for another one hour. The wells were washed again three times with 30 μL of PBS-10. Then 30 μL of 0.5% BSA solution in PBS-10 was added to each well for 1 hour and the system was again placed inside the humidity chamber. Then each well was washed three times with 30 μL of PBS-10. The finalized sensor surface was stored in the fridge immersed in PBS-10 for later use.

4.2.5 SERS Immunoassay

30 μL of the spiked antigen in the desired concentrations, ranging from 1.6 ng.mL^{-1} to 50.0 ng.mL^{-1} or 1.6 ng.mL^{-1} to 200.0 ng.mL^{-1}, prepared in either PBS-10 or diluted saliva, were added to the sensor surface. Each experiment was performed in duplicates. The experiments with PBS-10 were performed first, so the protocol could be developed using a simpler matrix. The results for the assay conducted in PBS-10 together with details of the data analysis are present as Appendix A. To prepare the diluted saliva, 3.5 mL of saliva from a healthy volunteer was collected in a 15 mL Falcon tube using the drool method. The saliva donor volunteer refrained from consumption of anything, but water 45 minutes before collection. 3.5 mL of PBS-10 was added to the raw saliva samples and the mixture was vortexed. Aliquots were added to Eppendorf tubes and centrifuged at 6 G for 20 minutes, to remove any cellular debris. The supernatant was collected and spiked with the appropriated concentration of S1-S2 spike protein. The dilution of the saliva matrix was required to decrease the viscosity of the sample. It is important to have the same dilution for all the concentrations. The final dilution ratio was 4X PBS-10 to pure saliva in volume. For instance, an example of dilution consisted of adding 300 μL of 100.0 ng.mL^{-1} of antigen (S1-S2 spike protein) prepared in PBS-10 to 300 μL of the 2X diluted saliva, leading to a 50.0 ng.mL^{-1} final solution. Similarly, a 25 ng.mL^{-1} solution was made by adding 300 μL of 50.0 ng.mL^{-1} of antigen in PBS-10 to 300 μL of the 2X diluted saliva.

Additionally, a variety of controls were run in duplicates for each assay, including only PBS-10 or diluted saliva (blank), SARS wt Spike at 25.0 ng.mL^{-1} in either PBS-10 or diluted saliva (negative control).

The sensor platforms were incubated with the samples for 3 hours inside the humidity chamber, at room temperature. The slides were washed with 30 µL of PBS-10T (PBS-10 with 0.1% tween 20), twice. This is done by gently aspirating the contents of the PDMS wells (PDMS mask B, Figure B-S2B), with a micropipette and adding the washing solutions. Followed by three 30 µL washes with PBS-10 to each PDMS well. The slides were then stored at this point in a fridge, with 50 µL PBS-10 in each well, inside the humidity chamber for later use, or conduct the next step straightaway.

The last step of the assay was adding 30 µL of freshly prepared ERLs to each PDMS well, for 2 hours, inside the humidity chamber, at room temperature. Followed by two 30 µL washes with PBS-10 to each PDMS well. The PDMS was then discarded, and the sensors were washed abundantly with ultrapure water with a squirt bottle and gently dried in N_2 stream. The slides were then ready to be measured in the Raman system.

4.2.6 Assay Overview

The SERS-based sandwich immunoassay principle is depicted in Figure 4-3. The sensor surfaces contain anti-SARS CoV-2 antibody against the S2 subunit of the SARS-CoV-2 virus. Different concentrations of the S1-S2 spike protein in either PBS-10 or diluted saliva plus two controls were added, in duplicates, to separate wells in the PDMS. The antigen interacts with the antibodies present in the sensor. ERLs are later added to the assay, containing anti-SARS-CoV-2 antibody against S1 subunit. The antibodies in the ERLs interact with the antigen and the amount of ERLs on the surface of the sensor will be lower for a lower concentration of antigen (Figure 4-3A) and higher for a higher concentration of antigen (Figure 4-3B). Controls were run to determine background noise from nonspecific binding and to determine the level of cross-reactivity.

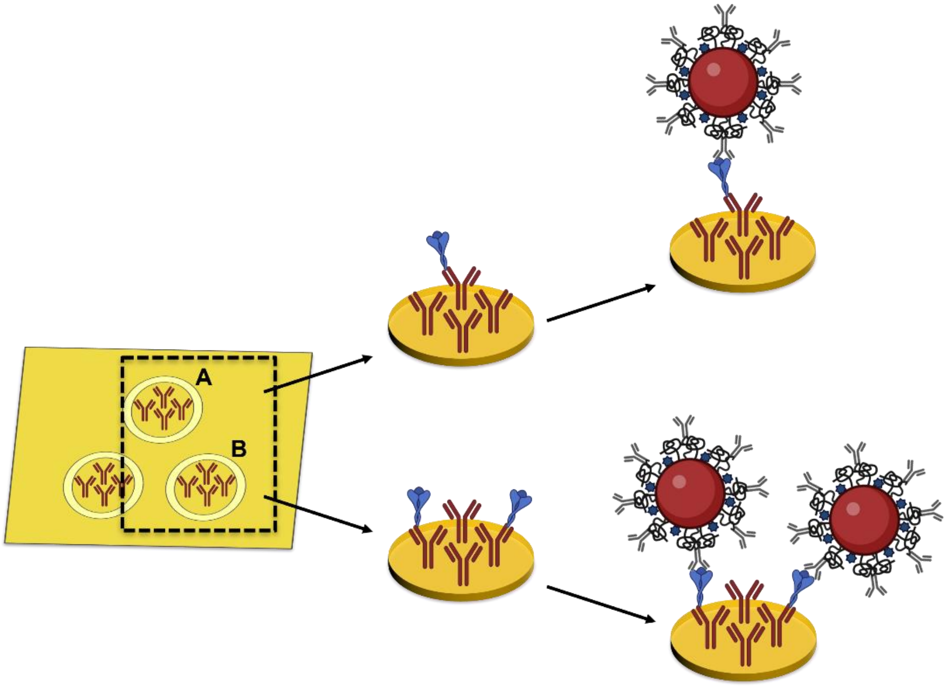

Figure 4-3. SERS-based sandwich assay principle. Gold-coated glass slides contain anti-SARS-CoV-2 antibody against S2 subunit. Slides were incubated with different concentrations of S1-S2 spike protein (antigen) in diluted saliva. Next, the slides were incubated with modified gold nanoparticles with anti-SARS-CoV-2 antibody against S1 subunit (ERLs). A) Areas exposed to lower antigen concentration have fewer ERLs on the sensor surface. B) Areas exposed to higher antigen concentration have more ERLs on the sensor surface.

4.2.7 Instrumentation

All nanoparticles were characterized by ultraviolet-visible (UV-Vis), dynamic light scattering (DLS), ζ-potential, and transmission electron microscopy (TEM). The size and shape of the particles were estimated from UV-Vis spectroscopy measured using a Biotek Cytation 5 (Agilent) plate reader and from TEM images, taken in a Joel 1011 Transmission Electron Microscope. An Anton Paar LiteSizer 500 was used to measure the hydrodynamic radius (DLS) and the surface charge (ζ-potential).

Raman measurements were recorded on a Renishaw inVia Raman Microscope with a 633 nm (He–Ne) excitation laser, and a 50 X Leica Germany 5660 objective (NA=0.75), 10 seconds integration time, 10 mW laser power, grating 1200 l/mm. SERS maps of random areas of the sensors consisted of 900 spectra of 30 by 30 μm^2 regions, 1 μm step size, using StreamLine® image acquisition. The collection time was 6.5 minutes per map, with the beam spread around 0.22 mm^2, the power density of 45.5 mW/mm^2, and the pixel size was 1.1 μm^2. SEM images were taken from the Raman interrogated surfaces using a Hitachi S-4800 scanning electron microscope at magnification 50.0k and 1kV. Figure B-S3 in Appendix B shows an example of SEM image for the PBS-10 sensor surface at 1.56 and 50 $ng.mL^{-1}$ S1-S2 Spike Protein concentration.

4.3 Results and Discussion

4.3.1 ERLs Characterization

The particle characterization is presented in Figure 4-4. Figure 4-4A, 4-4B and 4-4C presents UV-Vis, dynamic light scattering (DLS) and ζ- potential for the bare AuNP (denominated AuNP), AuNP+NB+PEG and ERLs (AuNPs+NB+PEG+Antibody). Table 3-1 compiles the averages of triplicate measurements of UV-Vis and DLS and duplicates of ζ- potential measurements for the modified stages of the particle. There was a redshift of the LSPR peak as the particles were modified, from 523.2 ± 0.1 for the bare AuNPs, to 525.1 ± 0.1 for AuNP+NB+PEG and to 525.6 ± 0.1 for the ERLs. Similarly, there was an increase in the DLS from 36.8 ± 0.4 to 54.3 ± 0.3 and finally to 80.3 ± 0.2 as the particles were progressively modified. This increase in size distributions is expected as the particles are coated with a thiol-PEG layer that then have the COOH moieties covalently linked to the anti-SARS-CoV-2 antibody forming amide bonds. The ζ- potential changed from -37.6 ± 1.6 to -30.7 ± 1.2 as the PEG layer was added to the particles. The increase in the ζ-potential is an indication of replacement of the citrate layer to the thiol-PEG layer in the particle. [34–36] After antibody conjugation, the ζ- potential further increases to -17.3 ± 0.7. This trend is in accordance to previous observations reported in the literature. [37,38] Figure 4-4D and 4-4E show TEM images of the bare AuNP and the ERLs. The bare AuNP particles have an average size of 31 ± 4 nm, and there is no change in size of the AuNP core after conjugation, indicating that there was no significant aggregation.

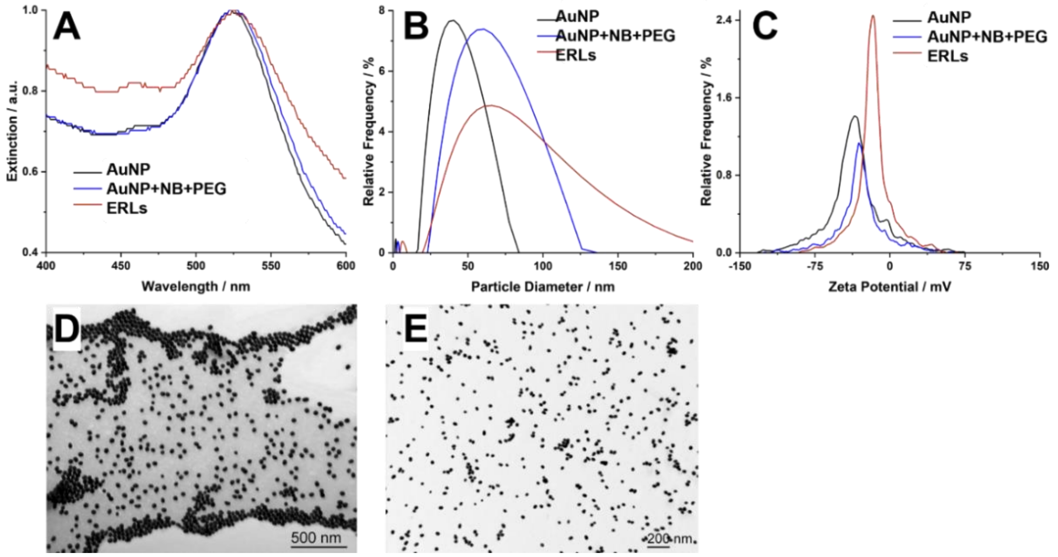

Figure 4-4. A) Normalized UV-Vis B) Dynamic light scattering (DLS) and C) ζ-potential for the bare AuNP (AuNP), pegylated (AuNP+NB+PEG) and covalently linked anti-SARS-CoV-2 antibody against the S1 subunit (ERLs). D) and E) shows TEM images for the bare gold nanoparticles and ERLs, respectively.

Table 4-1. UV-Vis and DLS triplicates and ζ- potential duplicates for bare AuNP, pegylated AuNPs (AuNP+NB+PEG) and ERLs.

Nanoparticle	UV-Vis peak wavelength	Hydrodynamic diameter / nm	Zeta Potential / mV
AuNP	523.2 ± 0.1	36.8 ± 0.4	-37.6 ± 1.6
AuNP+NB+PEG	525.1 ± 0.1	54.3 ± 0.3	-30.7 ± 1.2
ERLs	525.6 ± 0.1	80.3 ± 0.2	-17.3 ± 0.7

4.3.2 Digital Protocol and Assay Considerations

The assay was first developed in PBS-10, without the saliva matrix. The saliva introduces a more complex media, with lipids, proteins, and inorganic substances, and is prone to unspecific binding in the system.[39,40] The results for the assay in saliva will be presented here, while the data for the experiments conducted in PBS-10 are presented in Appendix B.

Raman mappings were obtained from immunoassays using all the different tested concentrations of the S1-S2 spike protein. Three random 30 by 30 μm^2 maps, with 900 measurements per map, were taken from each sensor surface. The assays were conducted in duplicate, and each sample was measured twice; therefore, the analyzed dataset consisted of a total of twelve maps, or 10,800 SERS measurements per concentration of the analyte in the saliva matrix.

The data analysis (more details are available as Appendix B, Figure B-S4) consists of baseline correcting each individual spectrum using the Savitsky-Golay signal removal method, described elsewhere.[41] Then, the Peakfit function in the MATLAB software was applied for NB phenoxazine ring mode, centered at 592 cm^{-1}, followed by integration. Peakfit used a Lorentzian line shape covering a range of 15 wavenumbers around the centered peak. 20 iterations were used for the fit. A threshold was defined for the digital quantification protocol, i.e., the attribution of values of 0 (no counts) and 1 (counts) to each pixel in the mappings. The goal of the digital protocol is to account for the large variation of the SERS signal observed when the amount of ERLs at the surface illuminated by the probing laser is small (ultralow concentrations). In this case, the assay considers the number of counts, rather than SERS signal intensity, for the generation of a calibration curve. Figure B-S2 in Appendix B shows an example of the data treatment. The area of the background (between 610 and 640 cm^{-1}) in the vicinity of the NB peak of interest was measured using a trapz function on MATLAB. The values for this background were recorded in each spectrum (pixel) and compared to the areas recorded under the NB phenoxazine ring mode at 592 cm^{-1}. A count of 1 was assigned to the pixel in the mapping when the NB peak area was three times higher than the background; otherwise, a value of 0 was assigned to the pixel. The signal detection limit set at 3 standard deviations above the background signal was decided considering the IUPAC definition commonly used in analytical chemistry for limits of detection (LOD).[42]

Figure 4-5 shows representative digital maps for the assay conducted in saliva at different concentrations of the S1-S2 spike protein. The white squares in Figure 4-5 represent the pixels that were assigned the value of 1, while the black squares indicate the pixels assigned with a value of 0 (no counts). Additionally, the number of ERLs per μm^2, determined independently by scanning electron microscopy (SEM) are shown in red in Figures 5. The slides were plasma cleaned for 30 minutes before the acquisition of the SEM images to improve imaging quality and resolution. It is important to emphasize the stability of the sensor surface. Reproducible results were obtained from the SERS maps even 8 months after the assay (for sensors stored in the fridge, as described above). However, the plasma cleaning step, required for the SEM, rendered the sensors unresponsive in future SERS determinations. Six SEM images were taken for each concentration of S1-S2 spike protein in saliva. In contrast to the experiments with PBS-10 (presented in the Appendix B file), the use of saliva as matrix made it harder to focus the electron beam on the ERLs for SEM images, probably due to other proteins and contaminations that remained on the sensor surface. Each SEM image was 2.55 µm by 1.90 µm. As expected, the estimated number of ERLs per µm^2 increased with the increase of antigen concentration, as denoted in Figure 4-5. A maximum of ~2.2 ERLs/mm^2 was reached at 25 ng.mL^{-1} of S1-S2 spike protein.

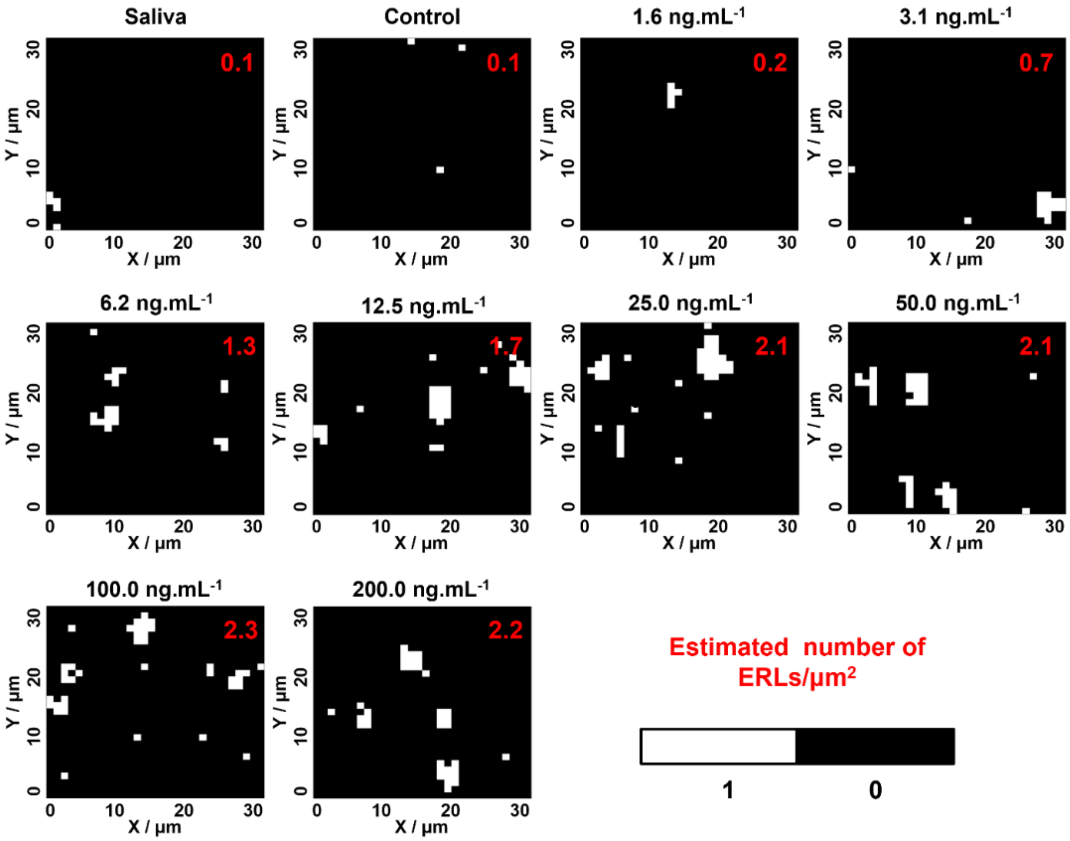

Figure 4-5. Representative digital maps for the saliva assays. The white squares represent the positive events (assigned as 1), and the black squares are the negative events (assigned as 0). The estimated number of nanoparticles per µm^2 based on SEM images are indicated in red.

The SEM images were further analyzed to estimate the total number of ERLs for each specific concentration of the antigen. The digital assignment presented in Figure 4-5 assumes that each pixel assigned "1" contains 1 (or a small number of) ERL. Therefore, a linear relationship between the number density of ERLs and the digital count is expected. This linear relationship is confirmed in Figure 4-6.

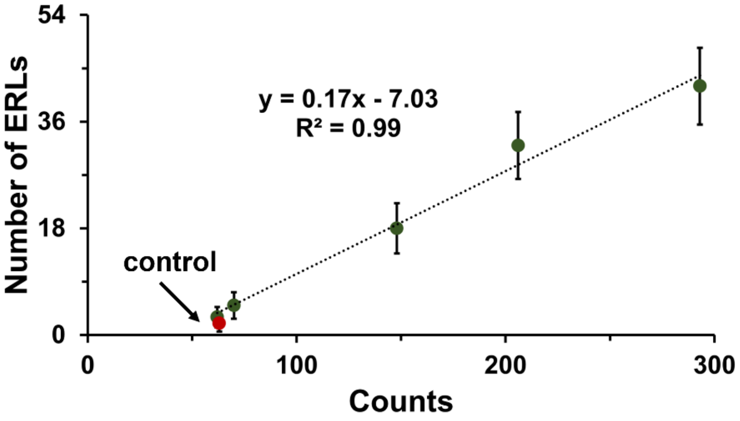

Figure 4-6. Linear relationship between the number of ERLs on the surface of the sensor determined by SEMs and the SERS digital counts for the assay in saliva.

It is worth noticing some clustering of the positive events on the digital maps in Figure 4-5. This phenomenon can be explained by two characteristics of the system: 1) a non-homogeneity of SAMs formation on the sensor surface; and 2) the effect of attinebility. Next, we will discuss each of those contributions to the clustering observed in the digital maps (Figures 4-5 and Figure B-S5). SAMs are known to have defects that originate from imperfections in the arrangement of the molecules at the gold film. The gold film itself contains coverage imperfections that lead to grain boundaries.[43] These defects are attributed to misaligned and missing molecules in the assembly, agglomeration due to selfreacted molecules and island formations of SAMs separated by grain boundaries.[44,45] The idea that SAMs consists of a long range ordered arrays linked by S-Au bonding is an inaccurate assumption.[46] Other than grain boundaries, reported defects on COOH-SAMs are bilayer formation through hydrogen bonding, laying down "striped" phases, gauche defects (tangled chains) and non-covered areas (vacancies).[47–49] XPS measurements for different SAM preparations, that measured improperly bound thiol for studies of SAMs quality formation shows large variability on spots of the same sample.[47] The antibodies are covalently linked to the SAMs and these defects propagates to the distribution of antibody coverage on the surface of the sensor. Proper orientation of antibodies on the surface of the assay is critical for biosensor performance, alongside with good coverage.[50] Therefore, if the SAMs are not formed homogeneously, the antibody coverage on the surface would not be a perfect monolayer in the whole area of the assay. The defects on the COOH-SAMs suggest a patched formation of antibody coverage on the gold substrate. Additionally, the attinebility might play a role in this system. Attinebility refers to a localized change in the dissociation constant of clustered receptors on surfaces.[51] The antigen rebinds to proximal receptors after an unbinding event, without further decrease in localization entropy.[51,52] It was experimentally shown that the apparent dissociation constant is significantly lowered for additional receptors in proximity to DNA hybridization complexes bound to the sensor and that these conclusions can be extended to other interactions such as antibody-antigen.[53] This phenomena was documented for clustered carbohydrates on surfaces[54] and for DNA-functionalized gold nanoparticles[55,56] This effect was dubbed density-dependent cooperative binding since the affinity is higher if a ligand is concurrently bound to multiple adjacent targets.[52]

In summary, the defects on the SAMs layers, the patched antibody coverage and the attinebility effect could cause the clustering seen in Figure 4-5. However, as these effects play a role in all samples, the linearity of the assay is maintained, as long as there is enough number of measurements done to account for the variability in the system. When using a 50x objective, around 50 measurements are necessary to meet a tolerance of 5% relative standard deviation (RSD) for ERL-based immunoassay substrate.[17]

4.3.3 Digital Calibration Curves

Figure 4-7 shows calibration curves in saliva from 1.6 ng.mL^{-1} to 12.5 ng.mL^{-1}. Figure 4-7A shows the conventional way of data analysis, which relates SERS intensities to the S1-S2 spike protein concentration. Figure 4-7B applies the digital protocol to the same dataset. Figure 4-7A is shown superposed to a box plot showing the median, mean, the 25 to 75 percentile and the range within 1.5 IQR (interquartile range) for the SERS intensities for each concentration and the control. The full range of concentrations, 1.6 ng.mL^{-1} to 200.0 ng.mL^{-1} of S1-S2 spike protein, is shown in Figure B-S6 (Appendix B).

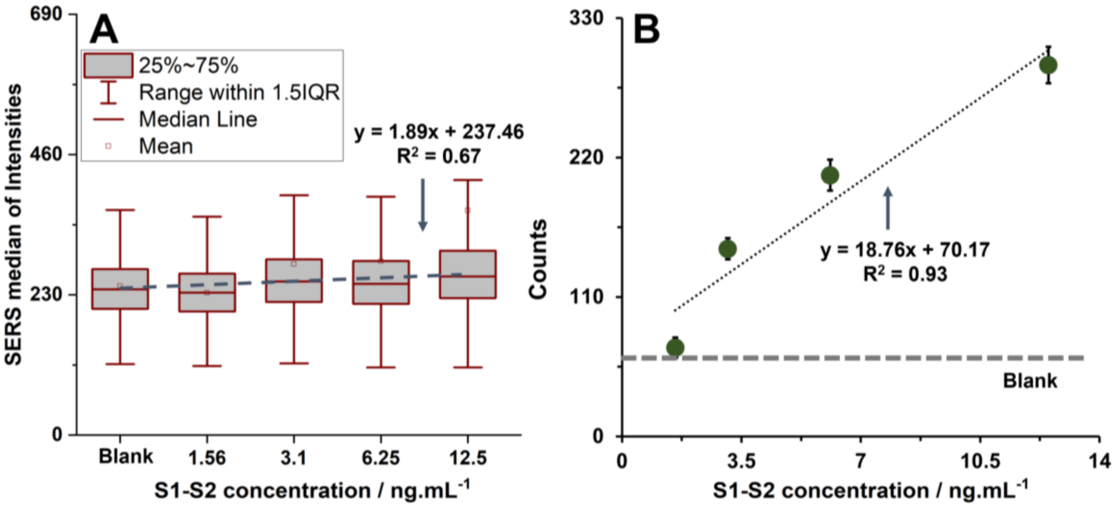

Figure 4-7. A) Calibration curve generated by the median of the intensities considering ` phenoxazine ring mode related to the concentration of the S1-S2 spike protein in saliva, superposed on a box plot with the range within 1.5 IQR shown. B) Calibration curve generated by the digital protocol, being counts (positive events) related to the concentration of the S1-S2 Spike Protein in saliva. In Figure B-S6, the box plot also shows the minimum and maximum of the SERS measurements for each S1-S2 spike protein concentration (the breaks in the y-axis were used to accommodate the representation of all variations in one plot). The box plot representation was chosen to show not only the large variation of the SERS intensities within the dataset but also the asymmetry in the distribution of SERS intensities.

The linearity of the relationship between the median of the SERS intensities and S1-S2 spike protein concentration, shown in Figure 4-7A, presented a R^2 of 0.67 The median of the intensities was chosen for the plot in Figure 4-7A instead of the mean, due to the nature of the lognormal distributed population for both assays (see Figure B-S8).[19] The linearity of the digital protocol for the same dataset (Figure 4-7B) was much better, reaching an R^2 of 0.93. The error bars in Figure 4-7B are the standard deviations of the counts in the maps. Figures 4-7A and 4-7B show that the digital approach decreased the variations and improved linearity. The effect of the improved linearity is even more dramatic in the experiments realized with PBS-10 and presented in the Appendix B file (Figure B-S7). Note that the range of linearity of the digital plots was smaller when in saliva (Figure 4-7B) than compared to PBS-10 (Figure B-S7B). Saliva is a complex fluid, with a library of proteins (102 identified), hormones, and antibodies.[57] Nonspecific binding, and therefore blocking of part of the available sites probably cause the assay to saturate at lower concentrations compared to a clean matrix such as PBS-10. However, the data in Figure 4-7B fits almost perfectly with the concentration in a log scale ($R^2 = 0.99$) that accounts for the slight curvature at higher concentrations in Figure 4-7B. The log concentration scale obviously also improves the linearity of the common (Figure 4-7A) SERS intensity calibration plots (to $R^2 = 0.77$). In any case, the digital procedure presents better performance than the common SERS intensity calibration method for the low concentration conditions explored here.

4.3.4 Summary of the Assay Performance

The digital assay in PBS-10 has a limit of quantification, LOQ, of 13.7 ng.mL^{-1} or 76.0 pM and a limit of detection, LOD, of 41.4 ng.mL^{-1} or 230.2 pM, within a 95% confidence level. The digital assay for saliva has LOQ of 19.0 ng.mL^{-1} or 105.7 pM and LOD of 6.3 ng.mL^{-1} or 34.9 pM, within a 95% confidence level. LOD was defined as the analyte concentration that produces a signal three times larger than the standard deviation and LOQ as 10 times the standard deviation of the blank.

4.4 Conclusion

Proof-of-concept assays for detection of SARS-CoV-2 spike protein S1-S2 subunit (S1-S2 Spike Protein) in PBS-10 and in saliva were described for a SERS-based digital protocol. The sensor was based on a gold covered glass that had SARS-CoV-2 (2019-nCoV) Spike S2 antibodies. The antigen, SARS-CoV-2 spike protein S1-S2 subunit was added to the sensor, followed by ERLs. The ERLs were modified gold nanoparticles that contained a Nile Blue (NB), a Raman reporter, and SARS-CoV-2 S1 antibodies. The sensors were mapped using line focus mapping, which allow the collection of an appreciable number of Raman measurements in minutes. A conventional data treatment was compared to a digital protocol for all datasets. The conventional data treatment was insufficient to generate calibration curves with a good linearity whereas the digital protocol was adequate. This is due to both the large variation in SERS intensities at lower surface concentrations of ERLs and the non-uniformity of hotspot intensity distributions.[18] The digital protocol is an effective and direct approach to analyze bioassays in the low concentration range (pM or less) that can be successfully applied to labeled SERS-based heterogenous immunoassays.

4.5 References

(1) Kahraman, M.; Mullen, E. R.; Korkmaz, A.; Wachsmann-Hogiu, S. Fundamentals and Applications of SERS-Based Bioanalytical Sensing. Nanophotonics 2017, 6 (5), 831–852.

(2) Cialla, D.; Pollok, S.; Steinbrücker, C.; Weber, K.; Popp, J. SERS-Based Detection of Biomolecules. Nanophotonics 2014, 3 (6), 383–411.

(3) Tzeng, Y.; Lin, B.-Y. Silver SERS Adenine Sensors with a Very Low Detection Limit. Biosensors (Basel) 2020, 10 (5), 53.

(4) Granger, J. H.; Granger, M. C.; Firpo, M. A.; Mulvihill, S. J.; Porter, M. D. Toward Development of a Surface-Enhanced Raman Scattering (SERS)-Based Cancer Diagnostic Immunoassay Panel. Analyst 2013, 138 (2), 410–416.

(5) Laing, S.; Gracie, K.; Faulds, K. Multiplex in Vitro Detection Using SERS. Chem. Soc. Rev. 2016, 45 (7), 1901–1918.

(6) Li, D.; Jiang, L.; Piper, J. A.; Maksymov, I. S.; Greentree, A. D.; Wang, E.; Wang, Y. Sensitive and Multiplexed SERS Nanotags for the Detection of Cytokines Secreted by Lymphoma. ACS Sens. 2019, 4 (9), 2507–2514.

(7) Navas-Moreno, M.; Mehrpouyan, M.; Chernenko, T.; Candas, D.; Fan, M.; Li, J. J.; Yan, M.; Chan, J. W. Nanoparticles for Live Cell Microscopy: A Surface-Enhanced Raman Scattering Perspective. Sci Rep 2017, 7 (1), 4471.

(8) Wang, Z.; Zong, S.; Wu, L.; Zhu, D.; Cui, Y. SERS-Activated Platforms for Immunoassay: Probes, Encoding Methods, and Applications. Chem. Rev. 2017, 117 (12), 7910–7963.

(9) Sharma, B.; Frontiera, R. R.; Henry, A.-I.; Ringe, E.; Van Duyne, R. P. SERS: Materials, Applications, and the Future. Materials Today 2012, 15 (1), 16–25.

(10) Mohammadi, M.; Antoine, D.; Vitt, M.; Dickie, J. M.; Sultana Jyoti, S.; Wall, J. G.; Johnson, P. A.; Wawrousek, K. E. A Fast, Ultrasensitive SERS Immunoassay to Detect SARS-CoV-2 in Saliva. Analytica Chimica Acta 2022, 1229, 340290.

(11) Rizzo, F. Optical Immunoassays Methods in Protein Analysis: An Overview. Chemosensors 2022, 10 (8), 326.

(12) Narayanan, R.; Lipert, R. J.; Porter, M. D. Cetyltrimethylammonium Bromide-Modified Spherical and Cube-Like Gold Nanoparticles as Extrinsic Raman Labels in Surface-Enhanced Raman Spectroscopy Based Heterogeneous Immunoassays. Anal. Chem. 2008, 80 (6), 2265–2271.

(13) Crawford, A. C.; Laurentius, L. B.; Mulvihill, T. S.; Granger, J. H.; Spencer, J. S.; Chatterjee, D.; Hanson, K. E.; Porter, M. D. Detection of the Tuberculosis Antigenic Marker Mannose-Capped Lipoarabinomannan in Pretreated Serum by Surface-Enhanced Raman Scattering. Analyst 2016, 142 (1), 186–196.

(14) Banaei, N.; Foley, A.; Houghton, J. M.; Sun, Y.; Kim, B. Multiplex Detection of Pancreatic Cancer Biomarkers Using a SERS-Based Immunoassay. Nanotechnology 2017, 28 (45), 455101.

(15) Wang, G.; Lipert, R. J.; Jain, M.; Kaur, S.; Chakraboty, S.; Torres, M. P.; Batra, S. K.; Brand, R. E.; Porter, M. D. Detection of the Potential Pancreatic Cancer Marker MUC4 in Serum Using Surface-Enhanced Raman Scattering. Anal. Chem. 2011, 83 (7), 2554–2561.

(16) Langer, J.; Jimenez de Aberasturi, D.; Aizpurua, J.; Alvarez-Puebla, R. A.; Auguié, B.; Baumberg, J. J.; Bazan, G. C.; Bell, S. E. J.; Boisen, A.; Brolo, A. G.; Choo, J.; Cialla-May, D.; Deckert, V.; Fabris, L.; Faulds, K.; García de Abajo, F. J.; Goodacre, R.; Graham, D.; Haes, A. J.; Haynes, C. L.; Huck, C.; Itoh, T.; Käll, M.; Kneipp, J.; Kotov, N. A.; Kuang, H.; Le Ru, E. C.; Lee, H. K.; Li, J.-F.; Ling, X. Y.; Maier, S. A.; Mayerhöfer, T.; Moskovits, M.; Murakoshi, K.; Nam, J.-M.; Nie, S.; Ozaki, Y.; Pastoriza-Santos, I.; Perez-Juste, J.; Popp, J.; Pucci, A.; Reich, S.; Ren, B.; Schatz, G. C.; Shegai, T.; Schlücker, S.; Tay, L.-L.; Thomas, K. G.; Tian, Z.-Q.; Van Duyne, R. P.; Vo-Dinh, T.; Wang, Y.; Willets, K. A.; Xu, C.; Xu, H.; Xu, Y.; Yamamoto, Y. S.; Zhao, B.; Liz-Marzán, L. M. Present and Future of Surface-Enhanced Raman Scattering. ACS Nano 2020, 14 (1), 28–117.

(17) Crawford, A. C.; Skuratovsky, A.; Porter, M. D. Sampling Error: Impact on the Quantitative Analysis of Nanoparticle-Based Surface-Enhanced Raman Scattering Immunoassays. Anal. Chem. 2016, 88 (12), 6515–6522.

(18) Fan, M.; Andrade, G. F. S.; Brolo, A. G. A Review on Recent Advances in the Applications of Surface-Enhanced Raman Scattering in Analytical Chemistry. Analytica Chimica Acta 2020, 1097, 1–29.

(19) Tuckmantel Bido, A.; Azarakhshi, A.; Brolo, A. G. Exploring Intensity Distributions and Sampling in SERS-Based Immunoassays. Anal. Chem. 2022, acs.analchem.2c02845.

(20) Serebrennikova, K. V.; Berlina, A. N.; Sotnikov, D. V.; Zherdev, A. V.; Dzantiev, B. B. Raman Scattering-Based Biosensing: New Prospects and Opportunities. Biosensors 2021, 11 (12), 512.

(21) Zhang, Y.; Noji, H. Digital Bioassays: Theory, Applications, and Perspectives. Anal. Chem. 2017, 89 (1), 92–101.

(22) de Albuquerque, C. D. L.; Sobral-Filho, R. G.; Poppi, R. J.; Brolo, A. G. Digital Protocol for Chemical Analysis at Ultralow Concentrations by Surface-Enhanced Raman Scattering. Anal. Chem. 2018, 90 (2), 1248–1254.

(23) Shim, J.-E.; Kim, Y. J.; Choe, J.-H.; Lee, T. G.; You, E.-A. Single-Nanoparticle-Based Digital SERS Sensing Platform for the Accurate Quantitative Detection of SARS-CoV-2. ACS Appl. Mater. Interfaces 2022, 14 (34), 38459–38470.

(24) Chuong, T. T.; Pallaoro, A.; Chaves, C. A.; Li, Z.; Lee, J.; Eisenstein, M.; Stucky, G. D.; Moskovits, M.; Soh, H. T. Dual-Reporter SERS-Based Biomolecular Assay with Reduced False-Positive Signals. Proceedings of the National Academy of Sciences 2017, 114 (34), 9056–9061.

(25) Shaw, C. P.; Fan, M.; Lane, C.; Barry, G.; Jirasek, A. I.; Brolo, A. G. Statistical Correlation Between SERS Intensity and Nanoparticle Cluster Size. J. Phys. Chem. C 2013, 117 (32), 16596–16605.

(26) Qian, X.; Peng, X.-H.; Ansari, D. O.; Yin-Goen, Q.; Chen, G. Z.; Shin, D. M.; Yang, L.; Young, A. N.; Wang, M. D.; Nie, S. In Vivo Tumor Targeting and Spectroscopic Detection with Surface-Enhanced Raman Nanoparticle Tags. Nat Biotechnol 2008, 26 (1), 83–90.

(27) Eck, W.; Craig, G.; Sigdel, A.; Ritter, G.; Old, L. J.; Tang, L.; Brennan, M. F.; Allen, P. J.; Mason, M. D. PEGylated Gold Nanoparticles Conjugated to Monoclonal F19 Antibodies as Targeted Labeling Agents for Human Pancreatic Carcinoma Tissue. ACS Nano 2008, 2 (11), 2263–2272.

(28) Ruiz, G.; Tripathi, K.; Okyem, S.; Driskell, J. D. PH Impacts the Orientation of Antibody Adsorbed onto Gold Nanoparticles. Bioconjugate Chem. 2019, 30 (4), 1182–1191.

(29) Thompson, P.; Bovolato, A. L. de C.; Ibáñez-Redín, G.; Brolo, A. G. Quantification of a COVID-19 Antibody Assay Using a Lateral Flow Test and a Cell Phone. Chemosensors 2022, 10 (7), 234.

(30) Holzer, B.; Manoli, K.; Ditaranto, N.; Macchia, E.; Tiwari, A.; Franco, C. D.; Scamarcio, G.; Palazzo, G.; Torsi, L. Characterization of Covalently Bound Anti-Human Immunoglobulins on Self-Assembled Monolayer Modified Gold Electrodes. Advanced Biosystems 2017, 1 (11), 1700055.

(31) Lee, J. W.; Sim, S. J.; Cho, S. M.; Lee, J. Characterization of a Self-Assembled Monolayer of Thiol on a Gold Surface and the Fabrication of a Biosensor Chip Based on Surface Plasmon Resonance for Detecting Anti-GAD Antibody. Biosensors and Bioelectronics 2005, 20 (7), 1422–1427.

(32) Wickramathilaka, M. P.; Tao, B. Y. Characterization of Covalent Crosslinking Strategies for Synthesizing DNA-Based Bioconjugates. Journal of Biological Engineering 2019, 13 (1), 63.

(33) Liberelle, B.; Boucher, C.; Chen, J.; Jolicoeur, M.; Durocher, Y.; De Crescenzo, G. Impact of Epidermal Growth Factor Tethering Strategy on Cellular Response. Bioconjugate Chem. 2010, 21 (12), 2257–2266.

(34) Wang, W.; Wei, Q.-Q.; Wang, J.; Wang, B.-C.; Zhang, S.; Yuan, Z. Role of Thiol-Containing Polyethylene Glycol (Thiol-PEG) in the Modification Process of Gold

Nanoparticles (AuNPs): Stabilizer or Coagulant? Journal of Colloid and Interface Science 2013, 404, 223–229.

(35) Zhang, G.; Yang, Z.; Lu, W.; Zhang, R.; Huang, Q.; Tian, M.; Li, L.; Liang, D.; Li, C. Influence of Anchoring Ligands and Particle Size on the Colloidal Stability and in Vivo Biodistribution of Polyethylene Glycol-Coated Gold Nanoparticles in Tumor-Xenografted Mice. Biomaterials 2009, 30 (10), 1928–1936.

(36) Zhang, Z.; Lin, M. Fast Loading of PEG–SH on CTAB-Protected Gold Nanorods. RSC Adv. 2014, 4 (34), 17760–17767.

(37) Tam, J. O.; de Puig, H.; Yen, C.; Bosch, I.; Gómez-Márquez, J.; Clavet, C.; Hamad-Schifferli, K.; Gehrke, L. A Comparison of Nanoparticle-Antibody Conjugation Strategies in Sandwich Immunoassays. J Immunoassay Immunochem 2017, 38 (4), 355–377.

(38) Kim, C.; Galloway, J. F.; Lee, K. H.; Searson, P. C. Universal Antibody Conjugation to Nanoparticles Using the Fcγ Receptor I (FcγRI): Quantitative Profiling Of Membrane Biomarkers. Bioconjugate Chem. 2014, 25 (10), 1893–1901.

(39) Michalke, B.; Rossbach, B.; Göen, T.; Schäferhenrich, A.; Scherer, G. Saliva as a Matrix for Human Biomonitoring in Occupational and Environmental Medicine. Int Arch Occup Environ Health 2015, 88 (1), 1–44.

(40) Griffin, S. M.; Converse, R. R.; Leon, J. S.; Wade, T. J.; Jiang, X.; Moe, C. L.; Egorov, A. I. Application of Salivary Antibody Immunoassays for the Detection of Incident Infections with Norwalk Virus in a Group of Volunteers. J Immunol Methods 2015, 424, 53–63.

(41) Schulze, G.; Jirasek, A.; Yu, M. M. L.; Lim, A.; Turner, R. F. B.; Blades, M. W. Investigation of Selected Baseline Removal Techniques as Candidates for Automated Implementation. Appl Spectrosc 2005, 59 (5), 545–574.

(42) Granger, J. H.; Schlotter, N. E.; Crawford, A. C.; Porter, M. D. Prospects for Point-of-Care Pathogen Diagnostics Using Surface-Enhanced Raman Scattering (SERS). Chem. Soc. Rev. 2016, 45 (14), 3865–3882.

(43) Losic, D.; Shapter, J. G.; Gooding, J. J. Influence of Surface Topography on Alkanethiol SAMs Assembled from Solution and by Microcontact Printing. Langmuir 2001, 17 (11), 3307–3316.

(44) Hinckley, A. P.; Muscat, A. J. Detecting and Removing Defects in Organosilane Self-Assembled Monolayers. Langmuir 2020, 36 (10), 2563–2573.

(45) Jalali, H.; Gates, B. D. Monitoring and Mapping Imperfections in Silane-Based Self-Assembled Monolayers by Chemical Amplification. Langmuir 2009, 25 (16), 9078–9084.

(46) Guo, Q.; Li, F. Self-Assembled Alkanethiol Monolayers on Gold Surfaces: Resolving the Complex Structure at the Interface by STM. Phys. Chem. Chem. Phys. 2014, 16 (36), 19074–19090.

(47) Brightbill, E. L.; Hitchcock, B.; Tsai, M.-Y.; Verga, A.; Vogel, E. M. Preblocking Procedure to Mitigate Nonselective Protein Adsorption for Carboxyl-SAMs Used in Biosensing. The Journal of Physical Chemistry C 2019.

(48) Schreiber, F. Structure and Growth of Self-Assembling Monolayers. Progress in Surface Science 2000, 65 (5–8), 151–257.

(49) Love, J. C.; Estroff, L. A.; Kriebel, J. K.; Nuzzo, R. G.; Whitesides, G. M. Self-Assembled Monolayers of Thiolates on Metals as a Form of Nanotechnology. Chem. Rev. 2005, 105 (4), 1103–1170.

(50) Chen, S.; Liu, L.; Zhou, J.; Jiang, S. Controlling Antibody Orientation on Charged Self-Assembled Monolayers. Langmuir 2003, 19 (7), 2859–2864.

(51) Frutiger, A.; Tanno, A.; Hwu, S.; Tiefenauer, R. F.; Vörös, J.; Nakatsuka, N. Nonspecific Binding—Fundamental Concepts and Consequences for Biosensing Applications. Chem. Rev. 2021, 121 (13), 8095–8160.

(52) Ozer, A.; White, B. S.; Lis, J. T.; Shalloway, D. Density-Dependent Cooperative Non-Specific Binding in Solid-Phase SELEX Affinity Selection. Nucleic Acids Res 2013, 41 (14), 7167–7175.

(53) Sobek, J.; Rehrauer, H.; Schauer, S.; Fischer, D.; Patrignani, A.; Landgraf, S.; Korlach, J.; Schlapbach, R. Single-Molecule DNA Hybridisation Studied by Using a Modified DNA Sequencer: A Comparison with Surface Plasmon Resonance Data. Methods Appl. Fluoresc. 2016, 4 (1), 015002.

(54) Horan, N.; Yan, L.; Isobe, H.; Whitesides, G. M.; Kahne, D. Nonstatistical Binding of a Protein to Clustered Carbohydrates. Proceedings of the National Academy of Sciences 1999, 96 (21), 11782–11786.

(55) Hwu, S.; Blickenstorfer, Y.; Ihle, S. J.; Garzuel, M.; Forró, C.; Schmidheini, L.; Demkó, L.; Vörös, J. Theoretical and Experimental Investigation of Ligand-Induced Particle–Particle Interactions. J. Phys. Chem. C 2020, 124 (2), 1566–1574.

(56) Hwu, S.; Garzuel, M.; Forró, C.; Ihle, S. J.; Reichmuth, A. M.; Kurdzesau, F.; Vörös, J. An Analytical Method to Control the Surface Density and Stability of DNA-Gold

Nanoparticles for an Optimized Biosensor. Colloids and Surfaces B: Biointerfaces 2020, 187, 110650.

(57) Tiwari, M. Science behind Human Saliva. J Nat Sci Biol Med 2011, 2 (1), 53–58.

Chapter 5: Detection of SARS-CoV-2 in Saliva by a Low-cost LSPR-based Sensor

This chapter is based on the work: "Detection of SARS-CoV-2 in Saliva by a Low-cost LSPR-based Sensor" by Ariadne Tuckmantel Bido, Katherine J.I. Ember, Dominique Trudel, Madeleine Duran, Frederic Leblond and Alexandre G. Brolo, ready to be submitted.

ATB developed the sensors and performed all the measurements and data analysis. KJIB tested the sensors in patient's saliva at Centre hospitalier de l'Université de Montréal (CHUM) and sent them back to UVic for measurements. Madeleine Duran was responsible for patient's saliva collection. ATB wrote the first draft of the manuscript and all authors contributed with editing and suggestions.

The SARS-CoV-2 pandemic started more than 3 years ago, but the containment of the spread is still a challenge. Screening is imperative for informed decision making by government authorities to contain the spread of the virus locally. The access to screening tests is disproportional, due to the lack of access to reagents, equipment, finances or because of supply chain disruptions. Low and middle-income countries have especially suffered with the lack of these resources. Here, we propose a low cost and easily constructed sensor based on localized surface plasmon resonance, or LSPR, for the screening of SARS-CoV-2. The sensor was constructed in two modalities: 1) viral detection in saliva and 2) antibody against COVID in saliva. Saliva collected from 18

patients were tested. Both sensors successfully classified all COVID positive patients (among hospitalized and non-hospitalized). From the COVID negative patients 7/8 patients were correctly classified. For both sensors, sensitivity was determined as 100% (95% CI 79.5-100) and specificity as 87.5% (95% CI 80.5-100). The reagents and equipment used for the construction and deployment of this sensor are ubiquitous and low-cost. This sensor technology can then add to the potential solution for challenges related to screening tests in underserved communities.

5.1 Introduction

The severe acute respiratory syndrome (SARS)-coronavirus 2 (CoV-2) is spreading worldwide since the late 2019, and it has already caused more than 6.7 million deaths as of January 13, 2023.[1] There are reported increase in depression, anxiety, loneliness[2,3], food insecurity and job losses due to pandemic. The direct medical cost (Monte Carlo simulation, 20% infection rate) was estimated to be of 163.4 billion in the United States, with projections of the total cost in the order of $16 trillion.[4,5] The key preventative measure to deal with the ongoing SARS-CoV-2 is the deployment of vaccines. Highly efficient vaccines for the original virus were produced within a year, with about 95% efficacy following two doses.[6] However, the availability of screening tests is imperative to control and contain the spread of the disease. The induction of sterilizing immunity, i.e. elimination of the virus before it starts to replicate, is not an attainable goal for this disease.[7] SARS-CoV-2 has a high mutation rate due to a lack of a mismatch repair mechanism in the virus.[8,9] Mutations can make the virus more contagious and able to escape the natural and vaccine-induced immunity.[8] These mutations caused the transmission of new variants (α, β, γ, δ) waves.[7] Currently, the most common variant amongst the population is the omicron. The vaccine against the wild-type virus offers a strong protection from severe disease compared to non-vaccinated individuals, but the new mutant prevents the vaccine to induce a level of immunity that stops the spread.[7] Additionally, tests performed in asymptomatic vaccinated patients (at least one dose received) with an mRNA vaccine showed that 1.4% of this population was positive for the virus.[10] Mass testing was appointed as the most significant measure to decrease SARS-CoV-2 infection rates.[12] The wide application of rapid tests enables the monitoring of viral spread in a population and provide tools for policy makers to make informed decisions regarding spread containment. However, the access to screening tests is still a challenge, specifically in low-middle-income countries with turbulent socio-economic backgrounds. Most of the tests performed during the pandemic were in high income countries. For comparison, the USA tested the equivalent of 192% of the population in test numbers, whilst Brazil tested 27% and Nigeria only 1%.[13] One of the causes for this disparity of numbers is the lack of reagents and equipment due either to the lack of affordability or to supply chain disruptions.[14] There is an urgency for development of more options of screening tests that are of simple construction using widely available reagents and that can be easily deployed.

Reverse transcription polymerase chain reaction (RT-PCR) assays are the gold-standard for SARS-CoV-2 testing but require trained staff and sophisticated laboratory facilities. Lateral flow assays (LFAs) have been developed as a rapid mass screening alternative.[15] Antigen LFAs are notable for their ease of use, high specificity, and quick results (less than 30 min). However, concerns have arisen about the lower sensitivity, especially in asymptomatic individuals.[15,16] An evaluation of five LFA tests for the detection of SARS-CoV-2 nucleocapsid antigen reported 100% of specificity for 4/5 tests and sensitivity ranging from 64 (95% CI 53–73) to 76% (95% CI 65–85).[17]

There is high demand for testing asymptomatic individuals that have had close contact with COVID positive persons. In the general populations, among COVID positive individuals, 40.5% are asymptomatic.[18] Additionally, saliva is deemed as the ideal fluid for SARS-CoV-2 monitoring, since it decreases the exposition of health care workers during collection and can be deployed as self-collection.[13]

The sensor described in this paper was built on well plates and the readout was performed in an absorbance plate reader; both are ubiquitous in testing centers, companies, and universities. The well plate format was chosen here to allow for high throughput, but the principles of this sensor can be easily translated to individual strips for simpler collection.[19] The reagents required to make the silver nanoparticle (AgNPs) are common and low cost. Additionally, the synthesis is simple and yields a large volume (~100 mL), that is enough to cover more than 3,360 wells. The sensor is based on saliva instead of nasopharyngeal swabs, which are harder to collect, particularly in the case of infants. Therefore, we believe this alternative method of screening has the potential to be deployed in underserved communities as an additional tool in the fight against SARS-CoV-2 or for future pandemic preparedness. This sensor can be altered to detect other infectious diseases, by swapping the element of recognition adhered to the sensing film.

5.2 Materials and Methods

5.2.1 Materials

Flat-bottomed assay plates with 384 wells and a lid were purchased from Corning Incorporated. They were culture-treated, white with a clear bottom, and made of low flange polystyrene. Polyethyleneimine 50 wt. % solution in water (PEI), Mn 1200/Mw 1300 was purchased from Sigma-Aldrich. SARS-CoV-2 (2019-nCoV) Spike S2 Antibody, SARS-CoV-2 (2019-nCoV) Spike S1 + S2 ECD-His Recombinant Protein and Influenza A H7N9 (A/Shanghai/1/2013) Hemagglutinin / HA Protein (His Tag) were purchased from Sino Biological. Optical adhesive film covers were bought from Fisher Scientific. Silver nitrate and hydroxylamine hydrochloride were purchased from Sigma-Aldrich. Phosphate buffered saline (PBS) pH 7.2 (1X) was purchased from Gibco. Anhydrous ethyl alcohol was purchased from Commercial Alcohols. Sodium azide, bovine serum albumin (BSA), 3-mercaptopropionic acid (3 MPA), 11-mercaptoundecanoic acid (11 MUA) and ethanolamine-hydrochloride were purchased from Sigma-Aldrich. Polyoxyethylene-20 (tween 20) were purchased from Biotech. N-ethyl-N'-(3-diethylaminopropyl) carbodiimide (EDC) and sulfo-(N-hydroxysulfosuccinimide sodium salt (sulfo NHS) were purchased from ProteoChem™; HS-PEG-COOH, MW 3000 and methoxy -PEG-thiol, MW 5000 were purchased from Rapp Polymere. Dimethyl sulfoxide (DMSO), HPLC grade was purchased from Sigma-Aldrich. Triton X-100 was purchased from Fisher Bioreagents. Ultrapure water was collected in a Nanopure Diamond™, 18.2 MΩ.cm at room temperature, and used in all solution preparations and washing steps. An accuSpin

Micro 17 (Fisher Scientific,Waltham, Massachusetts, United States) was used for centrifugation.

5.2.2 Synthesis of Silver Nanoparticles (AgNPs)

Silver nanoparticles (AgNPs) were prepared according to Leopold and Lendl with a few modifications.[20] 90 mL of a 3.33 mM sodium hydroxide solution was added to a beaker and 1 mL of a 150 mM hydroxylamine hydrochloride solution was added whilst stirring (700 rpm/min). Then, 10 mL of a 10 mM silver nitrate solution was added dropwise at a fast pace using a 10 mL-serological pipette. The mixture was left to stir for 15 min, resulting in a dark yellow colored solution. The synthesized AgNPs were then stored in a fridge in a glass vial for further use (4 °C). This process yielded mostly spherical AgNP with estimated average size of 42.9 ± 17.3 nm. The size was determined by averaging the diameter of 587 AgNPs in transmission electron microscopy (TEM) images using Image J software. The estimated concentration of the colloid is 1.7 x 10^{10} AgNPs/mL, considering the average size of the AgNPs measured in TEM and the amount of silver added to the reaction.

5.2.3 Sensing Film Preparation on Well Plates

In a 384 well assay plate, 25 µL of a 1% (m/v) PEI solution in water was added to each of the wells. After 45 minutes, the wells were washed with water at least ten times. The water was added with a squeeze bottle and tapping the inverted plate into a paper towel, in a similar manner as in an enzyme linked immunosorbent assay (ELISA) wash.[21,22] Then, 30 μL of the AgNPs were added to each of the wells and the plate was left overnight in the fridge. The wells were then washed with water, following the same procedure as before. The wells modified with Ag NPs were ready for immediate antibody adherence, but they could also be stored in the fridge for later modification. PEI was used as an attachment promoter of the AgNPs to the well plate plastic. PEI has a high density of amino groups that when protonated interact with the negatively charged plastic surface and with the negatively charged AgNPs.[23] The wells covered with the silver nanoparticles were a visually homogenous dark yellow color. These wells must be kept saturated with liquid, otherwise the sensing film degrades. The plate was measured using the Cytation 5 Cell Imaging Multimode Reader, (Biotek, Winooski, Vermont, United States). Measurements were done in absorption mode, 300 to 600 nm at 1 nm step, with 30 μL of PBS-10 (PBS diluted 10X with water) in each well. All measurements in Cytation 5 used the same parameters throughout the assay. The measurements were consistent well-to-well. Films were formed in 80 wells and measured with 30 μL of PBS-10 in a Cytation 5. The average maximum of the extinction spectra from the 80 plates was 1.00 ± 0.02 arbitrary units (a.u). The individual readings were then normalized, and the peak portion (above 0.75 normalized a.u.) was fit to a polynomial of order 6 (see 1.8 Data Processing). The peak maximum of each well was found by solving the roots for the derivative of the polynomial fit using Matlab (MathWorks, Natick, Massachusetts, United States). The average of excitation maximum of the 80 wells were determined to be 397.6 ± 0.1 nm, which is consistent with AgNPs of ~ 40 nm.[24]. A photo of a plate with its wells covered with the AgNPs sensing film is presented as Appendix C, Figure C-S1.

5.2.4 Conjugation of the Detection Element to the Sensing Films

Two detection elements were conjugated to the sensing films: SARS-CoV-2 (2019-nCoV) Spike S2 Antibody, dubbed Spike S2 Ab and SARS-CoV-2 (2019-nCoV) Spike S1 + S2 ECD-His Recombinant Protein, dubbed S1+S2 protein. The former is an antibody that recognizes the virus' spike protein, and the latter is a recombinant protein that recognizes SARS-CoV-2 antibodies. The conjugation of these elements was mediated by self-assembled monolayers (SAMs). A thiol moiety present in both 3-mercaptopropionic acid (3MPA) and 11-mercaptoundecanoic acid (11 MUA) spontaneously binds to the silver sensing film via strong covalent metal-thiol bonds.[25] The SAMs formation was based on a protocol by Holzer et al.[26] 30 µL of a mixture of 3 MPA and 11 MUA in ethanol at 10×10^{-3} M in 10:1 volume ratio was added to each well and left in the fridge overnight. The contents of the wells were then aspirated using a micropipette and the wells are washed three times by adding 30 µL of PBS-10 and tapping the inverted plate into a paper towel. 30 µL of PBS-10 was added to each well and the plate was measured using a Cytation 5 reader. Next, 30 µL of a 0.2 M EDC / 0.05 M sulfo-NHS mixture was added to each well plate and left to react for 2 hours at room temperature. The wells were washed three times by rinsing with 30 µL of water and tapping the inverted plate onto paper towels. 15 µL of the recognition element at 50 µg/mL in PBS-10 was then added to the wells. The conjugation reaction was allowed to occur for 2.5 hours in an incubator at 25-30 °C. Both SARS-CoV-2 (2019-nCoV) Spike S2 Antibody (Spike S2 Ab) and the SARS-CoV-2 (2019-nCoV) Spike S1 + S2 ECD-His Recombinant Protein (S1+S2 protein) contain primary amines that form an amide bond with the activated carboxylic terminal ends of the

SAMs.[27–29] The wells were washed three times with 30 μL of PBS-10 and tapping the inverted plate into paper towels. Next, 30 μL of a 1M ethanolamine solution was added to the wells to deactivate unreacted esters, and left incubating for 1 hour.[30] The wells were subsequently washed three times with 30 μL PBS-10 as previously described and the plate was measured in an absorbance plate reader. Finally, the sensing films were blocked with BSA and DMSO. 30 μL of a 0.5% BSA (m/v) and 0.1% DMSO (v/v) in PBS-10 solution was added to each well for 1 hour at room temperature. BSA is used to block non-specific binding of proteins and a small amount of DMSO covers any exposed silver in the sensing film. [31–33] The wells were washed again three times with 30 μL PBS-10. The wells were filled with 30 μL PBS-10 and stored in the fridge for later use. The sensors are formed with 4 layers. Figure C-S2 shows a depiction of the layers. The first layer (1) is the AgNP film formed on the plastic well plates, the second layer (2) is the SAMs (3MPA and 11 MUA), the third layer (3) is the detection element, being either the Spike S2 Ab or S1+S2 protein. Lastly the fourth layer (4) is the blocking agent (BSA and DMSO). The fourth layer is not constructed on top of the third layer, but it is intertwined with the detection elements and the AgNP film. The fifth layer (5) depicts the analyte interacting with the detection element, being either the SARS-CoV-2 virus interacting with the Spike S2 Ab or the SARS-CoV-2 Ab interacting with the S1-S2 protein. The optical characteristics of the wells were measured after each layering step (1-4), showing a red shift of the extinction maxima after each step, as expected. However, only the peak shift of the full assembled sensor measured before and after exposure to the saliva is needed for detection/screening. The sensors were constructed at University of Victoria and shipped to Montreal for testing at the Centre hospitalier de l'Université de Montréal (CHUM). The wells of the plate were fully covered (around 105 μL) with PBS-10 and then isolated with an optical adhesive film cover for mailing. This guaranteed that the sensing film was in contact with the buffer solution during transport even when the package was not in an upright position.

5.2.5 Sample Collection and Processing

For the sensor development and optimization, standard samples were generated from self-collected saliva that were then spiked with analyte. The saliva was collected via the passive drool protocol, where unstimulated saliva is collected by dripping or gently spiting in a container until filling a specific volume.[34–37] The saliva sample donors washed their mouth three times with water and placed a 15 mL Falcon tube to mouth, letting the saliva flow out of the back salivary glands into the tube. 2.5 mL of saliva was collected and to that, 2.5 mL of PBS-10 was added. The Falcon tube was then gently vortexed. Aliquots were centrifuged at 6g for 20 min in an accuSpin Micro 17, at room temperature to remove any debris and the supernatants were frozen for later use. Aliquots were thawed and spiked with the analytes (either Spike S2 Ab or S1+S2 protein) to be used in the sensor. Blank and control experiments were run using saliva and with Influenza A H7N9 (A/Shanghai/1/2013) Hemagglutinin / HA Protein (His Tag), respectively. An example of an assay run for the controls and the standard samples are shown in the Appendix C, Figure C-S3.

5.2.6 Testing with Patient Samples

Patient samples, both positive and negative for SARS-CoV-2, were collected at the Pointe-Saint-Charles testing clinic in Montreal and from patients hospitalized due to SARS-CoV-2 at the Centre hospitalier de l'Université de Montréal (CHUM). Participants provided informed consent, and the project was approved by the CHUM Research Ethics Board (project number: 20.133). [38] The saliva collection was conducted as above described, at a minimum of 1.5 mL. [38] Tubes where then stored in a fridge at 4 °C and handled in a biosafety containment level 2 (BSL2) when manipulated. Samples collected at Pointe-Saint-Charles testing clinic were classified as "COVID positive outpatient" and "COVID negative" with SARS-CoV-2 based on PCR tests from nasopharyngeal swabs performed at the same time as the saliva collection. The hospitalized patients were classified as "COVID positive hospitalized", the infection was confirmed by a PCR test at admission. 16 patient samples were available to test the LSPR sensors, being 6 from "COVID positive hospitalized", 8 "COVID negative" and 2 "COVID positive outpatient". The samples were centrifuged at 4000 rpm for 30 minutes at 4°C in 1 mL aliquots. The supernatant was pipetted into a cryotube, mixed, and aliquoted into five separate 1.8 ml cryotubes. These aliquots were thawed at room temperature for 45 minutes before application to the wells. The pellet was retained and stored at -80 °C.

The plates were constructed as described above at University of Victoria and shipped to CHUM for the samples testing. The sensors were stored for a year in a fridge at 8 °C before use on the samples. At CHUM, the samples were thawed and diluted with PBS-10 two times and vortexed. To each well, 30 μL of the diluted saliva was added and left incubating at room temperature for 2 hours. The saliva was aspirated out of the wells and then 50 μL of a Triton X-100 0.5% (v/v) in PBS-10 was added to each well for virus inactivation, for 1 hour. [39] Next, the wells were washed with 50 μL of PBS-10, 5X as previously described. The wells were fully covered with PBS-10 and covered with an optical adhesive film covers for transportation. Finally, the wells were emptied, followed by the addition of 30 μL of PBS-10 to each one. The optical measurements were conducted with an absorbance plate reader at the CAMTEC BioCore Facility at the University of Victoria. The measurements were done after three weeks of the patient's samples exposure. The sensors were kept on a fridge at 8 °C.

5.2.7 Sensor Principle

The working principle of the sensor method is depicted in Figure 5-1. The sensing surface was built on top of a AgNP film modified with the specific antibody. The sensor was constructed in plastic well plates to allow for high throughput. The sensor response is based on the localized surface plasmon resonance (LSPR) principle. The maximum of the extinction spectra from each well was assessed before and after the exposure to the saliva samples of the patients. The magnitudes of the shifts of the main LSPR peak were used to classify the patients as "COVID positive" or "COVID negative". Figure 5-1A depicts an example of result obtained from a saliva sample of a healthy patient. Notice that no LSPR shift was observed in this case. Figure 5-1B depicts an example of extinction curves before and after exposure to the saliva of a COVID positive patient. Changes in the local refractive index, caused by the interaction of the recognition element immobilized at the surface with the target analyte in the saliva sample, generated a change in the plasmon frequency of the

AgNPs.[40] Large red shifts denote a strong change in refractive index which can be correlated to a larger amount of the analyte of interest binding to the target at the surface.

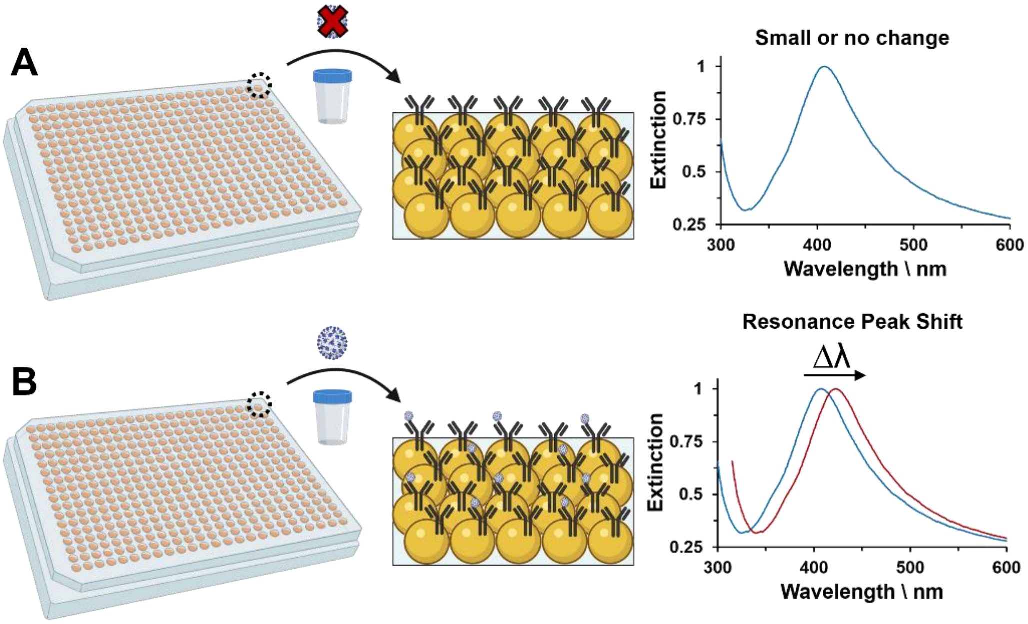

Figure 5-1. Sensor principle. A saliva sample is added to a well for SARS-Cov-2 screening. A) Saliva does not contain the virus, and there is no significant change in the extinction spectrum maxima. B) Saliva contains the virus, and there is a significant change in the extinction spectrum maxima.

5.2.8 Data Processing

The extinction spectra from each well were measured before and after exposure to the saliva samples. The individual readings were normalized, and the peak portion (above 0.75 normalized a.u.) was fit to a polynomial of order 6. The peak maxima were found by solving the roots for the derivative of the polynomial fit using Matlab. The LSPR peak values were recorded before and after exposure to the saliva samples. Triplicate measurements were done for each sample and the standard deviation of the three measurements were determined to be the error of the peak shift (LSPR peak position after exposure to the saliva sample – LSPR peak position before exposure to the saliva sample) for each measurement.

5.2.9 Instrumentation

A plate reader operating in absorbance mode, Biotek Cytation 5 (Agilent), was used to measure the extinction (UV-Vis) after each stage of modification and testing. The AgNPs were characterized by dynamic light scattering (DLS) and ζ-potential in an Anton Paar LiteSizer 500 (Anton Paar, Ashland, Virginia,United States), to determine the hydrodynamic radius (DLS) and surface charge (ζ-potential). The size and concentration of the AgNPs were estimated based on TEM images taken using a JEOL 1011 transmission electron microscope (JEOL USA Inc, Peabody, MA, United States). A PAL-1 digital hand-held refractometer (Atago, ltabashi-ku, Tokyo, Japan) was used to determine the refractive index of ethanol/water solutions used for film sensitivity determination.

5.3 Results and Discussion

5.3.1 AgNPs Characterization

Silver nanoparticles were generated in a reproducible manner, and characterized using UV-vis spectroscopy, TEM and dynamic light scattering (DLS). Figure 5-2A, 5-2B and 5-2C presents a UV-Vis spectrum with an insert of a TEM image section, a DLS and ζ- potential measurement for the AgNPs used to construct the sensing films. TEM images were analyzed using Image J software of 587 particles for size determination. The particles had a mean size of 42.9 ± 17.3 nm. The UV-Vis spectral maximum, taken in triplicate was at 409.3 ± 0.1 nm. The typical extinction peak for 40 nm silver nanospheres is located around 400 nm and has a characteristic yellow color.[24] There are two populations on the silver colloid, the main population have an average hydrodynamic radius of 62.2 ± 0.4 nm and a small seed population with an average hydrodynamic radius of 5.7 ± 0.5 nm. The average hydrodynamic radius of the particles, measured in duplicates by DLS, was 54.3 ± 1.6 nm. The ζ- potential, taken in triplicate, was determined to be 34.3 ± 0.4 mV. This suggests that the nanoparticles have high stability, as nanoparticles with zeta potential above +30 mV have been demonstrated to be highly stable.[41] A representative example of the LSPR peak shift measured after each layering is shown as Appendix C, Figure C-S4. Each stage of layering (Figure C-S3) is monitored for quality control, but for the classification of the samples, the difference is taken from before and after saliva exposure.

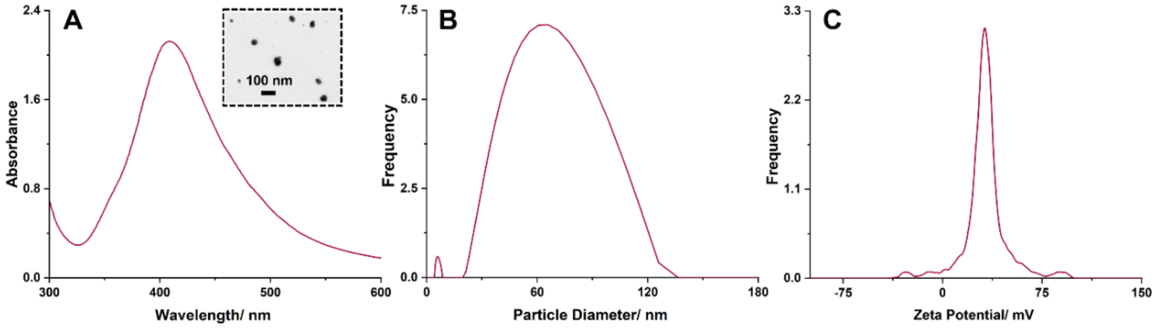

Figure 5-2. A) UV-Vis and TEM image, B) Dynamic light scattering (DLS), C) ζ-potential for the AgNPs used to construct the Ag film for the assay.

5.3.2 Sensing Film Sensitivity

The refractive index sensitivity of the films was determined by measuring the extinction of the silver nanoparticle film in 11 distinct ethanol/water solutions with variable compositions, from 0:10 (v/v) to 10:0 (v/v). Each solution had its refractive index measured (n) independently using a refractometer and the maxima of the extinction spectra was determined as explained in data processing in Materials and Methods. Figure C-S5 shows the LSPR maxima plotted in relation to the measured refractive index for the solutions. The refractive index sensitivity was determined to be 105.6 nm per refractive index unit (nm/RIU) in the AgNP film.

5.3.2 Virus Detection

Figure 5-3 shows the results for the patient samples for sensors with Spike S2 Ab as the recognition element. These sensors test for the presence of the virus in saliva. The plate wells were tested before and after contact with the patient’s saliva, in a plate reader (Biotek Cytation 5). The shifts were obtained after data processing. Each extinction maximum shift was calculated from triplicate measurements conducted in three separate wells for each sample, excluding patient 8 that was conducted in duplicate. Patients 1 to 6 are classified as “COVID positive hospitalized” and are represented as columns with a diagonal downward stripe pattern, patients 7 and 8 are classified as “COVID positive outpatient” and are represented as columns with a diagonal upward stripe pattern, patients 9 to 16 are classified as “COVID negative” and are represented as columns with a checkerboard pattern. Column 17 is a blank, represented as a green column. The blank (negative control) was generated by following all the procedures but not adding saliva to the well. Notice that the blank has a large negative shift, and some samples of COVID negative patients have a small negative shift. We believe the negative shift is due to the use of Triton X-100 for deactivation of the virus on the plates. Triton X-100 disrupts the lipid membrane of enveloped viruses and is employed in inactivation protocols for SARS-CoV-2.[39,42] Triton X-100 is a nonionic surfactant that has demonstrated low impact on antigen-antibody binding.[43] However, Triton X-100 complexes with BSA which was used as a blocker in this assay.[44,45] It is probable that some of the BSA is stripped with the relatively high concentration of Triton X-100 added to the assay, causing a negative shift to the blank and to samples that have no virus. The small but positive shifts for most COVID negative samples are probably due to proteins on the saliva that interact nonspecifically to the sensor, but this shift is smaller than when the positive samples containing the virus interact with the antibodies.

A large positive shift (> 0.7 nm) was observed for patients 1 to 6, “COVID positive hospitalized”. For patients 7 and 8, “COVID positive outpatient”, a medium size shift (> 0.3 nm) was observed. The patients’ saliva contains a high enough viral load to cause detectable large shifts in the peak maxima of the extinction spectra of the sensors.

Small positive (< 0.1 nm) and negative shifts were observed for patients classified as “COVID negative” by the hospital except for patient 9. A threshold for a binary classification of “COVID positive” or “COVID negative” for this sensor was defined. The samples with shifts above 0.21 were classified as “COVID positive” for the “COVID negative” classification was used for samples that produced shifts below the 0.21threshold.

This defined threshold correctly classified 8/8 COVID positive patients, (6 hospitalized and 2 outpatients). 7/8 COVID negative patients were correctly classified.

In total, it classified 93.8% of the samples correctly. The sensitivity for this sensor was determined as 100% (95% CI 79.5-100) and specificity as 87.5% (95% CI 80.5-100).[46]

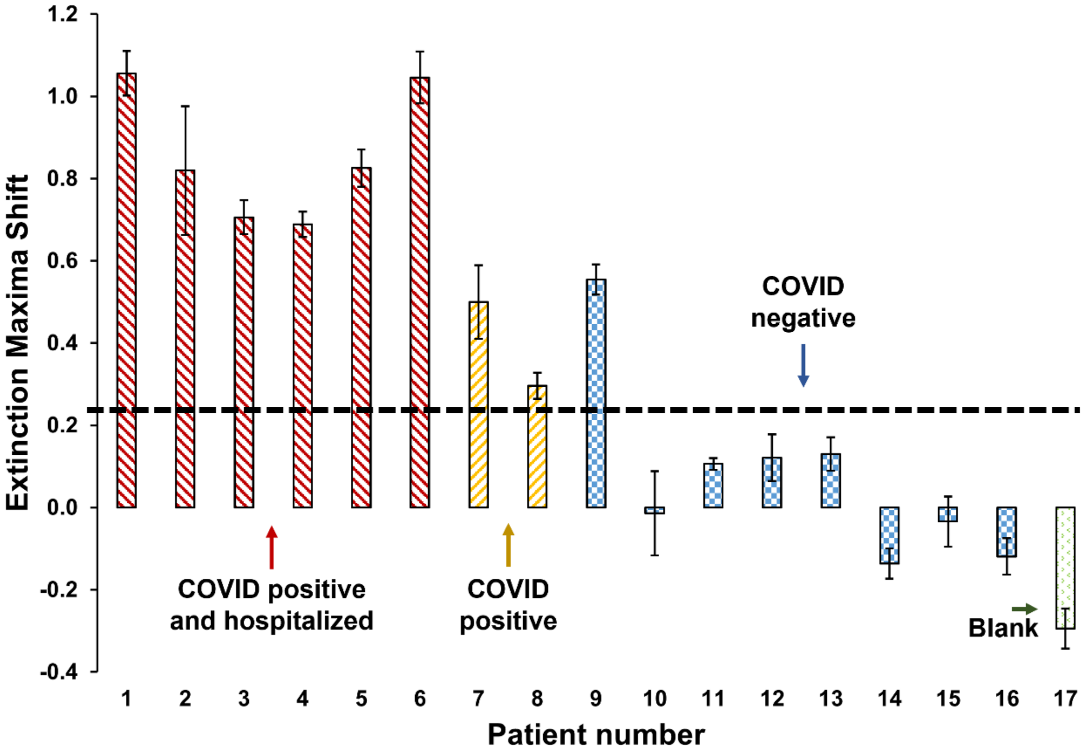

Figure 5-3. Results for samples from patients tested at CHUM. Columns with a diagonal downward stripe pattern are COVID positive patients that were hospitalized due to SARS-CoV-2, columns with a diagonal upward stripe pattern are for COVID positive outpatients, columns with a checkerboard pattern are COVID negative patients, and the column with a divot pattern is a blank. Error bars are the standard deviation of the triplicates conducted for each sample. The plate is covered with SARS-CoV-2 (2019-nCoV) Spike S2 Antibody and is testing for the presence of SARS-CoV-2 virus in saliva. The dashed line shows a possible threshold for this sensor.

5.3.3 Antibody Detection

Figure 5-4 shows the results for the patient samples for sensors with S1+S2 protein as recognition element. Those sensors were testing for the presence of SARS-CoV-2 antibody in saliva i.e. the immune response. The tested patient numbers are correspondent between the plates, i.e. same samples, for Figures 5-3 and 5-4.

Previous studies show that the viral load of SARS-CoV-2 peaks at the first week post-symptom onset (PSO)[47] and salivary SARS-CoV-2 IgG levels are consistent with serum levels.[48] Viral RNA can also be detected in patient saliva for up to 27 days PSO. [49] Anti-SARS-CoV-2 antibodies have been detected in serum and saliva samples for infected patients in samples collected on day 3 PSO and reached maximum levels 16–30 days PSO.[50] Therefore, the virus and anti-SARS-CoV-2 antibodies coexist in the saliva shortly after the infection is detectable.

A large positive shift was observed for patients 1 to 6 in Figure 5-4, for patients classified as “COVID positive hospitalized”. The sensors were then able to detect antibodies against SARS-CoV-2 present in saliva. Similarly to observed in Figure 5-3, a negative shift is seen for the blank, perhaps due the use of Triton X-100 to deactivate the virus for transport as discussed above. COVID positive outpatients presented small negative shifts. All patients classified as “COVID negative”, excluding patient number 9 presented large negative shifts.

A threshold for a binary classification of “COVID positive” or “COVID negative” was defined for this sensor. The patient samples with response above -0.31 were classified as “COVID positive” and the ones below -0.31 were classified as “COVID negative”. The sensor correctly classifies all 8 of the COVID positive patients, being either hospitalized or outpatients as COVID positive. The sensor correctly classifies 7/8 negative patients as COVID negative. The misclassification of the negative patient was for the same patient in both plates (number 9). Since the sensors contain different elements of recognition (either Spike S2 Ab or S1+S2 protein) it is possible that this was a false negative in the hospital classification (PCR test). The antibody detection sensor (Figure 5-4) has the same correct/ incorrect sample classifications as the viral detection sensor (Figure 5-3). Therefore, the sensitivity and specificity are the same, determined as 100% (95% CI 79.5-100) and 87.5% (95% CI 80.5-100), respectively.[46]

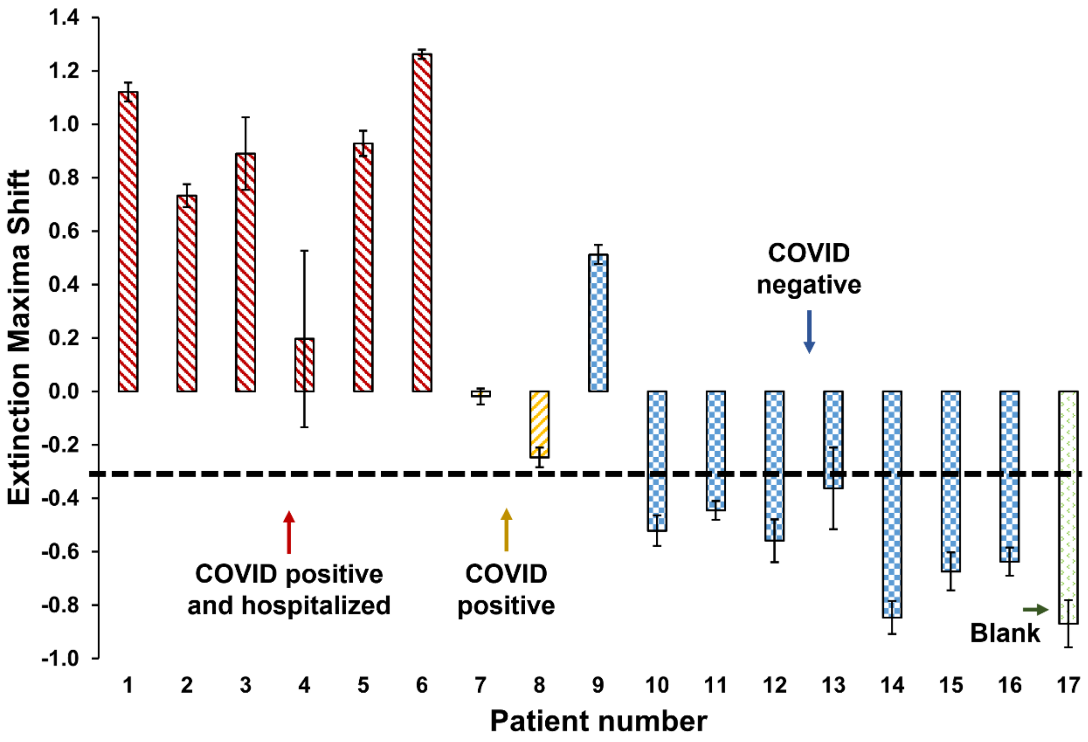

Figure 5-4. Results for samples from patients tested at CHUM. Columns with a diagonal downward stripe pattern are COVID positive patients that were hospitalized due to SARS-CoV-2, columns with a diagonal upward stripe pattern are for COVID positive outpatients, columns with a checkerboard pattern are COVID negative patients, and the column with a divot pattern is a blank. Error bars are the standard deviation of the triplicates conducted for each sample. The plate is covered with SARS-CoV-2 (2019-nCoV) Spike S1 + S2 ECD-His Recombinant Protein and is testing for the presence of SARS-CoV-2 antibody in saliva. The dashed line shows a possible threshold for this sensor.

5.3.4 Receiver Operating Characteristic (ROC) Curves

Receiver operating characteristic (ROC) curves were constructed for the tested plates using the results presented in Figures 5-3 and 5-4. Figure 5-5A is an ROC curve constructed from the data in Figure 5-3 while Figure 5-5B is a ROC curve constructed from the data in Figure 5-4. The ROC curve is a plot of the sensitivity (true positive rate, TRP) versus 1-specificity (false positive rate, FRP) considering for all possible cutoff points (thresholds) for the classifier (LSPR peak shift in our case). An ROC curve is a useful evaluation of new diagnostic tests and it is used to provide a visual comparison of the efficacy of two or more tests.[51] Specifically, the area under the curve (AUC) can be employed to compare diagnostic tools. An AUC of 1.0 would indicate a perfect diagnostic test, whereas an AUC of 0.5 indicates a test with no discriminatory ability.[52]

Tables C-S1 and C-S2 in Appendix C tabulates the thresholds, TPR and FPR used to construct the ROC curves in Figure 5-5. The area under the curve (AUC) for Figure 5-5A was determined to be 0.97 and for Figure 5-5B was 0.96.

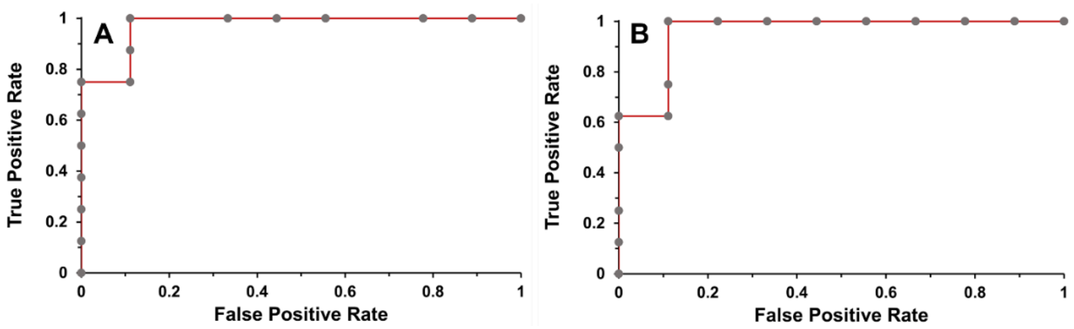

Figure 5-5. Receiver operating characteristic (ROC) curves corresponding to the tested plates shown in Figures 5-3 and 5-4, respectively. A) The plate is covered with SARS-CoV-2 (2019-nCoV) Spike S2 Antibody and is testing for the presence of SARS-CoV-2 virus in saliva. B) The plate is covered with SARS-CoV-2 (2019-nCoV) Spike S1 + S2 ECD-His Recombinant Protein and is testing for the presence of SARS-CoV-2 antibody in saliva.

5.4 Conclusion

In conclusion, this work presents LSPR-based sensors constructed for the detection of either SARS-CoV-2 virus or SARS-CoV-2 antibody in saliva. Other LSPR sensors were developed for SARS-CoV-2 detection. However, some were developed for serum[53,54], plasma[55,56], nasopharyngeal swabs[57] or not tested in a body fluid or comparative media [58,59]. Other relies on more complex construction (e.g. electrochemical anodization, thermal oxidation and metal coating [60,61] ; silver nanotriangle array fabrication[62]) in comparison to our simple fabrication. In our method, a 1% PEI solution in water is added to the plastic for 45 minutes, washed with water and then added the silver colloid to form the film.

The sensors were tested in patients' saliva, for 16 patients, in triplicates, for both sensor modalities with a sensitivity determined as 100% (95% CI 79.5-100) and specificity as

87.5% (95% CI 80.5-100) in both test modalities (i.e. viral or immune response detection). The sensors were able to correctly identify all COVID positive patients (hospitalized or outpatients) and 7/8 negative COVID patients correctly. The AUC for the ROC curve was 0.97 for viral detection and 0.96 for the antibody detection, based on the chosen thresholds of 0.21 and -0.31 extinction maxima shift, respectively.

It is important to consider that a next step with a larger pool of samples would be required to define a definitive threshold with more robust statistics. In any case, these sensors are inexpensive, and they can be constructed with widely available materials and reagents. The price for the sensors, without the recognition elements is less than $0.1 per well. The antibody used for the viral detection cost is estimated as $2.30 per sensor and the protein used for the antibody detection cost was about $2.09 per sensor. The cost can be vastly decreased if the materials are bought in bulk or if the elements of recognition are made in-house. The sensors can be constructed in strips for individual point of care deployment or used in plates for high throughput assays, since there is no requirement for specialized equipment for their deployment. Therefore proof-of-concept assay is a potential contribution for the deployment of screening tests in underserved communities.

5.5 References

(1) WHO Coronavirus (COVID-19) Dashboard. https://covid19.who.int (accessed 2023-01-16).

(2) Penninx, B. W. J. H.; Benros, M. E.; Klein, R. S.; Vinkers, C. H. How COVID-19 Shaped Mental Health: From Infection to Pandemic Effects. Nat Med 2022, 28 (10), 2027–2037.

(3) Varga, T. V.; Bu, F.; Dissing, A. S.; Elsenburg, L. K.; Bustamante, J. J. H.; Matta, J.; van Zon, S. K. R.; Brouwer, S.; Bültmann, U.; Fancourt, D.; Hoeyer, K.; Goldberg, M.; Melchior, M.; Strandberg-Larsen, K.; Zins, M.; Clotworthy, A.; Rod, N. H. Loneliness, Worries, Anxiety, and Precautionary Behaviours in Response to the COVID-19 Pandemic: A Longitudinal Analysis of 200,000 Western and Northern Europeans. Lancet Reg Health Eur 2021, 2, 100020.

(4) Richards, F.; Kodjamanova, P.; Chen, X.; Li, N.; Atanasov, P.; Bennetts, L.; Patterson, B. J.; Yektashenas, B.; Mesa-Frias, M.; Tronczynski, K.; Buyukkaramikli, N.; El Khoury, A. C. Economic Burden of COVID-19: A Systematic Review. Clinicoecon Outcomes Res 2022, 14, 293–307.

(5) Cutler, D. M.; Summers, L. H. The COVID-19 Pandemic and the $16 Trillion Virus. JAMA 2020, 324 (15), 1495–1496.

(6) Moghadas, S. M.; Vilches, T. N.; Zhang, K.; Wells, C. R.; Shoukat, A.; Singer, B. H.; Meyers, L. A.; Neuzil, K. M.; Langley, J. M.; Fitzpatrick, M. C.; Galvani, A. P. The Impact of Vaccination on COVID-19 Outbreaks in the United States. medRxiv 2021, 2020.11.27.20240051.

(7) Wahl, I.; Wardemann, H. Sterilizing Immunity: Understanding COVID-19. Immunity 2022, 55 (12), 2231–2235.

(8) Zhou, W.; Wang, W. Fast-Spreading SARS-CoV-2 Variants: Challenges to and New Design Strategies of COVID-19 Vaccines. Sig Transduct Target Ther 2021, 6 (1), 1–6.

(9) Liu, C.; Shi, W.; Becker, S. T.; Schatz, D. G.; Liu, B.; Yang, Y. Structural Basis of Mismatch Recognition by a SARS-CoV-2 Proofreading Enzyme. Science 2021, 373 (6559), 1142–1146.

(10) Impact of Vaccination on Coronavirus Disease 2019 (COVID-19) Outbreaks in the United States | Clinical Infectious Diseases | Oxford Academic. https://academic.oup.com/cid/article/73/12/2257/6124429 (accessed 2023-01-16).

(11) Toro-Huamanchumo, C. J.; Hilario-Gomez, M. M.; Pinedo-Castillo, L.; Zumarán-Nuñez, C. J.; Espinoza-Gonzales, F.; Caballero-Alvarado, J.; Rodriguez-Morales, A. J.; Barboza, J. J. Clinical and Epidemiological Features of Patients with COVID-19 Reinfection: A Systematic Review. New Microbes and New Infections 2022, 48, 101021.

(12) Bong, C.-L.; Brasher, C.; Chikumba, E.; McDougall, R.; Mellin-Olsen, J.; Enright, A. The COVID-19 Pandemic: Effects on Low- and Middle-Income Countries. Anesthesia & Analgesia 2020, 131 (1), 86.

(13) Duma, Z.; Chuturgoon, A. A.; Ramsuran, V.; Edward, V.; Naidoo, P.; Mpaka-Mbatha, M. N.; Bhengu, K. N.; Nembe, N.; Pillay, R.; Singh, R.; Mkhize-Kwitshana, Z. L. The Challenges of Severe Acute Respiratory Syndrome Coronavirus 2 (SARS-CoV-2) Testing in Low-Middle Income Countries and Possible Cost-Effective Measures in Resource-Limited Settings. Global Health 2022, 18 (1), 5.

(14) Boro, E.; Stoll, B. Barriers to COVID-19 Health Products in Low-and Middle-Income Countries During the COVID-19 Pandemic: A Rapid Systematic Review and Evidence Synthesis. Front Public Health 2022, 10, 928065.

(15) Pokhrel, P.; Hu, C.; Mao, H. Detecting the Coronavirus (COVID-19). ACS Sens. 2020, 5 (8), 2283–2296.

(16) Houston, H.; Gupta-Wright, A.; Toke-Bjolgerud, E.; Biggin-Lamming, J.; John, L. Diagnostic Accuracy and Utility of SARS-CoV-2 Antigen Lateral Flow Assays in Medical Admissions with Possible COVID-19. J Hosp Infect 2021, 110, 203–205.

(17) Heskin, J.; Pallett, S. J. C.; Al-Hindawi, A.; Davies, G. W.; Rayment, M.; Mughal, N.; Randell, P.; Jones, R.; Moore, L. S. P. Evaluating the Performance Characteristics of Five Lateral Flow Assays for the Detection of the SARS-CoV-2 Nucleocapsid Antigen. Sci Rep 2022, 12 (1), 8811.

(18) Ma, Q.; Liu, J.; Liu, Q.; Kang, L.; Liu, R.; Jing, W.; Wu, Y.; Liu, M. Global Percentage of Asymptomatic SARS-CoV-2 Infections Among the Tested Population and Individuals With Confirmed COVID-19 Diagnosis: A Systematic Review and Meta-Analysis. JAMA Network Open 2021, 4 (12), e2137257.

(19) Fan, M.; Thompson, M.; Andrade, M. L.; Brolo, A. G. Silver Nanoparticles on a Plastic Platform for Localized Surface Plasmon Resonance Biosensing. Anal. Chem. 2010, 82 (15), 6350–6352.

(20) Leopold, N.; Lendl, B. A New Method for Fast Preparation of Highly Surface-Enhanced Raman Scattering (SERS) Active Silver Colloids at Room Temperature by Reduction of Silver Nitrate with Hydroxylamine Hydrochloride. J. Phys. Chem. B 2003, 107 (24), 5723–5727.

(21) de la Rica, R.; Stevens, M. M. Plasmonic ELISA for the Detection of Analytes at Ultralow Concentrations with the Naked Eye. Nat Protoc 2013, 8 (9), 1759–1764.

(22) Lourenço, E. V.; Roque-Barreira, M.-C. Immunoenzymatic Quantitative Analysis of Antigens Expressed on the Cell Surface (Cell-ELISA). In Immunocytochemical

Methods and Protocols; Oliver, C., Jamur, M. C., Eds.; Methods in Molecular Biology; Humana Press: Totowa, NJ, 2010; pp 301–309.

(23) Vancha, A. R.; Govindaraju, S.; Parsa, K. V.; Jasti, M.; González-García, M.; Ballestero, R. P. Use of Polyethyleneimine Polymer in Cell Culture as Attachment Factor and Lipofection Enhancer. BMC Biotechnol 2004, 4, 23.

(24) Cobley, C. M.; Skrabalak, S. E.; Campbell, D. J.; Xia, Y. Shape-Controlled Synthesis of Silver Nanoparticles for Plasmonic and Sensing Applications. Plasmonics 2009, 4 (2), 171–179.

(25) Stewart, A.; Zheng, S.; McCourt, M. R.; Bell, S. E. J. Controlling Assembly of Mixed Thiol Monolayers on Silver Nanoparticles to Tune Their Surface Properties. ACS Nano 2012, 6 (5), 3718–3726.

(26) Holzer, B.; Manoli, K.; Ditaranto, N.; Macchia, E.; Tiwari, A.; Franco, C. D.; Scamarcio, G.; Palazzo, G.; Torsi, L. Characterization of Covalently Bound Anti-Human Immunoglobulins on Self-Assembled Monolayer Modified Gold Electrodes. Advanced Biosystems 2017, 1 (11), 1700055.

(27) Li, D.; Han, B.; Wei, R.; Yao, G.; Chen, Z.; Liu, J.; Poon, T. C. W.; Su, W.; Zhu, Z.; Dimitrov, D. S.; Zhao, Q. N-Terminal α-Amino Group Modification of Antibodies Using a Site-Selective Click Chemistry Method. mAbs 2018, 10 (5), 712–719.

(28) Huang, Y.; Yang, C.; Xu, X.; Xu, W.; Liu, S. Structural and Functional Properties of SARS-CoV-2 Spike Protein: Potential Antivirus Drug Development for COVID-19. Acta Pharmacol Sin 2020, 41 (9), 1141–1149.

(29) Watanabe, C.; Okiyama, Y.; Tanaka, S.; Fukuzawa, K.; Honma, T. Molecular Recognition of SARS-CoV-2 Spike Glycoprotein: Quantum Chemical Hot Spot and Epitope Analyses. Chemical Science 2021, 12 (13), 4722–4739.

(30) Fischer, M. J. E. Amine Coupling Through EDC/NHS: A Practical Approach. In Surface Plasmon Resonance: Methods and Protocols; Mol, N. J., Fischer, M. J. E., Eds.; Methods in Molecular Biology; Humana Press: Totowa, NJ, 2010; pp 55–73.

(31) Reimhult, K.; Petersson, K.; Krozer, A. QCM-D Analysis of the Performance of Blocking Agents on Gold and Polystyrene Surfaces. Langmuir 2008, 24 (16), 8695–8700.

(32) Pakiari, A. H.; Jamshidi, Z. Nature and Strength of M−S Bonds (M = Au, Ag, and Cu) in Binary Alloy Gold Clusters. J. Phys. Chem. A 2010, 114 (34), 9212–9221.

(33) Diaz, D.; Rivera, M.; Ni, T.; Rodriguez, J.-C.; Castillo-Blum, S.-E.; Nagesha, D.; Robles, J.; Alvarez-Fregoso, O.-J.; Kotov, N. A. Conformation of Ethylhexanoate Stabilizer on the Surface of CdS Nanoparticles. J. Phys. Chem. B 1999, 103 (45), 9854–9858.

(34) Bhattarai, K. R.; Kim, H.-R.; Chae, H.-J. Compliance with Saliva Collection Protocol in Healthy Volunteers: Strategies for Managing Risk and Errors. Int J Med Sci 2018, 15 (8), 823–831.

(35) Munro, C. L.; Grap, M. J.; Jablonski, R.; Boyle, A. Oral Health Measurement in Nursing Research: State of the Science. Biological Research For Nursing 2006, 8 (1), 35–42.

(36) Topkas, E.; Keith, P.; Dimeski, G.; Cooper-White, J.; Punyadeera, C. Evaluation of Saliva Collection Devices for the Analysis of Proteins. Clinica Chimica Acta 2012, 413 (13), 1066–1070.

(37) Williamson, S.; Munro, C.; Pickler, R.; Grap, M. J.; Elswick, R. K. Comparison of Biomarkers in Blood and Saliva in Healthy Adults. Nursing Research and Practice 2012, 2012, e246178.

(38) Ember, K.; Daoust, F.; Mahfoud, M.; Dallaire, F.; Ahmad, E. Z.; Tran, T.; Plante, A.; Diop, M.-K.; Nguyen, T.; St-Georges-Robillard, A.; Ksantini, N.; Lanthier, J.; Filiatrault, A.; Sheehy, G.; Beaudoin, G.; Quach, C.; Trudel, D.; Leblond, F. Saliva-Based Detection of COVID-19 Infection in a Real-World Setting Using Reagent-Free Raman Spectroscopy and Machine Learning. J. Biomed. Opt. 2022, 27 (02).

(39) Patterson, E. I.; Prince, T.; Anderson, E. R.; Casas-Sanchez, A.; Smith, S. L.; Cansado-Utrilla, C.; Solomon, T.; Griffiths, M. J.; Acosta-Serrano, Á.; Turtle, L.; Hughes, G. L. Methods of Inactivation of SARS-CoV-2 for Downstream Biological Assays. J Infect Dis 2020, jiaa507.

(40) Unser, S.; Bruzas, I.; He, J.; Sagle, L. Localized Surface Plasmon Resonance Biosensing: Current Challenges and Approaches. Sensors (Basel) 2015, 15 (7), 15684–15716.

(41) dos Santos, K. C.; da Silva, M. F. G.; Pereira-Filho, E. R.; Fernandes, J. B.; Polikarpov, I.; Forim, M. R. Polymeric Nanoparticles Loaded with the 3,5,3′-Triiodothyroacetic Acid (Triac), a Thyroid Hormone: Factorial Design, Characterization, and Release Kinetics. Nanotechnology, Science and Applications 2012, 5, 37–48.

(42) Belem, W. F.; Liu, C.-H.; Hu, Y.-T.; Burnouf, T.; Lin, L.-T. Validation of Viral Inactivation Protocols for Therapeutic Blood Products against Severe Acute Respiratory Syndrome Coronavirus-2 (SARS-CoV-2). Viruses 2022, 14 (11), 2419.

(43) Qualtiere, L. F.; Anderson, A. G.; Meyers, P. Effects of Ionic and Nonionic Detergents on Antigen-Antibody Reactions. J Immunol 1977, 119 (5), 1645–1651.

(44) Singh, S. K.; Kishore, N. Thermodynamic Insights into the Binding of Triton X-100 to Globular Proteins: A Calorimetric and Spectroscopic Investigation. J. Phys. Chem. B 2006, 110 (19), 9728–9737.

(45) Vlasova, I. M.; Vlasov, A. A.; Saletskii, A. M. Complexation of Serum Albumins and Triton X-100: Quenching of Tryptophan Fluorescence and Analysis of the Rotational Diffusion of Complexes. Russ. J. Phys. Chem. 2016, 90 (7), 1479–1483.

(46) Berkman, N. D.; Wallace, I.; Watson, L.; Coyne-Beasley, T.; Cullen, K.; Wood, C.; Lohr, K. N. Formulas for Accuracy; Agency for Healthcare Research and Quality (US), 2015.

(47) Xu, R.; Cui, B.; Duan, X.; Zhang, P.; Zhou, X.; Yuan, Q. Saliva: Potential Diagnostic Value and Transmission of 2019-NCoV. Int J Oral Sci 2020, 12 (1), 1–6.

(48) Pisanic, N.; Randad, P. R.; Kruczynski, K.; Manabe, Y. C.; Thomas, D. L.; Pekosz, A.; Klein, S. L.; Betenbaugh, M. J.; Clarke, W. A.; Laeyendecker, O.; Caturegli, P. P.; Larman, H. B.; Detrick, B.; Fairley, J. K.; Sherman, A. C.; Rouphael, N.; Edupuganti, S.; Granger, D. A.; Granger, S. W.; Collins, M. H.; Heaney, C. D. COVID-19 Serology at Population Scale: SARS-CoV-2-Specific Antibody Responses in Saliva. J Clin Microbiol 2020, 59 (1), e02204-20.

(49) Congrave-Wilson, Z.; Lee, Y.; Jumarang, J.; Perez, S.; Bender, J. M.; Bard, J. D.; Pannaraj, P. S. Change in Saliva RT-PCR Sensitivity Over the Course of SARS-CoV-2 Infection. JAMA 2021, 326 (11), 1065–1067.

(50) Isho, B.; Abe, K. T.; Zuo, M.; Jamal, A. J.; Rathod, B.; Wang, J. H.; Li, Z.; Chao, G.; Rojas, O. L.; Bang, Y. M.; Pu, A.; Christie-Holmes, N.; Gervais, C.; Ceccarelli, D.; Samavarchi-Tehrani, P.; Guvenc, F.; Budylowski, P.; Li, A.; Paterson, A.; Yue, F. Y.; Marin, L. M.; Caldwell, L.; Wrana, J. L.; Colwill, K.; Sicheri, F.; Mubareka, S.; Gray-Owen, S. D.; Drews, S. J.; Siqueira, W. L.; Barrios-Rodiles, M.; Ostrowski, M.; Rini, J. M.; Durocher, Y.; McGeer, A. J.; Gommerman, J. L.; Gingras, A.-C. Persistence of Serum and Saliva Antibody Responses to SARS-CoV-2 Spike Antigens in COVID-19 Patients. Science Immunology 2020, 5 (52), eabe5511.

(51) Hajian-Tilaki, K. Receiver Operating Characteristic (ROC) Curve Analysis for Medical Diagnostic Test Evaluation. Caspian J Intern Med 2013, 4 (2), 627–635.

(52) García, J. P.; Ferreira, J. C.; Patino, C. M. Receiver Operating Characteristic Analysis: An Ally in the Pandemic. J Bras Pneumol 2021, 47 (2), e20210139.

(53) Funari, R.; Chu, K.-Y.; Shen, A. Q. Detection of Antibodies against SARS-CoV-2 Spike Protein by Gold Nanospikes in an Opto-Microfluidic Chip. Biosensors and Bioelectronics 2020, 169, 112578.

(54) Bhalla, N.; Payam, A. F.; Morelli, A.; Sharma, P. K.; Johnson, R.; Thomson, A.; Jolly, P.; Canfarotta, F. Nanoplasmonic Biosensor for Rapid Detection of Multiple Viral Variants in Human Serum. Sensors and Actuators B: Chemical 2022, 365, 131906.

(55) Masterson, A. N.; Sardar, R. Selective Detection and Ultrasensitive Quantification of SARS-CoV-2 IgG Antibodies in Clinical Plasma Samples Using Epitope-Modified Nanoplasmonic Biosensing Platforms. ACS Appl. Mater. Interfaces 2022, 14 (23), 26517–26527.

(56) Masterson, A. N.; Muhoberac, B. B.; Gopinadhan, A.; Wilde, D. J.; Deiss, F. T.; John, C. C.; Sardar, R. Multiplexed and High-Throughput Label-Free Detection of RNA/Spike Protein/IgG/IgM Biomarkers of SARS-CoV-2 Infection Utilizing Nanoplasmonic Biosensors. Anal. Chem. 2021, 93 (25), 8754–8763.

(57) Luo, Z.; Cheng, Y.; He, L.; Feng, Y.; Tian, Y.; Chen, Z.; Feng, Y.; Li, Y.; Xie, W.; Huang, W.; Meng, J.; Li, Y.; He, F.; Wang, X.; Duan, Y. T-Shaped Aptamer-Based LSPR Biosensor Using Ω-Shaped Fiber Optic for Rapid Detection of SARS-CoV-2. Anal. Chem. 2023, 95 (2), 1599–1607.

(58) Qiu, G.; Gai, Z.; Tao, Y.; Schmitt, J.; Kullak-Ublick, G. A.; Wang, J. Dual-Functional Plasmonic Photothermal Biosensors for Highly Accurate Severe Acute Respiratory Syndrome Coronavirus 2 Detection. ACS Nano 2020, 14 (5), 5268–5277.

(59) Taghipour, A.; Heidarzadeh, H. Design and Analysis of Highly Sensitive LSPR-Based Metal–Insulator–Metal Nano-Discs as a Biosensor for Fast Detection of SARS-CoV-2. Photonics 2022, 9 (8), 542.

(60) Rong, G.; Zheng, Y.; Li, X.; Guo, M.; Su, Y.; Bian, S.; Dang, B.; Chen, Y.; Zhang, Y.; Shen, L.; Jin, H.; Yan, R.; Wen, L.; Zhu, P.; Sawan, M. A High-Throughput Fully Automatic Biosensing Platform for Efficient COVID-19 Detection. Biosensors and Bioelectronics 2023, 220, 114861.

(61) Zheng, Y.; Bian, S.; Sun, J.; Wen, L.; Rong, G.; Sawan, M. Label-Free LSPR-Vertical Microcavity Biosensor for On-Site SARS-CoV-2 Detection. Biosensors 2022, 12 (3), 151.

(62) Yang, Y.; Murray, J.; Haverstick, J.; Tripp, R. A.; Zhao, Y. Rapid and High-Sensitive LSPR Sensor for Coronavirus Detection. In Chemical, Biological, Radiological,

Nuclear, and Explosives (CBRNE) Sensing XXIII; Guicheteau, J. A., Howle, C. R., Eds.; SPIE: Orlando, United States, 2022; p 59.

Chapter 7: Summary and Outlook

7.1 Summary and Conclusions

In this dissertation, metallic nanostructures were explored for the development of immunosensors and immunoassays.

In Chapter 3, a surface-enhanced spectroscopy (SERS)-based immunosensor was developed for detection of IgG from human serum. A 3D-printed platform and a method of sandwiching the platform with poly(dimethylsiloxane) (PDMS) masks was devised. Extensive data collection and analysis of the population distributions for various antigen concentrations were considered. This study is a step forward towards the determination of best practices for a more reliable and robust employment of quantitative SERS-based immunoassays. It is concluded that, in order to improve the application of SERS as an analytical tool, the inherent variations of SERS signals have to be embraced and methods of analysis have to be put in place. Specifically, the necessity of a larger number of measurements compared to other methods, the distance between measurements and the consideration of the population distribution for data analysis. A population description is necessary to determine methods of analysis across SERS reporter concentrations, spanning from Poisson, Log-normal or Gaussian distribution. Commonly, the Gaussian distribution is considered for data analysis, without further consideration. These factors are amongst the considerations that are affecting reproducibility and robustness, specially for low and ultralow concentrations of antigens and Raman reporters.

In Chapter 4, a SERS-based immunoassay for detection of SARS-CoV-2 in saliva was developed as a proof of concept for the use of a digital protocol for immunoassays.

This data analysis is a proposed method to tackle another challenge in the use of SERS in immunoassays. As the extrinsic Raman labels (ERLs) decrease in number on the probed sensor surface, the linearity between concentration and SERS signal is lost. The developed method consists in attributing 1 and 0 to the SERS intensities of the probed Raman reporter that are above and below a defined threshold. The method compares the traditional method and the digital approach and shows that the linearity is recuperated for the digital method, relating counts instead of average signal to concentration of antigen.

In Chapter 5, low-cost sensor was developed for detection of viral particles of SARS-CoV-2 in saliva and for the immune response to SARS-CoV-2 (antibodies against the disease). The sensor was tested in patient’s saliva at Center hospitalier de l'Université de Montréal (CHUM). Both modalities of the sensor had a sensitivity of 100% (95% CI 79.5-100) and specificity of 87.5% (95% CI 80.5-100). This sensor addresses the need for cheap sensors, constructed with widely available materials to reach underserved communities. The pandemic accentuated the importance of access to sensitive tests that can be mass produced and deployed. Additionally, it highlighted the inequality of the access to tools necessary for informed decisions for spread containment.

7.2 Outlook and Future Directions

The vast use of metallic nanostructures for the development of immunosensors and immunoassays will continue to evolve.

Results in Chapter 3 are a step towards the considerations to improve reproducibility and robustness of SERS as analytical tool for immunoassays. More studies are necessary to define universal parameters that consider variations in substrates, Raman reporters and

Raman systems. Our group is pursuing a method of standardization of substrates against a gold standard in partnership with the metrology research center at the National Research Council Canada (NRC-CNRC). This involves the definition of a gold standard and definition of procedures and statistical parameters that compare those substrates with the defined gold standard. This is another step towards improving SERS as an analytical tool. The development of those statistical analysis of variance in the substrate can be used in the assay conducted in chapter 3 and applied to other immunoassays, to evaluate how the number of measurements relate to the % error for different immunoassay substrates. The definition of statistics to evaluate substrates/sensors opens the door to systematically define procedures, including how many measurements, the method/parameters of taking them to an accepted variation within the community. Additionally, the same studies should be conducted in different laboratories to have a cross comparison between Raman systems.

The method developed in Chapter 4 is useful to improve the LOD/LOQ of immunoassays. This opens up the opportunity to measure lower concentrations of SERS-based immunoassays, increasing the range of probed concentrations. The next step for this approach is to perform this data analysis in diverse SERS based immunoassays and systematically define the improvement and conditions in which this protocol can be applied.

In Chapter 5, a SARS-CoV-2 sensor for saliva in two modalities, viral and immunological response, was developed and tested in patient’s sample. The access to samples were a challenge since many studies were being conducted amidst the pandemic that needed samples. Additionally, most hospitals and workers were overwhelmed, further complicating the process of collection since the priorities were in patient treatment. The next step is to test this sensor in more samples, to have a more robust statistics to compare to commercially available sensor and to validate its sensitivity, specificity and the cut-off points (threshold) for the classifier. Investments in biomedical research for the improvement and/or development of sensors, especially after the global SARS-CoV-2 pandemic, will keep finding solutions for testing. The use of metallic structures in those sensors will continue to be explored and improved upon.

Appendix A

Appendix A is published as Support Information to: Ariadne Tuckmantel Bido, Arash Azarakhshi, and Alexandre G. Brolo, "Exploring Intensity Distributions and Sampling in SERS-Based Immunoassays." Analytical Chemistry 2022 94 (49), 17031-17038. Copyright: Reproduced with permission.

A1. Lateral Flow Assay (LFA)

A1.1 Protocol

A nitrocellulose piece was cut into a strip and hydrated in a humidity chamber for 15 minutes, at 37 °C. Next, 5 μL of the corresponding antibodies were deposited in the negative control and test line at 1 mg.mL^{-1} and dried at 37 °C for 1 hour. The membrane was covered with 100-150 μL of blocking buffer, consisted of 1% BSA in PBS-10, and was incubated for 20 minutes in the humidity chamber. The strip was washed three times with washing buffer, consisting of PBS-10 with 0.05% tween 20. Lastly, the strip was dried at 37 °C for 15 minutes and subsequently used. The sample volume added to the sample pad was 5 μL at 1 mg.mL^{-1} followed by 200 μL of the runner buffer.

A1.2 Description

A test strip was constructed with a sample pad, a conjugate pad, a nitrocellulose membrane containing a test line, a negative control line, and an absorbent pad. Figure A-S1A shows a schematic of the test strip. The test is done by adding the sample IgG from human serum in PBS-10 directly to the sample pad and subsequently running buffer, consisting of 1% sucrose in PBS-10.[1,2] The sample flows to the conjugate pad that has the ERLs containing IgG Fab specific. When the liquid reaches the conjugate pad, the dried nanoparticles are released and mixed with the sample. If there are any target analytes that interact with the antibodies present in the ERLs, these will bind to the antibodies. The ERLs bounded with the target(s) then flow through a nitrocellulose membrane across the negative control and test line. The negative control line has antibodies (IgM) that have no interaction with the analyte(s) and should be colourless unless non-specific interaction happens. The fluid continues to flow and reaches the test line. The test line is a primary read out that has antibodies (anti-human IgG Fc specific) that binds to the analyte(s). If the ERLs have the analyte(s) bound to them, the analyte(s) will carry the ERLs with them, and the test line will be coloured. This test was repeated in duplicates for three ERL batches and showed same results, and a photo is shown in Figure A-S1B. The analyte, IgG from human serum, the same analyte being tested in the SERS-based sensor, is added as a sample and there is no visible interaction with the negative control line, IgM, that comes before the test line in the sample flow. The test line, containing anti-human IgG Fc specific, the same antibody used to cover the surface of the SERS-based sensor substrate, is very colourful, showing the strong interaction of the SERS-probe with the antigen and to the antibody present in the substrate. The colour of the test lines indicates the antibody adsorption to the ERLs was satisfactory, with an overall availability of the antigen-binding sites to interact with IgG and with little non-specific interaction with IgM.

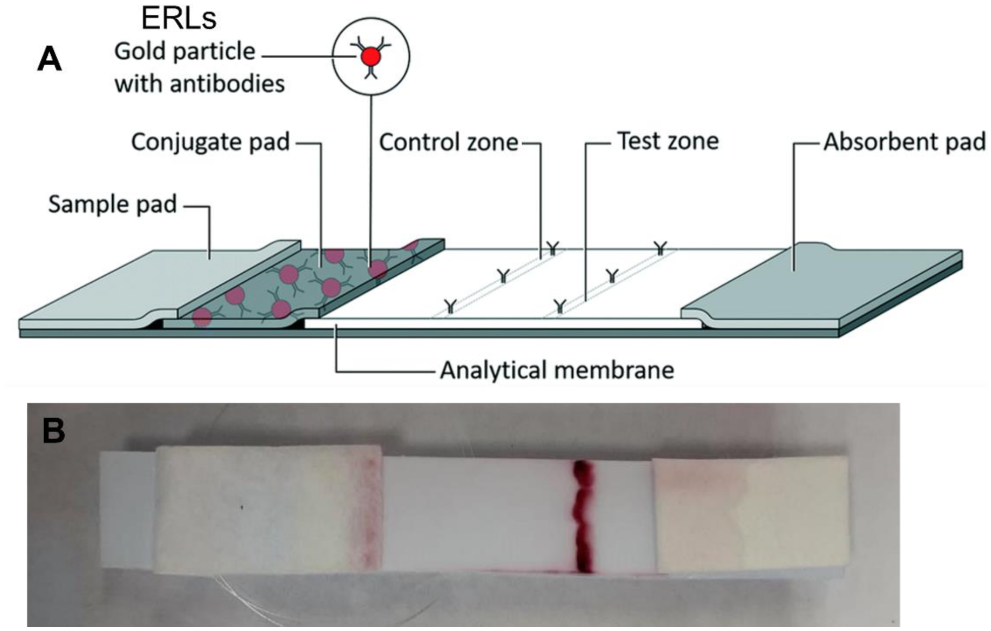

Figure A-S1. A) ERLs (with IgG Fab specific) tested in Lateral Flow Assay (FLA). Test line comprised of anti-human IgG Fc specific, a negative control line with IgM. Antigen tested IgG from human serum. B) Photo of a tested FLA strip with the ERLs.

A2. Assay Assembly in a 3D-printed Sensing Platform

A 100 nm gold-coated glass slide used as a substrate in the construction of the sensor is shown in Figure A-S2A. Areas in which the sensors will be constructed are marked in the slide. As seen in Figure A-S2C, the system consists of the substrate followed by a PDMS layer on top that has holes superposed with the marked areas. That ensures use of less resources, with the reactions constricted to the marked areas and that the sensors will be easily located for SERS measurement. A simple sensing platform made of polylactic acid (PLA) consisting of a base and a top were 3D-printed to give the sensor stability and to withstand the clamp pressure preventing deformation of the PDMS. It also allows the addition of samples to the wells without unclamping the system. The complete assembly is seen in Figure A-S2B, with the substrate, PDMS layer and top and bottom PLA clamped together with a binder clamp.

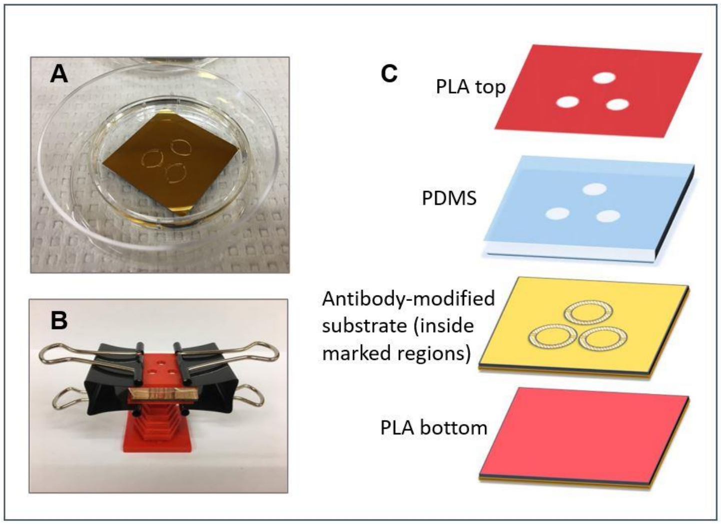

Figure A-S2. A) 100 nm gold-coated glass slide used as a substrate with marked regions. B) The assembled assay platform. C) Depiction of the layers used in the platform.

A3. Assay for Higher IgG Concentrations

The assay was repeated for higher concentrations of the analyte, IgG from human serum. Concentrations above 100 ng.mL^{-1} have a constant response, and the sensor is saturated. Above 50 ng.mL^{-1} the assay is not quantitative but is still qualitative and can be used as a Yes/ No response to the presence of the analyte.

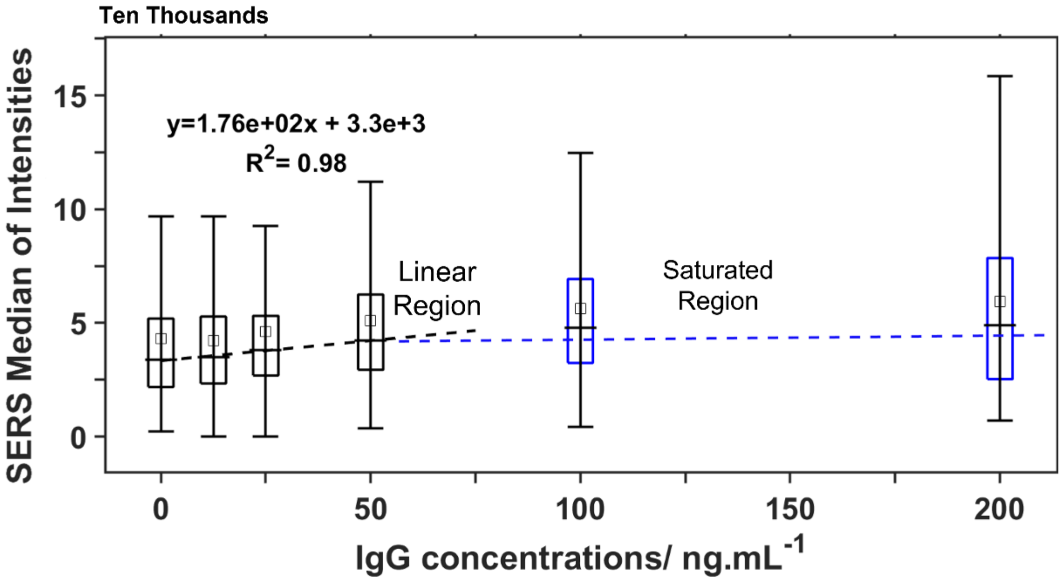

Figure A-S3. Box Plot superposed with calibration curve generated by the median of the areas under the NB peak for the 7200 measurements for each related IgG concentration for another assay with higher concentration of IgG, showing a linear region and a saturated region.

A4. Data Analysis

Figure A-S4A shows a Color Map of Intensities for one mapping taken at IgG concentration 19 ng.mL^{-1}. Each spectrum of the Raman mappings was individually baseline corrected using the Savitsky-Golay signal removal method. Figure A-S4B and A-S4C shows the raw data and after baseline correction, respectively. Each pixel of the Color Map of Intensities (Figure A-S4A, arrow), 1.1 µm^2, is color coded to the Raman intensity of the integrated area under the NB phenoxazine ring mode, centered at 592 cm^{-1} (Figure A-S4C, arrow).

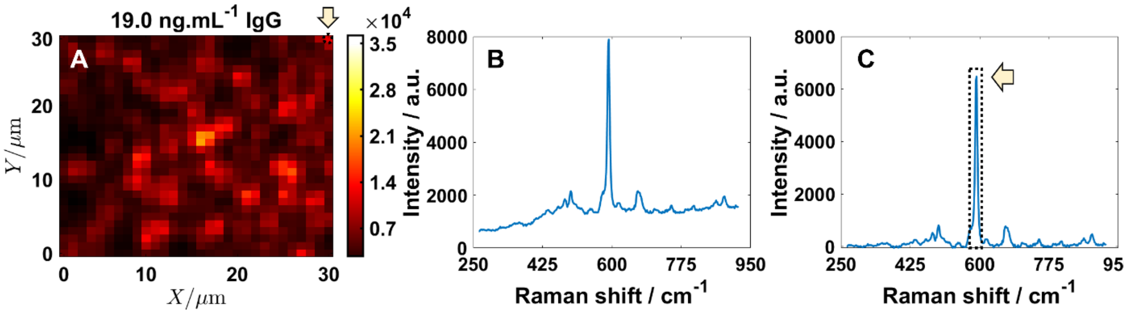

Figure A-S4. A) Color Map of Intensities of Raman measurements for a 19 ng.mL^{-1} IgG concentration; arrow is pointing to pixel correspondent to laser size. B) Raw signal correspondent to a pixel of the Color Map of Intensities. C) Signal after Savitsky-Golay signal removal method; arrow indicates the NB phenoxazine ring mode that have the area quantified for the construction of the calibration curves of this assay.

A5. SERS Intensity Distribution Histograms

The SERS intensity distribution histograms of the NB phenoxazine ring mode areas for the measured IgG concentrations are shown in Figure A-S5. The population distribution of a small number of ERLs that have highly efficient hotspots generates an intensity population distribution with a long tail.

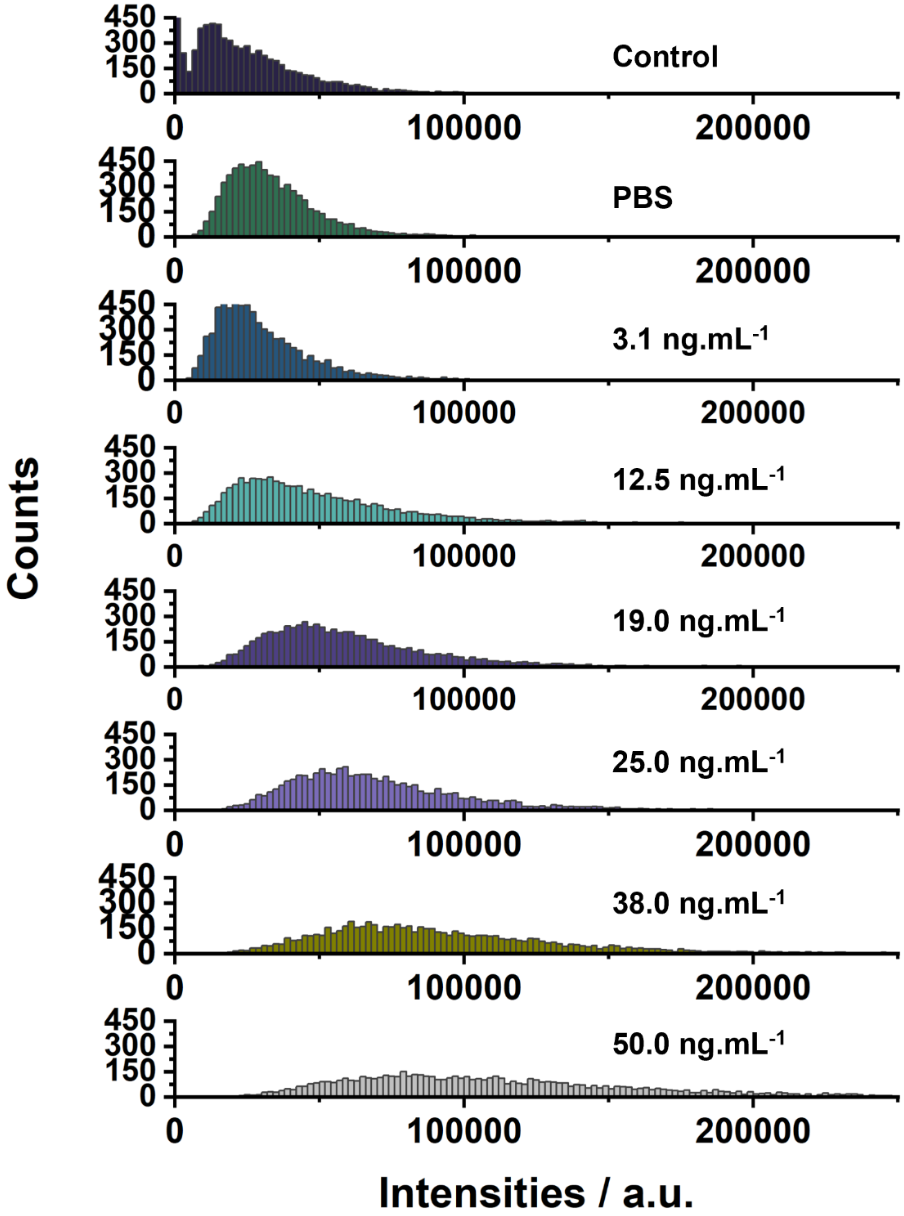

Figure A-S5. Histograms of the areas under the NB phenoxazine ring mode for 7200 measurements for duplicates of each IgG concentration, ranging from 3.1 to 50.0 ng.mL^{-1} and two controls, no antigen (PBS) and 25 ng.mL^{-1} of IgM, bin size 2000.

A6. Chi-square Test for Lognormal Distributions

To confirm that we have lognormal distributions, a chi-square test with alpha 0.01 (Figure A-2B) was conducted comparing a log normal fitting using MATLAB®, to the experimental data for all the populations according to Equation A-S1.[3]

$$\chi^2 = \sum \frac{(Observed\ frequency - Expected\ frequency)^2}{Expected\ frequency} \qquad \text{Equation A-S1}$$

The considered null hypothesis is that the distribution is log normal and the alternate hypothesis was that the distribution is not a log normal. High p-values were obtained, and it confirmed the acceptance of the null hypothesis and that the distributions are Log normal. Percent Root mean square error (%RMSE) was calculated using MATLAB® to access how close is the Log normal fit to the data. %RMSE values are low compared to the data range (Figure A-3B) and the Log normal fitting proves adequate to the distributions.

References

(1) van Amerongen, A.; Veen, J.; Arends, H. A.; Koets, M. Lateral Flow Immunoassays. In Handbook of Immunoassay Technologies; Elsevier, 2018; pp 157–182.

(2) Tomás, A. L.; de Almeida, M. P.; Cardoso, F.; Pinto, M.; Pereira, E.; Franco, R.; Matos, O. Development of a Gold Nanoparticle-Based Lateral-Flow Immunoassay for Pneumocystis Pneumonia Serological Diagnosis at Point-of-Care. Front. Microbiol. 2019, 10.

(3) Pearson, K. X. On the Criterion That a given System of Deviations from the Probable in the Case of a Correlated System of Variables Is Such That It Can Be Reasonably Supposed to Have Arisen from Random Sampling. The London, Edinburgh, and Dublin Philosophical Magazine and Journal of Science 1900, 50 (302), 157–175.

Appendix B

Appendix B is the Support Information to the unpublished work: "A Digital SERS Protocol for the Determination of SARS-CoV-2 in Saliva Samples" by Ariadne Tuckmantel Bido and Alexandre G. Brolo currently under review - manuscript ID: se-2023-001727.

B1. Lateral Flow Assay (LFA)

A LFA strip was constructed as described elsewhere.[1] It consisted of a sample pad, a conjugate pad, a nitrocellulose membrane containing a test line, a negative control line, and an absorbent pad. The control line was a negative control and contained anti-IgM. The ERLs should not react with this line. The test line contains SARS-CoV-2 Spike S2 antibody. The sample is 5 μL of antigen at 1 $mg.mL^{-1}$ in PBS-10, S1-S2 Spike Protein, followed by 200 μL of the runner buffer. The sample flowed from the sample pad to the conjugate pad, releasing the dried ERLs or the bare nanoparticles towards the negative control and test lines. Figure B-S1 shows that the ERLs successfully contain the antibodies. The ERLs interacted with the antigen in the sample and the antigen interacted with the antibody present in the test line. There was no interaction with the negative control, indicating that the unspecific binding was negligible. The bare nanoparticles did not interact with either the negative control or the test lines, indicating that the interaction was solely due to the antibodies added to the nanoparticles for the construction of ERLs. The test was carried out three times.

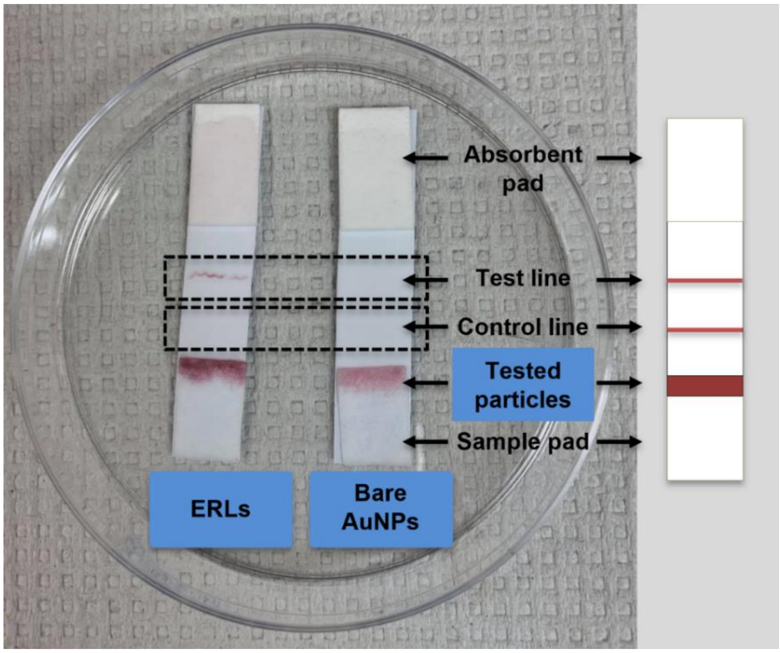

Figure B-S1. Lateral Flow Assay (LFA) used to test the ERLs binding and compare with non-modified nanoparticles (bare AuNPs). The ERLs contained SARS-CoV-2 S1 antibodies. The negative control line contained anti-IgM and did not interact with the ERLs. The test line contained SARS-CoV-2 Spike S2 antibody.

B2. Platform and PDMS Fabrication

The assembly of the platform used for this assay consisted of a polylactic acid (PLA) top and base that were 3D printed. They formed a sandwich with the sensor being modified with a PDMS (poly(dimethylsiloxane)) layer. The layers were clamped with a binder clip. A photo of this platform is shown elsewhere.[1] The PDMS layer encircled the areas of the substrate being modified. For the PDMS fabrication, a 10:1 mixture of a silicone elastomer base and an elastomer curing agent were mixed and poured into a silicon wafer that had aluminum foil wrapped to create a container for the mixture. The mixture was degassed by applying vacuum in a desiccator repeatedly. Then, the PDMS was baked at 150 °C in a hot plate for 1 h allowing it to polymerize. To prepare the PDMS masks used in the assay, the PDMS was peeled and cut into the same size as the gold-covered slides using a scalpel. The PDMS masks were gently touched with tape to make sure it was clear of any debris and then washed by gently rinsing in water and soap solution in a large beaker, then rinsed with water and ethanol abundantly and dried under a N_2 stream. These masks were cut either by having a large circle encompassing the three demarked regions of the assay and referred as PDMS mask A or with three holes that superpose the marked regions of the assay, made with a 5 mm biopsy punch and referred as PDMS mask B. Figure B-S2 shows masks A and B. Mask A is added after the SAMs formation and is consisted of a circle cut that encompasses the three marked regions on the sensor. Mask B have three 5 mm circles that encircles individual areas in the sensor surface, for the subsequent steps.

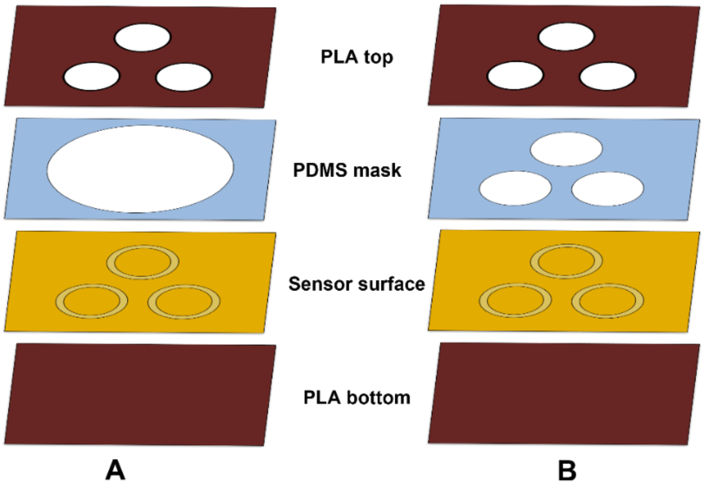

Figure B-S2. Platform assembly, consisting of a PLA top, a PDMS mask, the SERS sensor and a PLA bottom. A) the assembly with PDMS mask A, that expose the 3 areas in the sensor surface to be modified at once. B) the assembly with PDMS mask B, that expose the 3 areas of the sensor surface individually.

B3. SEM Images

SEM images were taken from all samples to estimate the number of ELRs/µm^2. Figure B-S3A shows an example of image for the PBS-10 sensor surface, for 1.56 ng.mL^{-1} of S1-S2 Spike Protein Figure B-S3B shows an example of image for the PBS-10 sensor surface, for 50 ng.mL^{-1} of S1-S2 Spike Protein.

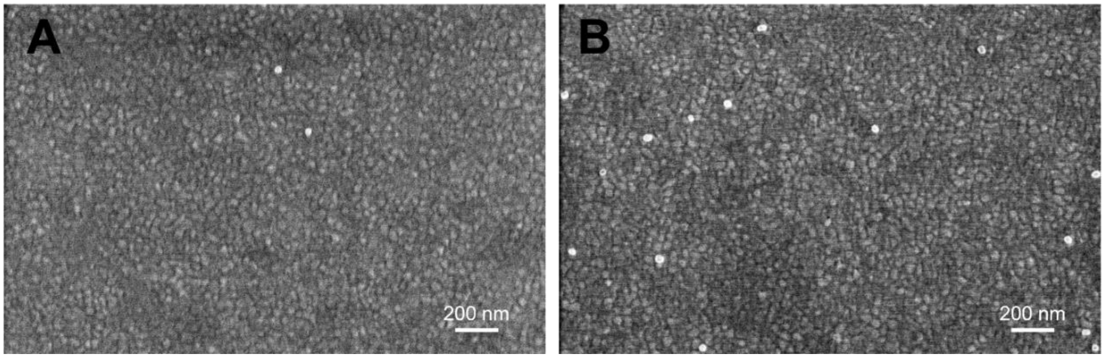

Figure B-S3. SEM images of sensor surfaces for the assay conducted in PBS-10. A) 1.56 ng.mL^{-1} of S1-S2 Spike Protein and B) 50 ng.mL^{-1} of S1-S2 Spike Protein.

B4. Digital Protocol

The Digital Protocol consists of given a 1 (counts) or 0 (no counts) classification to each spectrum and count the positive values. Figure B-S4A shows a typical raw data for a negative count and Figure B-S4C shows a typical raw data for a positive count. The first step in the data treatment is to baseline correct each spectrum using the Savitsky-Golay signal removal method. Figure B-S4B and B-S4D shows the spectra of the curves for B-S4A and B-S4C after baseline correction, respectively.

The next step is to fit use Peakfit in the NB peak region (blue arrow), centered at 592 cm^{-1}, applied to cover a range of 15 wavenumbers in each side of the centered peak, with Lorentzian peak shape and 20 iterations. The area of each spectrum peak is recorded in a matrix. As a background, the area for the same number of wavelengths, centred at 625 cm^{-1}, using the trapz function, is recorded for each spectra in another matrix.

Next, these matrices are compared. If the NB peak area is larger than three times the background, the value is considered 1; if the NB peak is equal or smaller than three times the background, it is considered a 0.

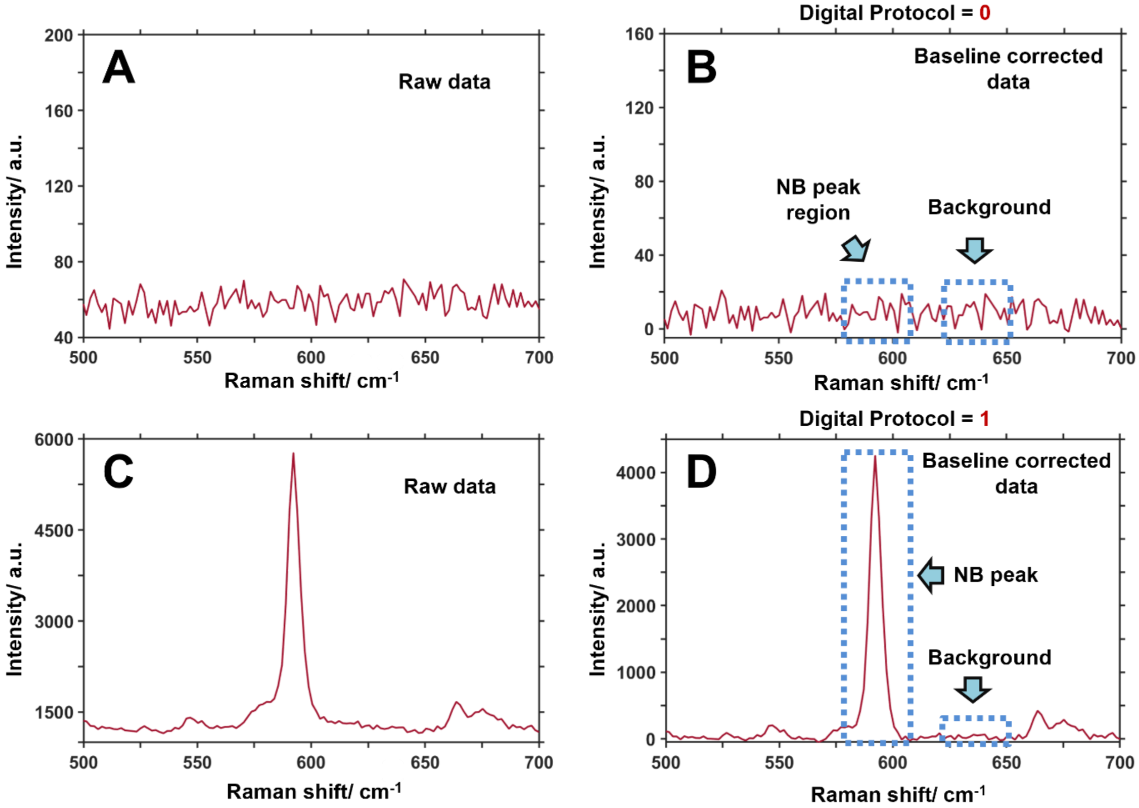

Figure B-S4. A) Typical raw data for a negative signal. B) The same spectra as in A) baseline corrected. C) Typical raw data for a positive signal. D) The same spectra as in C) baseline corrected.

B5. Assay Conducted in PBS-10

For the assay conducted in PBS-10, Raman mappings were obtained from all the different tested concentrations of the S1-S2 antigen, being three random 30 by 30 μm^2 maps, with 900 measurements per map. The assay was conducted in duplicate, therefore the data consisted of a total of six maps, or 5400 measurements per concentration. Figure B-S5 shows representative digital maps for the assay conducted in PBS-10, with number of ERLs per area shown in red, based on SEM images.

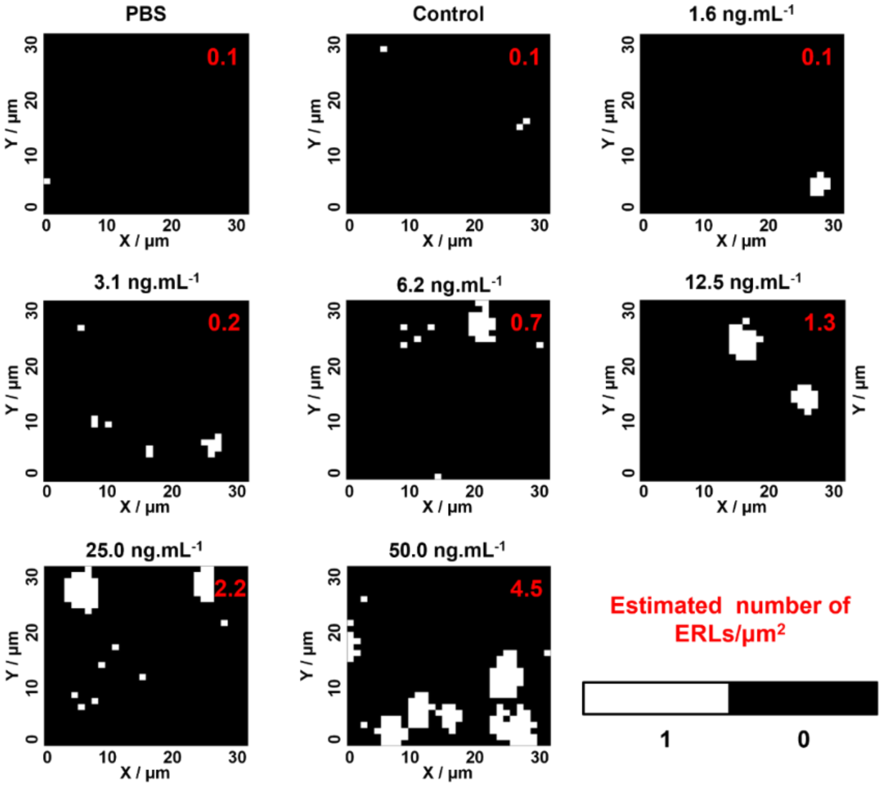

Figure B-S5. Representative digital maps for the assay conducted in PBS. The white squares represent the positive events (assigned as 1), and the black squares are the negative events (assigned as 0). The estimated number of nanoparticles per area (μm^2), based on SEM images are indicated in red.

B6. Calibration Curves for Conventional Data Analysis and Digital Protocol

Figure B-S6A shows the conventional method for data treatment, relating SERS intensities with the S1-S2 Spike Protein concentration. Figure B-S6B shows the same dataset with the digital protocol data treatment. There is a linear and a saturated region of this assay. From 25 ng.mL^{-1} of S1-S2 Spike Protein onwards, the assay saturates and can be used for detection but not quantification. The saturation of the plot may be due to saturation of available sites for the S1-S2 Spike Protein to interact with, plateauing the number of ERLs, and SERS signal at a saturation concentration. The breaks in the plot are from 650 to 5250, 5350 to 6950, 7100 to 11400, 11450 to 18440, 18500 to 19800, 19900 to 26250, 36400 to 32650, 32775 to 35000, 35050 to 42050 and 42400 to 69450, to accommodate the large variation in the SERS intensities.

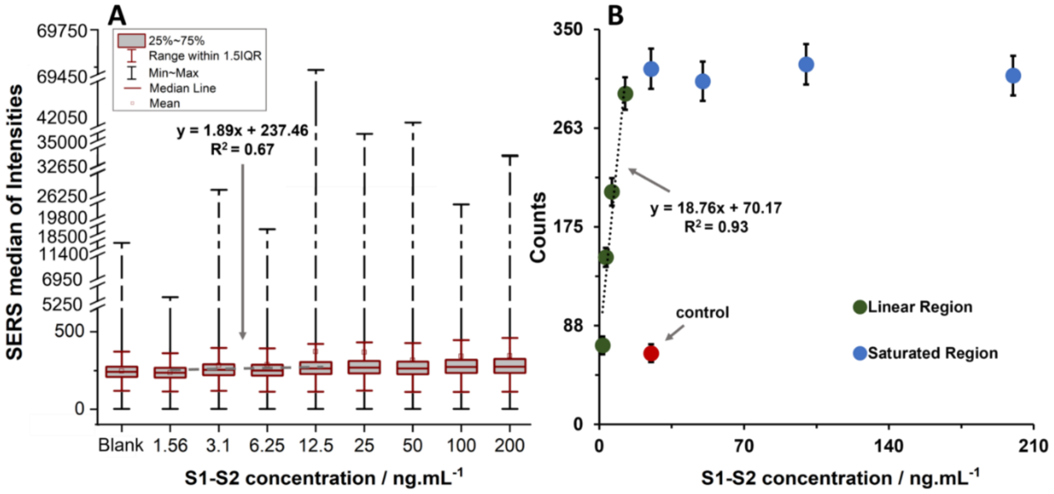

Figure B-S6. A) Calibration curve generated by the median of the intensities considering the area under the NB phenoxazine ring mode related to the concentration of the S1-S2 Spike Protein in saliva, superposed on a Box Plot with maximum and minimum shown. B) Calibration curve generated by the digital protocol, being counts (positive events) related to the concentration of the S1-S2 Spike Protein subunit in saliva.

Figure B-S7A shows the conventional method for data treatment, relating SERS intensities with the S1-S2 Spike Protein concentration. Figure B-S7B shows the same dataset with the digital protocol data treatment. The breaks in the plot are from 2800 to 5250, 5500 to 13950, 14300 to 38500, 39100 to 41400, 41700 to 43900 and 44300 to 324900, to accommodate the large variation in the SERS intensities.

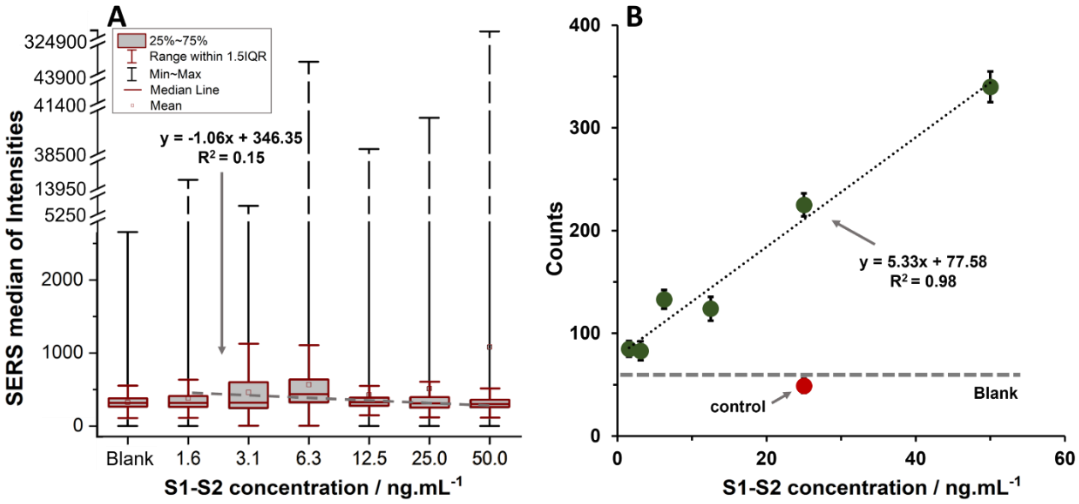

Figure B-S7. A) Calibration curve generated by the median of the intensities considering the area under the NB phenoxazine ring mode related to the concentration of the spiked S1-S2 Spike Protein in PBS-10, superposed on a Box Plot with maximum and minimum shown. B) Calibration curve generated by the digital protocol, being counts (positive events) related to the concentration of the S1-S2 Spike Protein in PBS-10.

B7. SERS Intensity Distribution Histograms

The SERS intensity distribution histograms of the NB phenoxazine ring mode areas for three S1-S2 Spike Protein concentrations are shown in Figure B-S8. The long tail distribution is expected for assays that have a small number of ERLs, caused by the presence of highly efficient hotspots.[2]

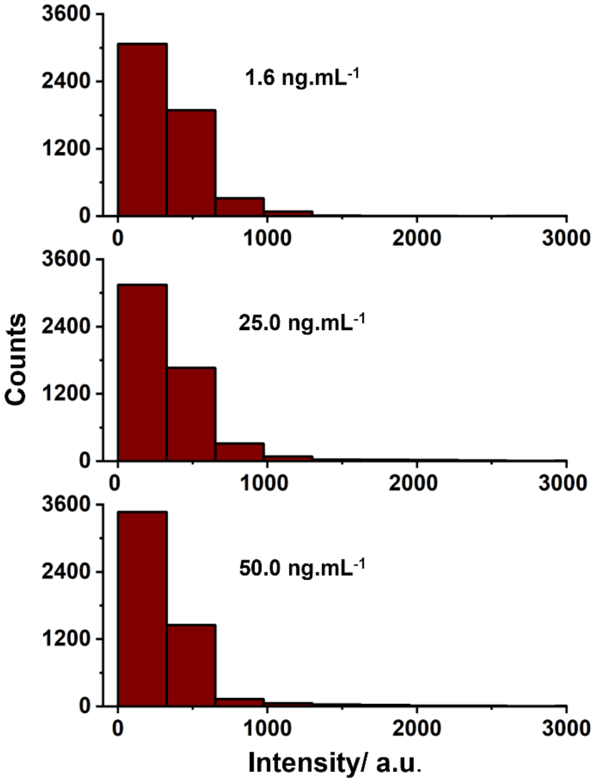

Figure B-S8. Histograms of the areas under the NB phenoxazine ring mode for three concentrations of S1-S2 Spike Protein, being 1.6, 25, and 50.0 ng.mL^{-1} in PBS-10. The populations are comprised of 5400 measurements, bin size 325, 1000 bins.

B8. Number of ERLs on the Sensor Surface and Counts Correlation

Figure B-S9 shows a linear relationship between the number of ERLs counted on the SEM images with the number of counts of the assay. The range of linearity is in accordance with the digital SERS assays. Figure B-S9A (PBS-10 assay) shows linearity in the whole assay whereas Figure B-S9B (saliva assay) has a linear and a saturated region, in accordance with the obtained digital protocol.

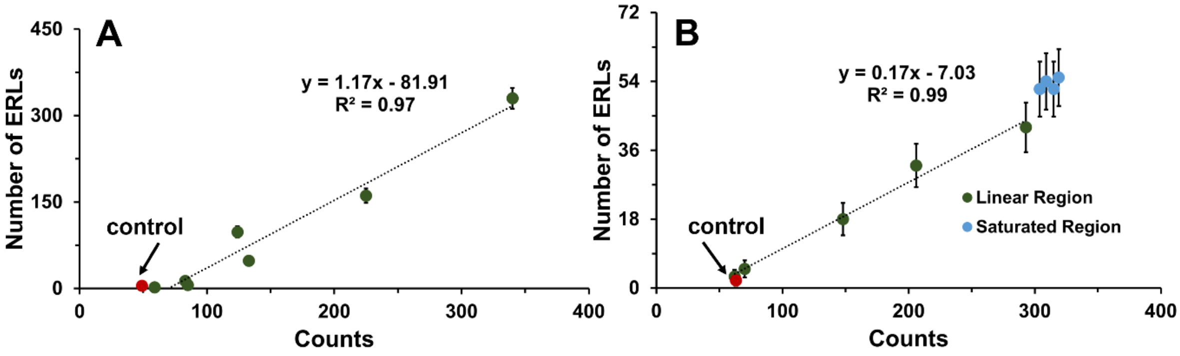

Figure B-S9. A) Linear relationship between the number of ERLs on the surface of the sensor determined by SEMs and the digital counts for the assay in PBS-10. B) Relationship between the number of ERLs on the surface of the sensor determined by SEMs and the digital counts for the assay in saliva, for the linear and saturated regions of the graph's assay.

References

(1) Tuckmantel Bido, A., Azarakhshi, A. & Brolo, A. G. Exploring Intensity Distributions and Sampling in SERS-Based Immunoassays. Anal. Chem. acs.analchem.2c02845 (2022).

(2) dos Santos, D. P., Temperini, M. L. A. & Brolo, A. G. Intensity Fluctuations in Single-Molecule Surface-Enhanced Raman Scattering. Acc. Chem. Res. 52, 456–464 (2019).

Appendix C

Appendix C is the Support Information to the unpublished work: "Detection of SARS-CoV-2 in Saliva by a Low-cost LSPR-based Sensor", by Ariadne Tuckmantel Bido Katherine J.I. Ember, Dominique Trudel, Madeleine Duran, Frederic Leblond and Alexandre G. Brolo that is ready to be submitted.

C1. Photo of the sensing films on a well plate

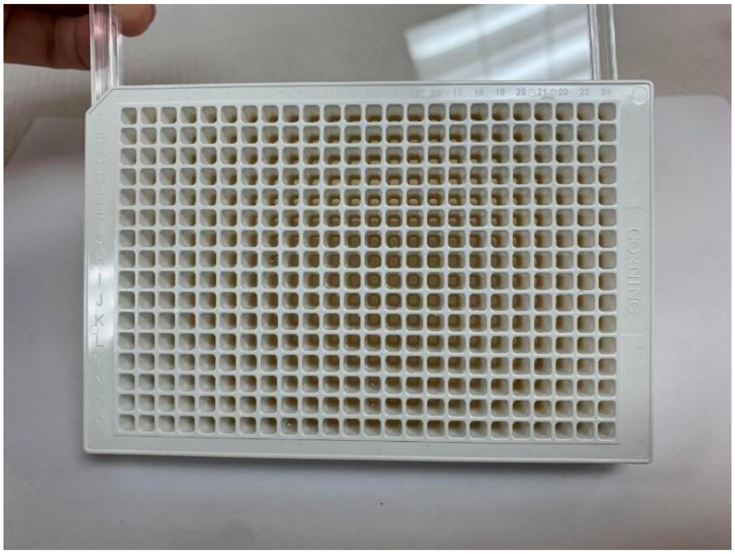

Figure C-S1. Photo of the sensing films (AgNPs) covering a well plate. Each plate has 364 individual wells for testing.

C2. Layers of the sensor

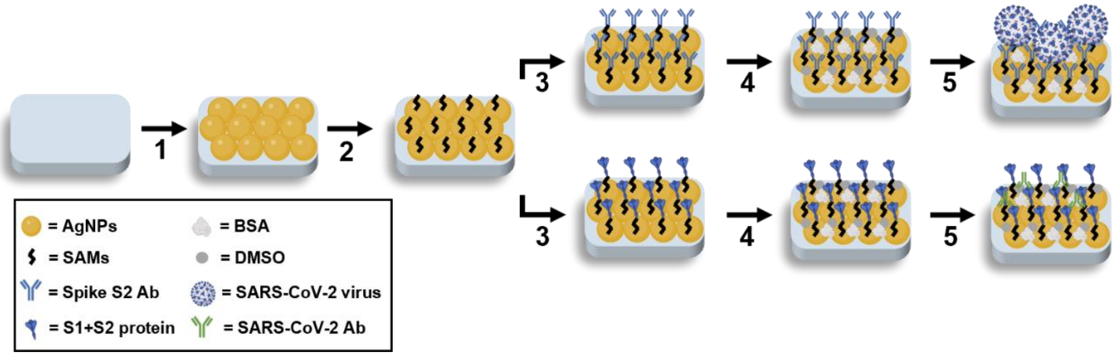

Figure C-S2. Layers constructed on the well plates. (1) AgNP film, (2) SAMS, (3) Spike S2 Ab or S1+S2 protein, (4) blocking with BSA and DMSO and (5) detection of the SARS-CoV-2 virus or SARS-CoV-2 Ab in saliva.

C3. Assay with saliva spiked with SARS-CoV-2 (2019-nCoV) Spike S1 + S2 ECD-His Recombinant Protein for protocol development.

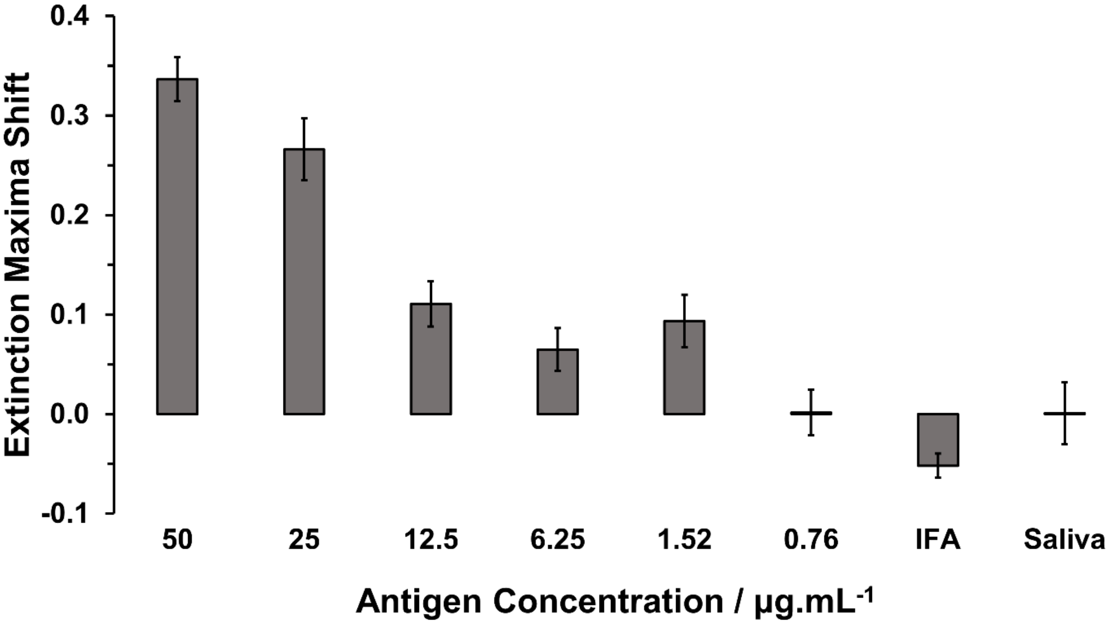

Figure C-S3. Assay conducted in saliva spiked with SARS-CoV-2 (2019-nCoV) Spike S1 + S2 ECD-His Recombinant Protein, with a control, IFA (Influenza A H7N9 (A/Shanghai/1/2013) Hemagglutinin / HA Protein (His Tag) and only saliva background. The detection element used in the AgNP film was Spike S2 Ab.

C4. Example of one well monitoring for the layering of the sensor elements and the tested saliva.

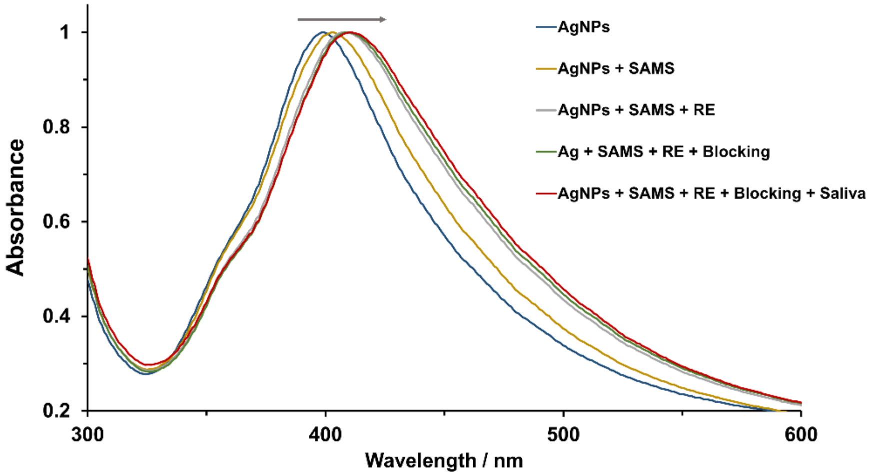

Figure C-S4. A shift of one well monitored and tested with a patient's saliva. Layers are AgNPs, SAMs, recognition element (RE) in this case SARS-CoV-2 (2019-nCoV) Spike S2 Antibody, blocking and saliva from the patient.

C5. LSPR λmax correlation with refractive index for the Ag film for RIS determination

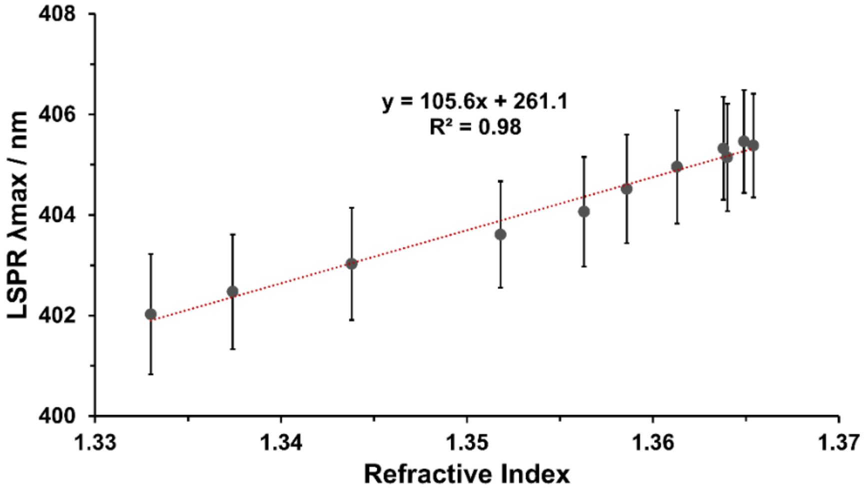

Figure C-S5. LSPR λmax correlation with refractive index for the Ag film in which the assay is based. The refractive index sensitivity (RIS) is 105.6 nm/RIU as denoted in the slope of the calibration curve.

C6. Thresholds, TPR and FRP for ROC construction for the sensor with Spike S2 Ab as detection element

To construct the ROC curves, confusion matrices were done for each possible threshold of the observed shift difference with actual and predicted "infected" and "not infected" as classifiers and determining the TRP and FRP.

Table CS-1. Thresholds, true positive rate (TPR) and false positive rate (FRP) calculated for the 15 confusion matrices used for the construction of the ROC curve for the sensor with Spike S2 Ab as detection element.

Virus Detection		
Threshold	TPR	FPR
>-0.30	1.00	1.00
>-0.20	0.89	1.00
>-0.13	0.78	1.00
>-0.03	0.56	1.00
>-0.01	0.44	1.00
>0.10	0.33	1.00
>0.13	0.11	1.00
>0.30	0.11	0.88
>0.50	0.11	0.75
>0.60	0.00	0.75
>0.69	0.00	0.63
>0.75	0.00	0.50
>0.82	0.00	0.38
>0.83	0.00	0.25
>1.05	0.00	0.13
>1.56	0.00	0.00

C7. Thresholds, TPR and FRP for ROC construction for the sensor with S1+S2 protein as detection element

Table CS-2. Thresholds, true positive rate (TPR) and false positive rate (FRP) calculated for the 19 confusion matrices used for the construction of the ROC curve for the sensor with S1+S2 protein as detection element.

Antibody Detection		
Threshold	TPR	FPR
>-0.88	1.00	1.00
>-0.85	1.00	0.89
>-0.84	1.00	0.78
>-0.67	1.00	0.67
>-0.63	1.00	0.56
>-0.55	1.00	0.44
>-0.44	1.00	0.33
>-0.37	1.00	0.22
>-0.36	1.00	0.22
>-0.34	1.00	0.22
>-0.27	1.00	0.11
>-0.01	0.75	0.11
>0.20	0.63	0.11
>0.60	0.63	0.00
>0.80	0.50	0.00
>0.90	0.25	0.00
>0.93	0.25	0.00
>1.13	0.13	0.00
>1.30	0.00	0.00